Stony Brook University

Constraining composition of Earth upper mantle and Mars from seismic, mineral physics and other geophysical data

A Dissertation Presented

by

Yi Wang

to

The Graduate School

in Partial Fulfillment of the

Requirements

for the Degree of

Doctor of Philosophy

in

Geosciences

Stony Brook University

August 2009

Stony Brook University

The Graduate School

Yi Wang

We, the dissertation committee for the above candidate for the Doctor of Philosophy degree, hereby recommend acceptance of this dissertation.

Lianxing Wen – Dissertation Advisor
Professor, Department of Geosciences

William Holt – Chairperson of Defense
Professor, Department of Geosciences

Donald J. Weidner
Distinguished Professor, Department of Geosciences

Scott McLennan
Professor, Department of Geosciences

Lupei Zhu
Associate Professor
Department of Earth and Atmospheric Sciences
Saint Louis University

This dissertation is accepted by the Graduate School

Lawrence Martin
Dean of the Graduate School

Abstract of the Dissertation

Constraining composition of Earth upper mantle and Mars from seismic, mineral physics and other geophysical data

by

Yi Wang

Doctor of Philosophy

in

Geosciences

Stony Brook University

2009

We constrain velocity structures and composition models in the Earth's upper mantle through joint modeling of seismic and mineral physics data, and the composition of Mars through joint modeling of mineral physics data and the observations of moment of inertia. For Earth, we constrain shear (SH) and compressional (P) wave velocity structures in the upper mantle beneath southern Africa, using triplicated phases recorded in the epicentral distance range of 11^o- 28^o for one shallow earthquake. Both SH and P wave data suggest presence of a low velocity zone beneath a high-velocity lithospheric lid. Seismic observations also suggest that the P/S ratio is larger (1.88) in the transition zone than in the lithospheric lid (1.70). We also constrain SH wave velocity structures near the 660-km discontinuity beneath South America and northeast Asia, using

triplicated phases near the discontinuity recorded in the epicentral distance range of 10^o-35^o for three deep earthquakes. SH velocity structures near the 660-km discontinuity are found to be different in the two regions. We then explore thermal and compositional models appropriate for explaining the inferred seismic structures in the sampling regions, based on mineral physics modeling. For Mars, we construct density models of the interior of Mars for a series of mantle compositions, core compositions and temperature profiles, and calculate the moment of inertia factors. With the constraints of total mass, possible core radius and observed moment of inertia factor, we find that Fe content in the martian mantle is between 10.5% and 14.3%; Al content in the martian mantle is less than 4%; and S content in the martian core is between 4.6% and 13.3%. We further discuss the implications of these compositional models to the understanding of formation and evolution of Mars. We also adopt the second-order internal theory of equilibrium of a self-gravitating and rotating planet to calculate the hydrostatic figure and flattening factor of Mars.

Table of Contents

List of Figures

List of Tables

Acknowledgements

The six-year stay in Stony Brook University is a precious treasure in my life. It is my pleasure to thank all the faculty, staff and students in Geosciences Department for building a wonderful research environment and making this dissertation possible.

I would like to express my deepest gratitude to my dissertation advisor: Lianxing Wen. He has been inspiring and encouraging me to pursue a career in geophysics study, providing a thoughtful guidance and been very supportive in every way during my study. I could not have wished a better advisor. In the same vein, I want to thank Donald J. Weidner, who has supervised me in mineral physics field, for his guidance and patient. Without his support, this dissertation would not be possible. I am grateful to the other members of my dissertation defense committee, William Holt, Scott McLannan and Lupei Zhu, for spending time to read and discuss the dissertation with me. I benefit tremendously from the courses taught by Lianxing Wen, William Holt, Donald J. Weidner, Teng-fong Wong and Jiuhua Chen. I also benefit from the discussions and assistances from my lab colleagues, Yumei He, Wen-Che Yu, Yi Wang, Aaron Frodsham and Hui Long, and other students in Geosciences department, especially Elliot C. Klein and Attreyee Ghosh.

I would like to thank Geosciences department staff, especially Loretta Budd, Owen Evans, Benedict Vitale for their help. I would also like to thank my friends, Wei Zhu, Wenqing Fang, Sun Zan, Bingjing Chen, Xun Xu, Shuangtao Zhang, Elliot C. Klein,

Attreyee Ghosh, Aaron Frodsham, Huaning Zhang, Xin Yang and Hui Long, for their support and friendship. They have helped me more than they realize. They make Stony Brook a second home for me.

In the end, I would like to thank my parents. Their love and unmoved faith in me is the source of my energy and confidence, and have walked me through all the difficult times.

Chapter 1 General Introduction

Understanding mantle composition and its lateral variations in Earth are important in many aspects of geophysics. For example, in large-scale modeling of the surface geodynamical observations, such as geoid, topography, and plate motions, predictions are usually made by assuming a three-dimensional instantaneous Newtonian flow, with density anomalies usually derived from seismic tomographic models by applying velocity-density scalings (e.g., *Hager, 1984; Richards and Hager, 1984; Phipps-Morgan and Shearer, 1993; Wen and Anderson, 1997a, b*). If mantle composition is known, the velocity-density scalings should represent a thermal and compositional indicator to the Earth's interior and serve as a link among geodynamics, seismology and mineral physics.

Mantle composition in Earth is also important in understanding phase transformations in Earth mantle, and phase transformations are important in understanding mantle dynamics. For example, the endothermic phase transformation from ringwoodite to perovskite plus magnesiowustite may introduce temporary layering through the 660-km discontinuity (*Honda and Balachandar, 1993; Tackley et al, 1993*). The seismically inferred transition zone thickness has often been used as a thermometer, assuming an endothermic phase transition at the 660-km discontinuity and an exothermic phase transition at the 410-km discontinuity. However, mantle composition consists of two major components: an olivine-normative component and a pyroxene-normative component. The properties of the phase transformations and the actual paths of these

phase transformations are complex and strongly depend on mantle composition and chemical interaction between the subsystems in the composition.

Different mantle compositions and temperatures result in different seismic structures in the upper mantle, and can be directly tested by seismic data. Joint modeling of seismic and mineral physics data can help us investigate mantle velocity structures and thermal and compositional models.

Compositions of other terrestrial planets are important for us to understand the formation and evolution of the planets. There are two hypotheses on the evolution of the planets. One hypothesis suggests that the different mean densities of the terrestrial planets indicate different Fe/Si ratio in the planets. Since the terrestrial planets have different distances from the Sun, the different mean densities of the planets suggest a Fe/Si fractionation in the solar nebula (*Urey, 1952; Ganapathy and Anders, 1974*). The other hypothesis suggests that the terrestrial planets all have a bulk composition with the same nonvolatile element abundances as those of C1 carbonaceous chondrite (*Ringwood, 1959*). Later, this hypothesis is revised to that the terrestrial planets consist of two chondritic components, one is completely reduced and the other is oxidized, but both components have the same bulk composition of C1 chondrite (*Wanke and Dreibus, 1988*). Based on this hypothesis, the terrestrial planets have the same Fe/Si ratio, but the ratios between metallic Fe and the total Fe are different. Understanding the composition of other terrestrial planets can help us evaluate these two hypotheses.

For other terrestrial planets, seismic data are not available, but the observation of moment of inertia is controlled by density distributions inside the planets, and can be used to constrain composition of the planets. Recent space missions to Mars provide us

precise measurements of moment of inertia of the planet. Recent progress in mineral physics field allows us to quantitatively predict velocity and density profiles in the interior of Mars, based on different mantle composition, core composition and temperature profiles insid the planet.

In this thesis, I discuss mineral physics modeling method and temperature and composition effects on mantle velocity and density in chapter 2, constrain the velocity and composition models in the upper mantle beneath southern Africa in chapter 3, constrain the detail velocity and composition structures near the 660-km discontinuity beneath South America and northeast Asia in chapter 4, and constrain the composition of Mars in chapter 5.

Chapter 2 Mineral physics modeling method and overview of effects of temperature and composition on mantle velocity and density

In this chapter, we present our mineral physics modeling method in detail. We use phase equilibria data to define the stable assemblages at relevant pressures and temperatures, and cation distribution data to define the chemical composition of each phase. This information, along with our current estimates of physical properties of these phases, provides a mineralogical model with volume fractions of each phase along with the aggregate velocities and density. We present how we define the stable assemblages in section 2.1.1; how we define the chemical composition of each mineral in section 2.1.2; how we extrapolate elastic properties to different temperatures, pressures and compositions in section 2.1.3; and how we calculate mantle velocity and density in section 2.1.4. We also discuss the effects of mantle temperature and composition, including Al, Fe and Ca contents, on discontinuity depths, velocity and density gradients and absolute velocities and density in the mantle in section 2.2.

2.1 Mineral physics modeling method

Recent progress in mineral physics field allows us to quantitatively predict velocity and density profiles in the mantle for various mantle compositions and

temperatures. In our mineral physics modeling, seismic velocity and density in the mantle are calculated following the procedures outlined in *Weidner and Wang (1998), Wang et al. (2006), Wang et al. (2008)* and *Wang et al. (2009).* We present the method in detail here. In order to calculate the velocity and density for a certain mantle temperature and composition, we need to know the stable minerals and volume fraction, chemical composition and elastic properties of each stable mineral under the condition of the mantle temperature, pressure and composition.

2.1.1 Stable minerals

We use phase equilibria data to define the stable assemblages at relevant pressures and temperatures. In this calculation, we determine the stable minerals for a certain mantle temperature, pressure and composition based on the phase diagrams of the CaO-MgO- Al_2O_3 - SiO_2 (CMAS) system reported by Gasparik (Figures 5.13 and 10.17 in *Gasparik, 2003*).

Mantle composition consists of two major components: an olivine-normative ($(Mg,Fe)_2SiO_4$) component and a pyroxene-normative ($(Mg,Fe)SiO_3$) component. At a pressure of approximate 14 GPa, olivine (α-phase) transforms to wadsleyite (β-phase), and pyroxene transforms to garnet. At a pressure of about 20 GPa, wadsleyite transforms to ringwoodite (γ-phase), and garnet transforms to Calcium-perovskite. Near the pressure of about 23 GPa, garnet transforms to perovskite and ringwoodite transforms to perovskite plus magnesiowustite. At low mantle temperature or/and high Fe content, olivine could transforms to ringwoodite first before it transforms to wadsleyite. At low mantle temperature or/and low Al content, garnet could transform to ilmenite first in the

bottom of the transition zone before it starts to transform to perovskite. Depending on mantle composition (mostly Al content), the garnet transformation to perovskite could persist to 100 km below the 660-km discontinuity. Since different phase transformations have different Clapeyron slopes, and the olivine-normative component and the pyroxene-normative pyroxene interact each other chemically, the actual phase transformation paths are complicated and controlled by mantle temperature and composition.

2.1.2 Chemical compositions and mole fractions of stable minerals

We use cation distribution data to define the chemical composition of each stable mineral. From mineral physics experiments, Fe/Mg ratios in different minerals in the upper mantle follow this relationship:

$$(\frac{Fe}{Mg})_{\alpha} : (\frac{Fe}{Mg})_{\beta} : (\frac{Fe}{Mg})_{\gamma} : (\frac{Fe}{Mg})_{OPX} : (\frac{Fe}{Mg})_{CPX} : (\frac{Fe}{Mg})_{Garnet} = 1 : 1.67 : 3.13 : 0.83 : 0.90 : 2.44$$

In the lower mantle, we assume $(\frac{Fe}{Mg})_{Pv} : (\frac{Fe}{Mg})_{Mw} = 1:1$. Since in the mantle, most of Al is in garnet and perovskite, and the Al contents of other minerals are negligible, we assume that all Al is in garnet and perovskite with other minerals Al-free. Since most of Ca is in garnet, clinoproxene and Ca-perovskite, we assume that all Ca is in garnet, clinoproxene and Ca-perovskite with other minerals Ca-free. The Al/Si ratio in garnet and Ca/Mg ratio in clinopyroxene and garnet are taken from mineral physics experiment data, and they are all controlled by mantle temperature and pressure. This information, along with the mantle composition, provides the chemical composition and mole fraction of every stable mineral for a certain temperature and pressure.

2.1.3 Elastic properties and volume fractions of stable minerals

In our database of elastic properties, every mineral is described using 45 properties (Table 1). The No. 1 to No. 11 properties are elastic properties for pure mineral (without Fe, Ca, Al) at zero pressure and a temperature of 2000 K: V_0 volume per mole oxygen; $\alpha = \alpha_0 \times (\frac{V}{V_0})^{-\delta}$ thermal expansion; γ Gruneisen parameter; q volume dependence of Gruneisen parameter; K bulk modulus; dK/dP pressure dependence of bulk modulus; dK/dT temperature dependence of bulk modulus; μ shear modulus; $d\mu/dP$ pressure dependence of shear modulus; $d\mu/dT$ temperature dependence of shear modulus. The No. 12 to No. 44 properties are the composition corrections: the No. 12 to No. 22 properties are $\frac{d}{dX_{Fe}}$ of the No. 1 to No. 11 properties; the No. 23 to No. 33 properties are $\frac{d}{dX_{Al}}$ of the No. 1 to No. 11 properties; the No. 34 to No. 44 properties are $\frac{d}{dX_{Ca}}$ of the No. 1 to No. 11 properties. The No. 45 property is the anisotropy of a single crystal (Table 1). These elastic properties come from either first principle calculations or experiments. For a mineral with a certain chemical composition, we make composition corrections for the first 11 elastic properties, using No. 12 to No. 44 properties. Then we extrapolate bulk modulus, shear modulus and volume at the room pressure and a temperature of 2000 K to the certain temperature and pressure using the third order Birch-Murnaghan equation of state (*Birth, 1947*). Based on the volume and the mole fraction of every stable mineral, we calculate the volume fraction and density of each stable mineral.

2.1.4 Calculate velocity and density in the mantle

With the bulk modulus K, shear modulus μ, density ρ and volume fractions Fv of every stable mineral, we calculate the combined bulk modulus, shear modulus and density of the assemblage using these equations:

$$K_{total} = \frac{1}{2}\sum_{i=1}^{n}(K_i Fv_i) + \frac{1}{2}\frac{1}{\sum_{i=1}^{n}\frac{1}{K_i}Fv_i} \quad (1)$$

$$\mu_{total} = \frac{1}{2}\sum_{i=1}^{n}(\mu_i Fv_i) + \frac{1}{2}\frac{1}{\sum_{i=1}^{n}\frac{1}{\mu_i}Fv_i} \quad (2)$$

$$\rho_{total} = \sum_{i=1}^{n}\rho_i Fv_i \quad (3)$$

Then we calculate the P and S velocity using equations:

$$Vp = \sqrt{\frac{K_{total} + 4\mu_{total}}{\rho_{total}}}, \qquad Vs = \sqrt{\frac{\mu_{total}}{\rho_{total}}} \quad (4)$$

Table 1. Elastic properties for mantle minerals at zero pressure and a temperature of 2000 K

	Minerals	Oliv	OPX	CPX	Garnet	Wads	Ring
1	$V_0\ (cm^3)$	11.54	11.41	10.17	9.96	10.70	10.54
2	$\alpha_0(\times 10^{-5})\ (1/K)$	3.89	2.72	2.72	2.93	3.58	3.85
3	δ	4.05	3.265	3.265	3.76	4.016	5.2
4	γ	1.19	0.97	0.97	1.15	1.289	1.34
5	q	1.33	0.114	0.114	0.8	1.013	1.44
6	K (GPa)	109.45	100	105	154.23	144.45	138
7	dK/dP	4.15	4.45	4.45	4.3	4.164	5.2
8	$dK/dT\ (\times 10^{-3})$ (GPa/K)	-2	0.9	0.9	3.3	-1.53	0
9	μ (GPa)	58.1	73.62	73.62	77.11	75.21	90.46
10	$d\mu/dP$	1.331	1.46	1.46	1.328	1.671	1.497
11	$d\mu/dT\ (\times 10^{-3})$ (GPa/K)	-7	-5.6	-5.6	-2.8	-10.2	-8.6
12	$dV_0/dX_{Fe}\ (cm^3)$	0.782	0.488	0.488	0.0188	0.820	0.744
13	$d\alpha_0/dX_{Fe}\ (1/K)$	0	0	0	0	0	0
14	$d\delta/dX_{Fe}$	0	0	0	0	0	0
15	$d\gamma/dX_{Fe}$	0	0	0	0	0	0
16	$d\mathrm{q}/dX_{Fe}$	0	0	0	0	0	0
17	dK/dX_{Fe}(GPa)	5.86	-6.91	-6.91	7.87	19.34	35.38
18	$d(dK/dP)/dX_{Fe}$	0	0	0	0	0	0
19	$d(dK/dT)/dX_{Fe}$ (GPa/K)	0	0	0	0	0	0
20	$d\mu/dX_{Fe}$(GPa)	-30.61	-24.74	-24.74	4.54	-47.64	-30.56
21	$d(d\mu/dP)/dX_{Fe}$	0	0	0	0	0	0
22	$d(d\mu/dT)/dX_{Fe}$ (GPa/K)	0	0	0	0	0	0

Oliv denotes olivine; Wads wadsleyite; Ring ringwoodite; OPX orthopyroxene; CPX clinopyroxene.

Table 1. Elastic properties for mantle minerals at zero pressure and a temperature of 2000 K (continue)

	Minerals	Stis	Mw	Il	Pv	Ca-Pv
1	$V_0\ (cm^3)$	8.58	11.92	9.20	8.576	9.766
2	$\alpha_0(\times 10^{-5})(1/K)$	3.24	4.5	3.21	3.24	3.78
3	δ	3.45	5	4.59	3.45	4.1
4	γ	1.56	1.4	1.36	1.56	1.63
5	q	1.02	0.9	1.84	1.02	1
6	K (GPa)	210.08	127.72	185.1	210.08	170.9
7	dK/dP	4.299	4.244	4.3	4.3	4.76
8	$dK/dT\ (\times 10^{-3})$ (GPa/K)	-0.196	0	0	-0.196	0
9	μ (GPa)	151.02	112.03	85.7	151.02	104.7
10	$d\mu/dP$	1.56	2.08	2.097	1.56	1.9
11	$d\mu/dT\ (\times 10^{-3})$ (GPa/K)	-13.76	0	-10	-13.7	0
12	$dV_0/dX_{Fe}\ (cm^3)$	0.341	1.160	0.5	0.341	0
13	$d\alpha_0/dX_{Fe}\ (1/K)$	0	0	0	0	0
14	$d\delta/dX_{Fe}$	0	0	0	0	0
15	$d\gamma/dX_{Fe}$	0	0	0	0	0
16	$d\mathrm{q}/dX_{Fe}$	0	0	0	0	0
17	dK/dX_{Fe}(GPa)	35.39	-8.17	5	35.39	0
18	$d(dK/dP)/dX_{Fe}$	0	0	0	0	0
19	$d(dK/dT)/dX_{Fe}$ (GPa/K)	0	0	0	0	0
20	$d\mu/dX_{Fe}$(GPa)	-54.71	-87.16	-20	-54.71	0
21	$d(d\mu/dP)/dX_{Fe}$	0	0	0	0	0
22	$d(d\mu/dT)/dX_{Fe}$ (GPa/K)	0	0	0	0	0

Stis denotes stishovite; Mw magnesiowustite; Il ilmenite; Pv provskite; Ca-Pv Calcium-provskite

Table 1. Elastic properties for mantle minerals at zero pressure and a temperature of 2000 K (continue)

	Minerals	Oliv	OPX	CPX	Garnet	Wads	Ring
23	$dV_0 / dX_{Al}\ (cm^3)$	0	0	0	-0.3 88	0	0
24	$d\alpha_0 / dX_{Al}\ (1/K)$	0	0	0	0	0	0
25	$d\delta / dX_{Al}$	0	0	0	0	0	0
26	$d\gamma / dX_{Al}$	0	0	0	0	0	0
27	dq / dX_{Al}	0	0	0	0	0	0
28	dK / dX_{Al} (GPa)	0	0	0	21.08	0	0
29	$d(dK / dP) / dX_{Al}$	0	0	0	0	0	0
30	$d(dK / dT) / dX_{Al}$ (GPa / K)	0	0	0	0	0	0
31	$d\mu / dX_{Al}$ (GPa)	0	0	0	7.76	0	0
32	$d(d\mu / dP) / dX_{Al}$	0	0	0	0	0	0
33	$d(d\mu / dT) / dX_{Al}$ (GPa / K)	0	0	0	0	0	0
34	$dV_0 / dX_{Ca}\ (cm^3)$	0	0	0	1.062	0	0
35	$d\alpha_0 / dX_{Ca}\ (1/K)$	0	0	0	0	0	0
36	$d\delta / dX_{Ca}$	0	0	0	0	0	0
37	$d\gamma / dX_{Ca}$	0	0	0	0	0	0
38	dq / dX_{Ca}	0	0	0	0	0	0
39	dK / dX_{Ca} (GPa)	0	0	0	-4.4	0	0
40	$d(dK / dP) / dX_{Ca}$	0	0	0	0	0	0
41	$d(dK / dT) / dX_{Ca}$ (GPa / K)	0	0	0	0	0	0
42	$d\mu / dX_{Ca}$ (GPa)	0	0	0	16.9	0	0
43	$d(d\mu / dP) / dX_{Ca}$	0	0	0	0	0	0
44	$d(d\mu / dT) / dX_{Ca}$ (GPa / K)	0	0	0	0	0	0
45	Anisotropy	0.24	0.25	0.25	0.02	0.28	0.04

Oliv denotes olivine; Wads wadsleyite; Ring ringwoodite; OPX orthopyroxene; CPX clinopyroxene.

Table 1. Elastic properties for mantle minerals at zero pressure and a temperature of 2000 K (continue)

	Minerals	Stis	Mw	Il	Pv	Ca-Pv
23	$dV_0 / dX_{Al}\ (cm^3)$	0.097	0	0	0.097	0
24	$d\alpha_0 / dX_{Al}\ (1/K)$	0	0	0	0	0
25	$d\delta / dX_{Al}$	0	0	0	0	0
26	$d\gamma / dX_{Al}$	0	0	0	0	0
27	dq / dX_{Al}	0	0	0	0	0
28	dK / dX_{Al} (GPa)	-9.39	0	0	-9.39	0
29	$d(dK / dP) / dX_{Al}$	0	0	0	0	0
30	$d(dK / dT) / dX_{Al}$ (GPa / K)	0	0	0	0	0
31	$d\mu / dX_{Al}$ (GPa)	-40.39	0	0	-40.39	0
32	$d(d\mu / dP) / dX_{Al}$	0	0	0	0	0
33	$d(d\mu / dT) / dX_{Al}$ (GPa / K)	0	0	0	0	0
34	$dV_0 / dX_{Ca}\ (cm^3)$	0	0	0	0	0
35	$d\alpha_0 / dX_{Ca}\ (1/K)$	0	0	0	0	0
36	$d\delta / dX_{Ca}$	0	0	0	0	0
37	$d\gamma / dX_{Ca}$	0	0	0	0	0
38	dq / dX_{Ca}	0	0	0	0	0
39	dK / dX_{Ca} (GPa)	0	0	0	0	0
40	$d(dK / dP) / dX_{Ca}$	0	0	0	0	0
41	$d(dK / dT) / dX_{Ca}$ (GPa / K)	0	0	0	0	0
42	$d\mu / dX_{Ca}$ (GPa)	0	0	0	0	0
43	$d(d\mu / dP) / dX_{Ca}$	0	0	0	0	0
44	$d(d\mu / dT) / dX_{Ca}$ (GPa / K)	0	0	0	0	0
45	Anisotropy	0.3	0.2	0.26	0.15	0.3

Stis denotes stishovite; Mw magnesiowustite; Il ilmenite; Pv provskite; Ca-Pv Calcium-provskite

2.2 Temperature and composition effects on mantle velocity and density

Mantle velocity and density structures are controlled by the phase transformations in the mantle. For the Earth's mantle, the 410-km discontinuity is caused by the phase transformation from olivine to wadsleyite; the 520-km discontinuity is caused by the phase transformations from wadsleyite to ringwoodite and from garnet to Ca-perovskite; the 660-km discontinuity is caused by phase transformations from garnet to perovskite and from ringwoodite to perovskite plus magnesiowustite (Figure 1). The velocity and density gradients above the 410-km discontinuity is controlled by the gradual phase transformation from pyroxene to garnet; the velocity and density gradients in the bottom of transition zone is controlled by the presence or absence of ilmenite phase and the phase transformation from garnet to ilmenite; the velocity grandient in the top of the lower mantle is controlled by the gradual phase transformations from garnet to perovskite below the 660-km discontinuity (Figure 1). The actual phase transformation paths are complicated, because the phase changes of the olivine- and pyroxene-nominative systems interact chemically.

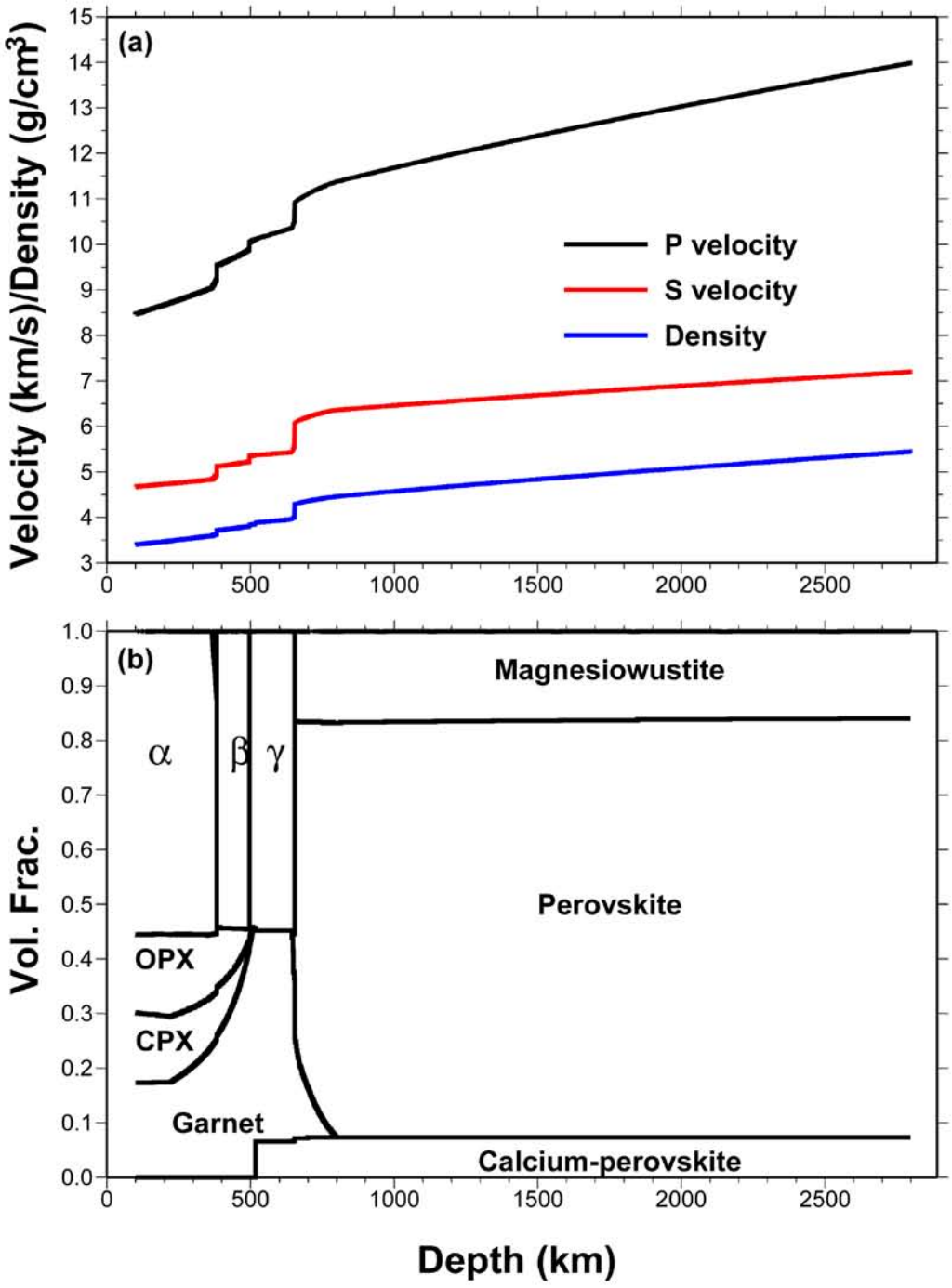

Figure 1. (a) Mineralogical structure and (b) associated P and S velocities and density structures in Earth's mantle calculated base on pyrolite composition model and a reference temperature model. α denotes olivine; β wadsleyite; γ ringwoodite; OPX orthopyroxne; and CPX clinopyroxene.

2.2.1 Temperature effects

Mantle temperature has significant effects on phase transformations and velocity and density structures in the mantle. Mantle temperatures affect the depths of the phase transformations. The depths of exothermic phase transformations (olivine →wadsleyite, wadsleyite → ringwoodite, garnet → Ca-perovskite, garnet → perovskite) increase when mantle temperature increases, and decrease when mantle temperature decrease; while the depths of endothermic phase transformations (e.g. ringwoodite →perovskite + magnesiowustite) do the opposite. For a certain mantle composition, a lower mantle temperature results in a shallower 410-km discontinuity, a shallower 520-km discontinuity and a deeper 660-km discontinuity (Figure 2a); a higher mantle temperature results in a deeper 410-km discontinuity, a deeper 520-km discontinuity and a shallower 660-km discontinuity (Figure 2c). Different mantle temperatures would cause different phase transformations in the mantle. A low mantle temperature causes two other phase transformations: olivine transforms to ringwoodite before it transforms to wadsleyite; garnet transforms to ilmenite before it transforms to perovskite (Figure 2a), and results in high density and velocity gradients just above the 410-km discontinuity and in the bottom of transition zone (Figure 2a). A high mantle temperature causes a phase transformation from ringwoodite to garnet and magnesiowustite at the bottom of the transition zone and a more gradual phase transformation from garnet to perovskite (Figure 2c) across the 660-km discontinuity, and results in a more gradual 660-km discontinuity. Mantle temperature also affects the elastic properties of mantle minerals, so it affects mantle velocity and density. The P velocity, S velocity and density in the mantle increase when

mantle temperature decreases (Figure 2a); and decrease when mantle temperature increases (Figure 2c).

2.2.2 Composition effects

2.2.2.1 Al content effects

Al content in the mantle affects the stability of garnet phase, so it affects the phase transformations and velocity and density structures in the mantle. A lower Al content reduces the stability of garnet. It causes less garnet and more pyroxene in shallow part of the upper mantle and a smaller depth extent of garnet phase below the 660-km discontinuity (Figure 3a). Since garnet has higher density and bulk modulus than those of pyroxene, but with very similar shear modulus as that of pyroxene, a lower Al content results in a lower density, a lower P velocity and a similar S velocity in the shallow part of the upper mantle (Figure 3a). The gradual phase transformation from garnet to perovskite below the 660-km discontinuity causes large density and velocity gradients in top of the lower mantle. A lower Al content results in a smaller depth extent of the large density and velocity gradients in the top of the lower mantle (Figure 3a). A low Al content also causes a phase transformation from garnet to ilmenite before garnet transforms to perovskite, and results in large density and velocity gradients in the bottom of the transition zone (Figure 3a). A higher Al content increases the stability of garnet, and causes more garnet and less pyroxene in shallow part of the upper mantle and a larger depth extent of garnet phase below the 660-km discontinuity. It results in a higher density, a higher P velocity and a similar S velocity in the shallow part of the upper mantle and a larger depth extent of the large density and velocity gradients in the top of the lower mantle (Figure 3c).

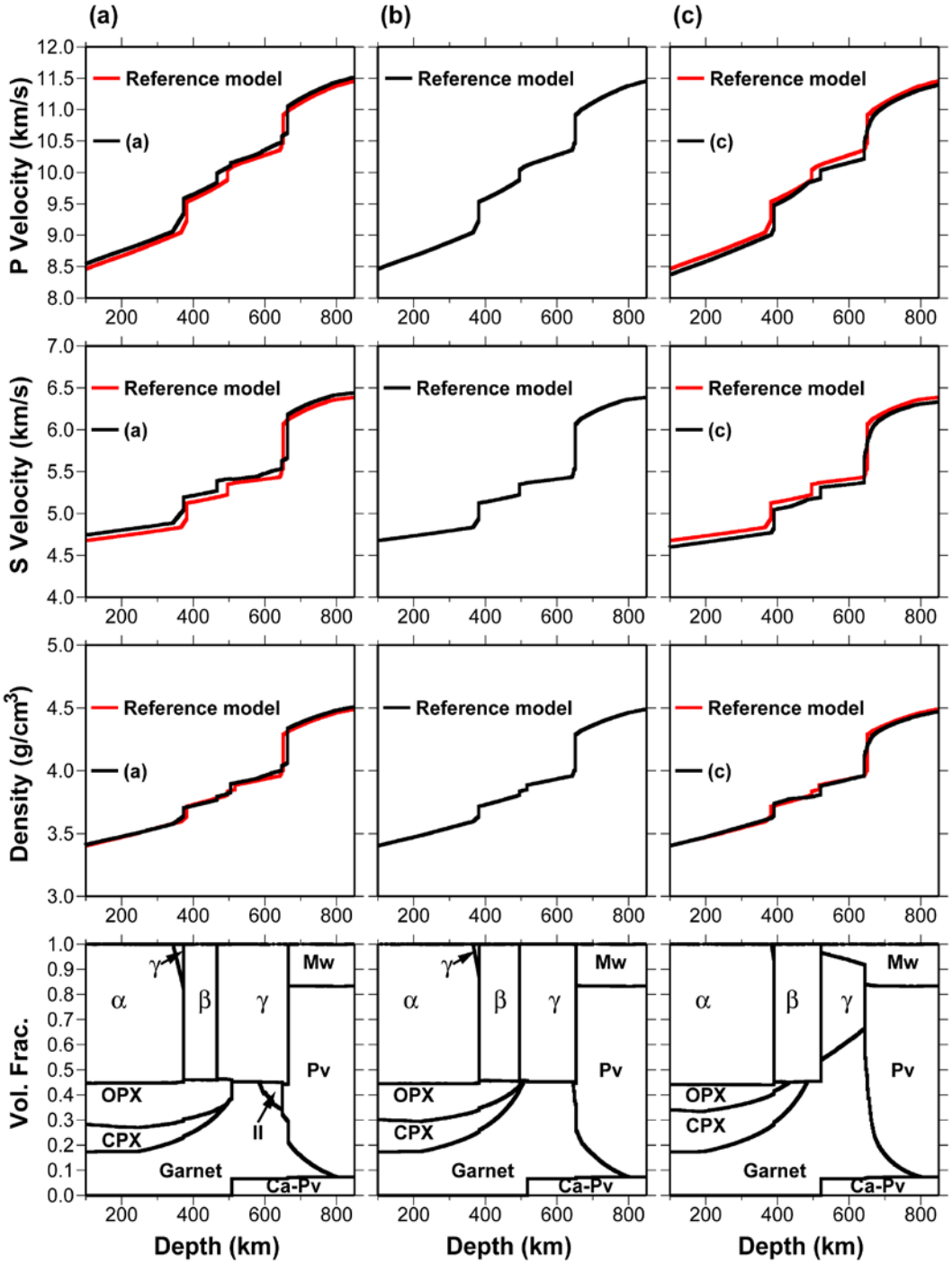

Figure 2. The mineralogical structures, P and S velocity and density structures in Earth mantle predicted based on pyrolite composition model and three different temperature models: (a) 200 $^{\circ}C$ lower than the reference temperature model; (b) the reference temperature model; (c) 200 $^{\circ}C$ higher than the reference temperature model. α denotes olivine; β wadsleyite; γ ringwoodite; OPX orthopyroxne; CPX clinopyroxene; Il ilmenite; Pv perovskite; Ca-Pv Cacium-perovskite; and Mw magnesiowustite.

2.2.2.2 Fe content effects

Fe content affects the elastic properties of every mineral in the mantle, so it affects the density and velocity in the mantle. A lower Fe content causes a lower density and higher P and S velocities (Figure 4a); and a higher Fe content does the opposite (Figure 4c). A high Fe content causes a phase transformation from olivine to ringwoodite before olivine transforms to wadsleyite, and when Fe content increases, more olivine transforms to ringwoodite before it transforms to wadsleyite (Figures 4b and 4c). This phase transformation results in large density and velocity gradients just above the 410-km discontinuity (Figures 4b and 4c).

2.2.2.3 Ca content effects

Ca content in mantle affects the volume ratio between orthopyroxene and clinopyroxene, and the volume fraction of Ca-perovskite. A decreasing Ca content increases the volume fraction of orthopyroxene and decreases the volume fractions of clinopyroxene and Ca-perovskite (Figure 5a). Since clinopyroxene has a higher density and lower P and S velocities than those of orthopyroxene, and Ca-perovskite has lower P and S velocities than those of perovskite, a lower Al content results in a lower density and higher P and S velocities in the shallow part of the upper mantle and higher P and S velocities in the lower mantle (Figure 5a). An increasing Ca content decreases the volume fraction of orthopyroxene and increases the volume fractions of clinopyroxene and Ca-perovskite (Figure 5c), and results in a higher density and lower P and S velocities in the shallow part of the upper mantle and lower P and S velocities in the lower mantle (Figure 5c).

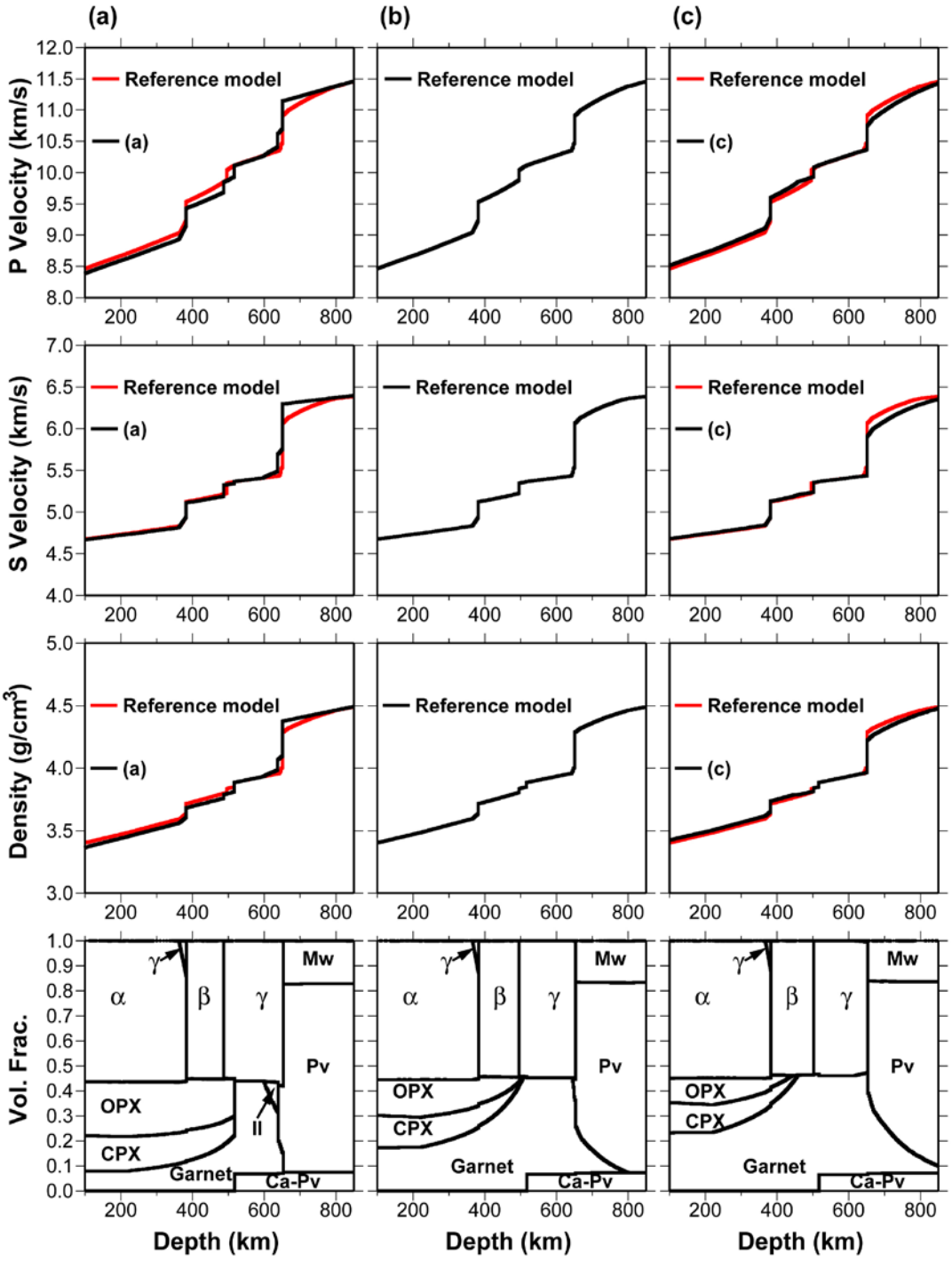

Figure 3. The mineralogical structures, P and S velocity and density structures in Earth mantle predicted based on a reference temperature model and three composition models with different Al contents: (a) Al content = 2%; (b) Al content = 4.42% (pyrolite composition); (c) Al content = 6%. α denotes olivine; β wadsleyite; γ ringwoodite; OPX orthopyroxne; CPX clinopyroxene; Il ilmenite; Pv perovskite; Ca-Pv Cacium-perovskite; and Mw magnesiowustite.

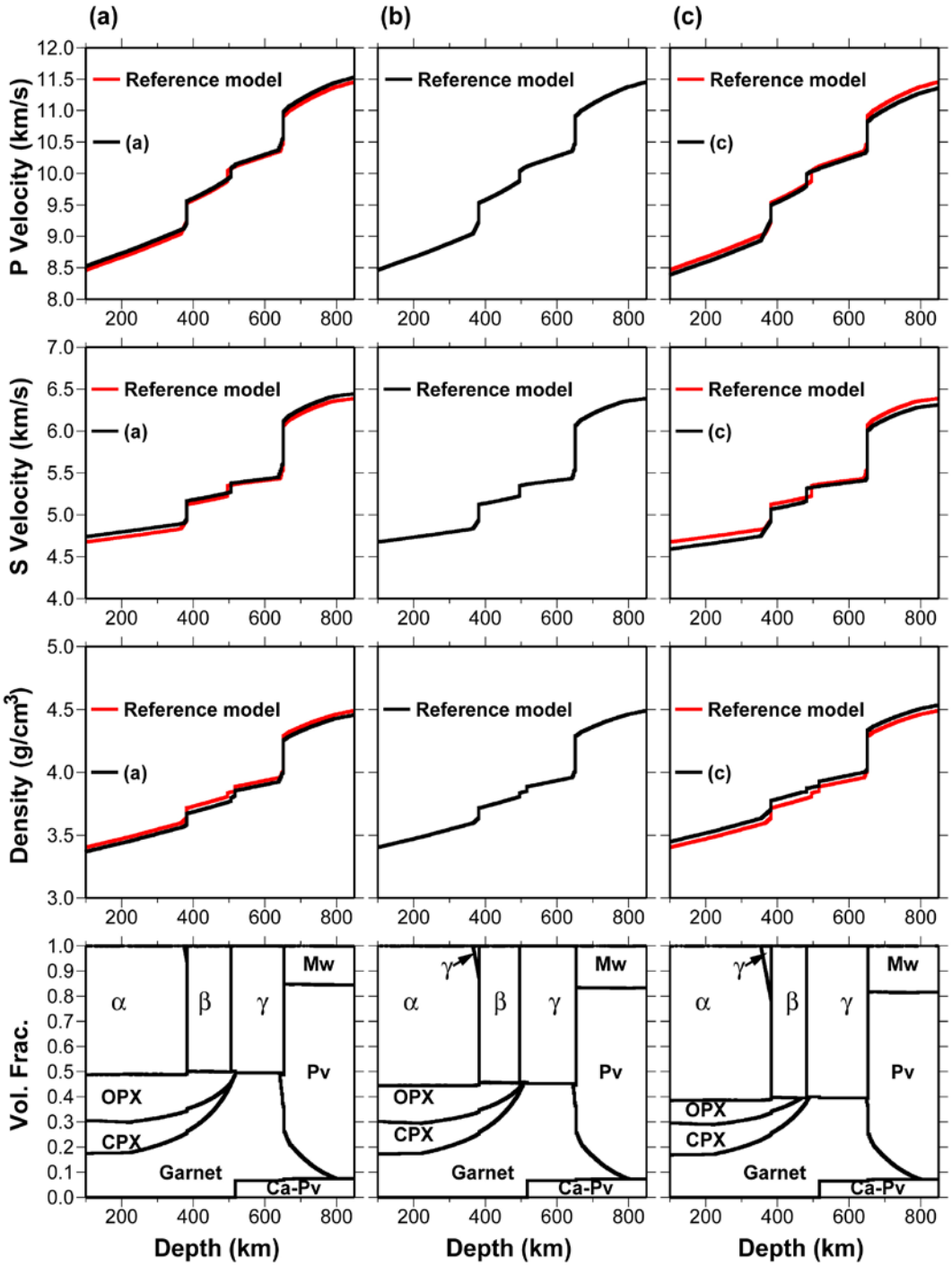

Figure 4. The mineralogical structures, P and S velocity and density structures in Earth mantle predicted based on a reference temperature model and three composition models with different Fe contents: (a) Fe content = 4%; (b) Fe content = 5.68% (pyrolite composition); (c) Fe content = 8%. α denotes olivine; β wadsleyite; γ ringwoodite; OPX orthopyroxne; CPX clinopyroxene; Pv perovskite; Ca-Pv Cacium-perovskite; and Mw magnesiowustite.

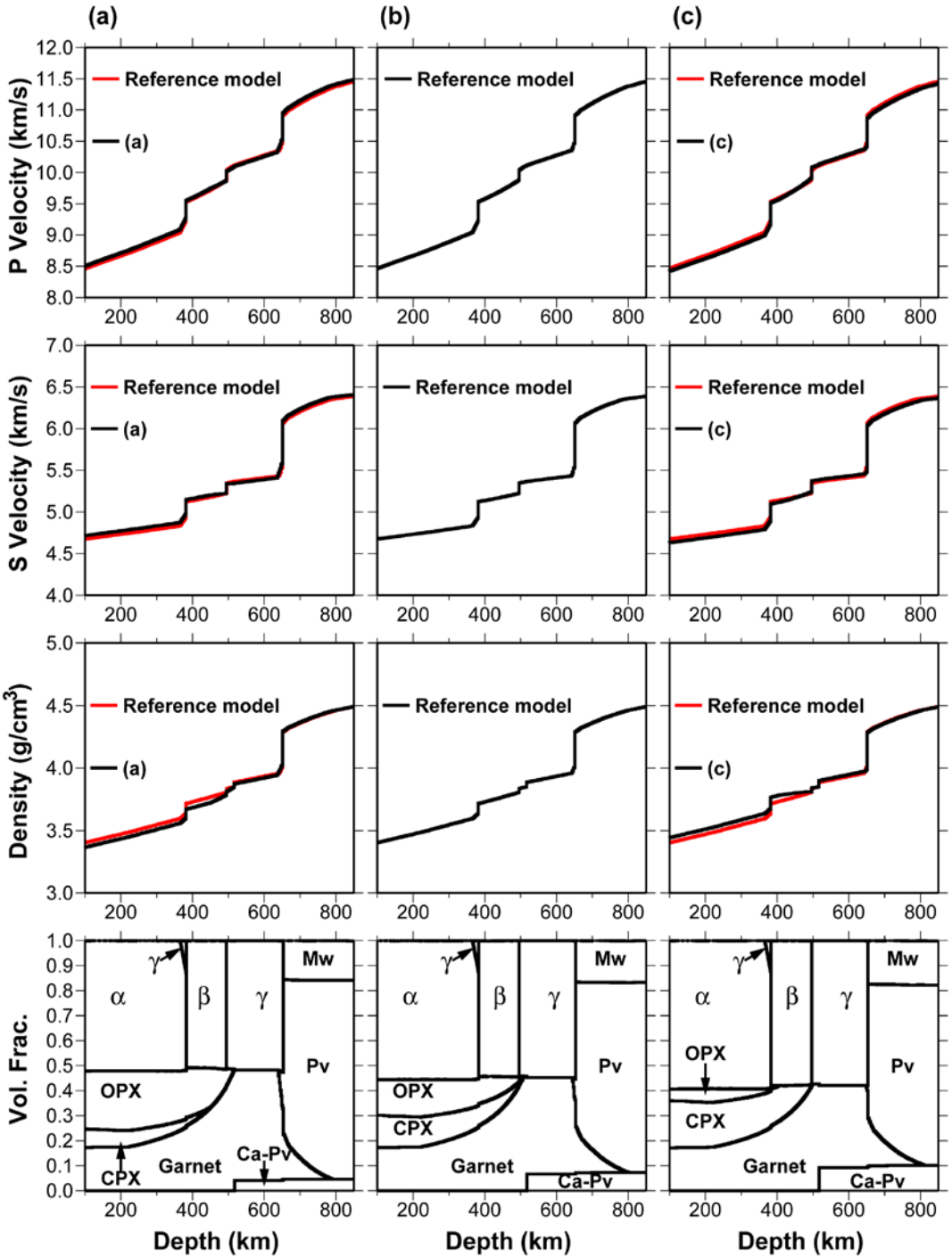

Figure 5. The mineralogical structures, P and S velocity and density structures in Earth mantle predicted based on a reference temperature model and three composition models with different Ca contents: (a) Ca content = 2%; (b) Ca content = 3.21% (pyrolite composition); (c) Ca content = 4.5%. α denotes olivine; β wadsleyite; γ ringwoodite; OPX orthopyroxne; CPX clinopyroxene; Pv perovskite; Ca-Pv Cacium-perovskite; and Mw magnesiowustite.

Chapter 3 Upper mantle velocity and composition models beneath southern Africa

3.1 Abstract

We constrain SH and P wave velocity structures in the upper mantle beneath southern Africa, using triplicated phases recorded in the epicentral distance range of 11^o-28^o for one shallow event. We then explore thermal and compositional models appropriate for explaining the inferred seismic structures in the region. Both SH and P wave data suggest presence of a low velocity zone with velocity reductions of at least –5% for S waves and –2% for P waves beneath a 150 km thick high-velocity lithospheric lid. Seismic observations also suggest that the P/S ratio is larger (1.88) in the transition zone than in the lithospheric lid (1.70). The inferred P wave velocity jump across the 660-km discontinuity is small (<4%), while the inferred SH wave velocity jump across the discontinuity is comparable to that in the Preliminary Reference Earth Model. The low velocity zone can be explained by a high temperature gradient of $6^oC/km$ or presence of partial melt. Partial melt would require presence of water or other volatile elements in the depth range of the low velocity zone to lower the mantle solidus. The different P/S velocity ratios between the lithospheric lid and the transition zone can be explained by a difference in aluminum content of mantle composition, with values of 1% in the lithospheric lid and 4% in the transition zone, respectively. The inferred P and SH

velocity jumps suggest a bulk sound velocity decrease of 3.4% across the 660-km discontinuity. Such a large decrease of bulk sound velocity is possible only if the bulk modulus of perovskite is similar to those of ringwoodite and garnet, a result remained to be confirmed by experimental or theoretical studies. The presence of the low velocity zone with large velocity reductions beneath southern Africa suggests existence of a low-density anomaly beneath the lithospheric lid, which may provide an explanation to the observed localized uplift in the "African Superswell".

3.2 Introduction

Southern Africa is a particularly interesting region for studying mantle composition and dynamics. The upper mantle structure beneath southern Africa provides an opportunity to study the depth extent and composition of the cratonic root. The southern African plateau is elevated by more than 1 km above the sea level and the surrounding oceans have a residual bathymetry in excess of 500 m (*Nyblade and Robinson, 1994*). These elevated regions are termed the "African Superswell" by *Nyblade and Robinson* (1994). The geoid also exhibits a positive anomaly, but the geoid anomaly is manifested in a broader region in Africa. The sources for the anomalously high elevation in the "African Superswell" and the relatively larger scale gravity anomaly in the region are still under debate. While *Nyblade and Robinson* (1994) suggested that the "African Superswell" may be caused by a thermal anomaly in the lithosphere, *Lithgow-Bertelloni and Silver* (1998) argued that the superswell can be explained by some density anomaly in the lower mantle. The detailed upper mantle velocity structures beneath

southern Africa are needed to evaluate these possible proposals for the origin of the "African Superswell".

Different mantle compositions and temperatures result in different seismic structures in the upper mantle, and can be directly tested by seismic data. Joint modeling of seismic and mineral physics data can help us investigate mantle velocity structures and thermal and compositional models.

In this study, we use joint modeling of seismic and mineral physics data to constrain the seismic P and SH velocity structures and thermal and compositional models in the upper mantle beneath southern Africa. We adopt waveform modeling to constrain the seismic structure. Synthetic waveforms are calculated by a reflectivity program (*Zhu and Rivera, 2002*). We also explore mantle mineralogical models that are associated with the inferred mantle thermal and compositional models. We discuss seismic data in Section 3.3, shear and compressional wave velocity structures beneath southern Africa in Sections 3.4 and 3.5, thermal, compositional and mineralogical models in Section 3.6, effects of lateral heterogeneity and attenuation, and comparisons with seismic results from previous studies on southern Africa and the Canadian Shield in Section 3.7, and implications for the origin of the "African Superswell" in Section 3.8.

3.3 Seismic Data

The sampling region of the seismic data is the upper mantle beneath southern Africa (Figure 6). The P and SH velocity structures of the upper mantle in this region are constrained using the triplicated phases recorded by the Kaapvaal Seismic Array in the epicentral distance range of $11^0 - 28^0$ for a shallow event occurring in southern Africa.

The seismic data of the event have a high signal to noise ratio and are selected from the earthquakes occurring in Africa during the lifetime of the Kaapvaal Array. The source mechanism of this event is 315^o for strike, 36^o for dip and -133^o for slip. The dense coverage of the Kaapvaal Array provides good sampling coverage for the entire depth range in the upper mantle. Our seismic approach is similar to those seismic studies using triplicated phases in the upper mantle distance ranges (*e.g., Helmberger and Wiggins, 1971; Burdick and Helmberger, 1978; Given and Helmberger, 1980; Walck, 1984; Grand and Helmberger, 1984a, 1984b; LeFevre and Helmberger, 1989; Cummins et al, 1992; Neele, 1996; Brudzinski and Chen, 1997; Melbourne and Helmberger, 1998; Zhao et al., 1999; Brudzinski and Chen, 2000; Brudzinski and Chen, 2003, Chen and Brudzinski, 2003; Song et al., 2004*).

Several seismic phases can be used to constrain the velocity structures in the upper mantle: the direct phase traveling in the lithospheric lid (AB branch), the reflection off the 410-km discontinuity (BC branch), the wave traveling in the transition zone (CD branch), the reflection off the 660-km discontinuity (DE branch), the wave traveling below the 660-km discontinuity (EF branch) and the wave traveling in the low velocity zone (CG branch) (Figure 7). The absolute travel time of the AB branch is sensitive to the seismic velocity in the lithospheric lid. The amplitude change of the AB phase with distance is sensitive to presence or absence of a low velocity zone below the lithospheric lid and the onset depth of the low velocity zone. The presence of a low velocity zone would create a shadow zone for the AB branch and generate weak direct arrivals. The onset distance of the observed weakened direct arrivals is controlled by the onset depth of the low velocity zone. The travel time differences between the AB and BC branches and

between the AB and CD branches are sensitive to the velocity reduction in the low velocity zone and the depth of the 410-km discontinuity. The travel time difference between the CD and DE branches is sensitive to the depth of the 660-km discontinuity and the velocity structure above the 660-km discontinuity. The travel time difference between the CD and EF branches is sensitive to the seismic velocity in the transition zone, the velocity jump across the 660-km discontinuity and the depth of the 660-km discontinuity. In the SH data, three phases, AB, CD and EF, can be recognized; while in the P data, only the AB and CD branches can be recognized. The triplications in the upper mantle occur in an epicentral distance range of 11^{o} - 28^{o}, so the data in this epicentral distance range is used. Seismic data are bandpass filtered in a frequency range of 0.05-1 Hz.

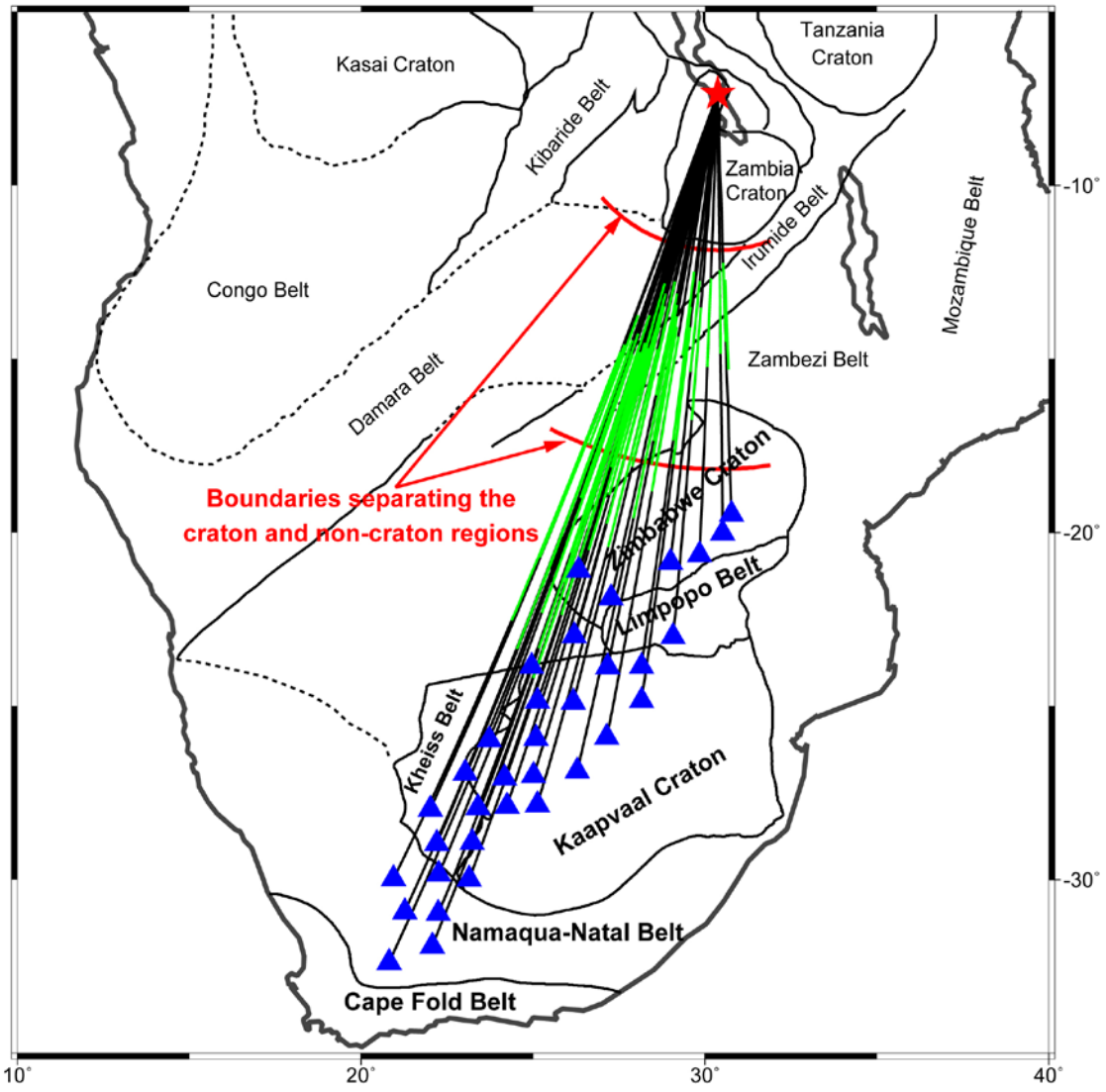

Figure 6. Map showing great circle paths from seismic event (red star) to stations (blue triangles), with the green segments indicating the portions that the BC branch (defined in Figure 7) travels below the lithospheric lid, as well as the geologic provinces in southern Africa. The original time of the earthquake is 1997/09/21/18:16:27 and the event depth is 30 km. Two red lines represent the boundaries of the finite-difference models in the calculations in Figure 14.

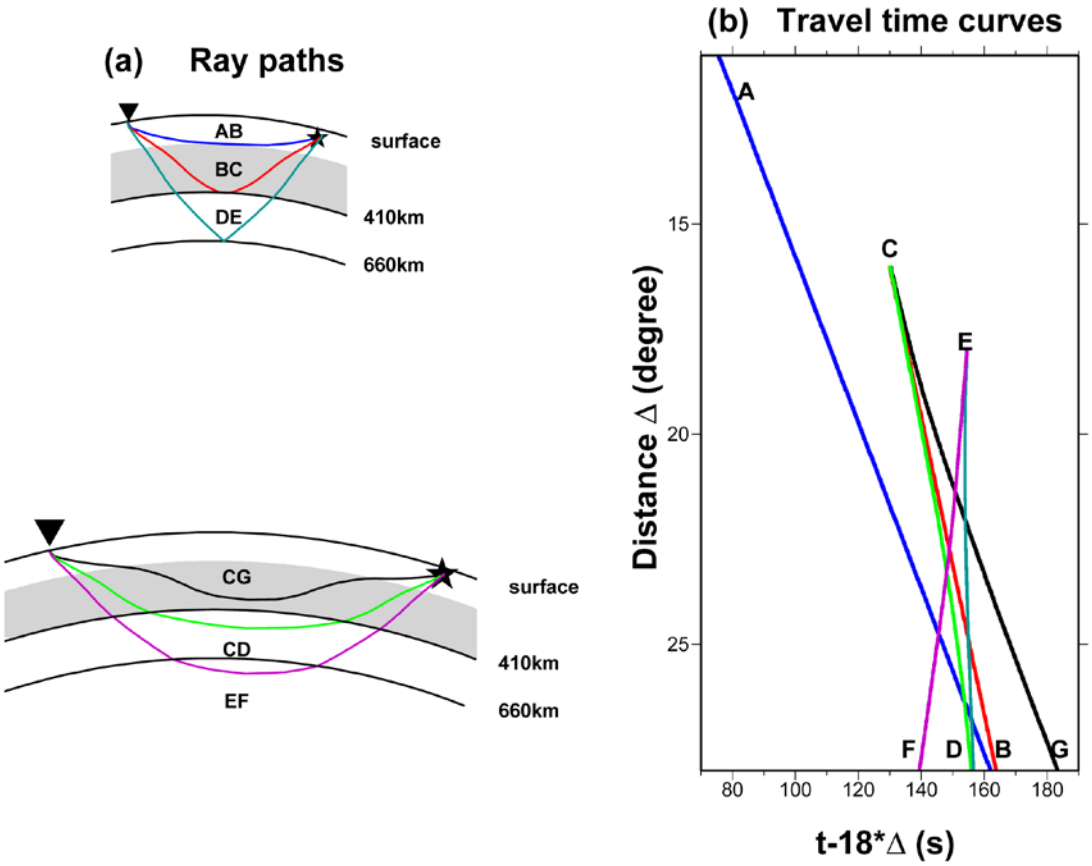

Figure 7. (a) Ray paths (upper for an epicentral distance of 14^{o}; lower for an epicentral distance of 25^{o}) and (b) travel time curves of the triplications in the upper mantle for a source depth of 30 km. The shaded regions in (a) represent the low velocity zone. AB branch is the direct wave propagating above the low velocity zone; BC is the reflection off the 410-km discontinuity; CG is the wave traveling in the low velocity zone; CD is the wave traveling in the transition zone; DE is the reflection off the 660-km discontinuity; and EF is the wave traveling below the 660-km discontinuity.

3.4 Upper mantle shear velocity structure beneath southern Africa

Tangential displacements recorded in the Kaapvaal Array for the event constitute a good record section sampling the seismic shear velocity structure in the upper mantle beneath southern Africa (black traces, Figures 8a, 8b). The event exhibits a simple source time function and three branches of triplications are clearly identifiable in the data. The AB branch turns about 125 km deep in the upper mantle at an epicentral distance of 11^{o},

starts to appear weak at a distance of about 20^o and becomes indiscernible at larger distances. The EF phase crosses over the CD phase at about 23.5^o and samples a depth of 750 km at 27^o (Figures 8a, 8b).

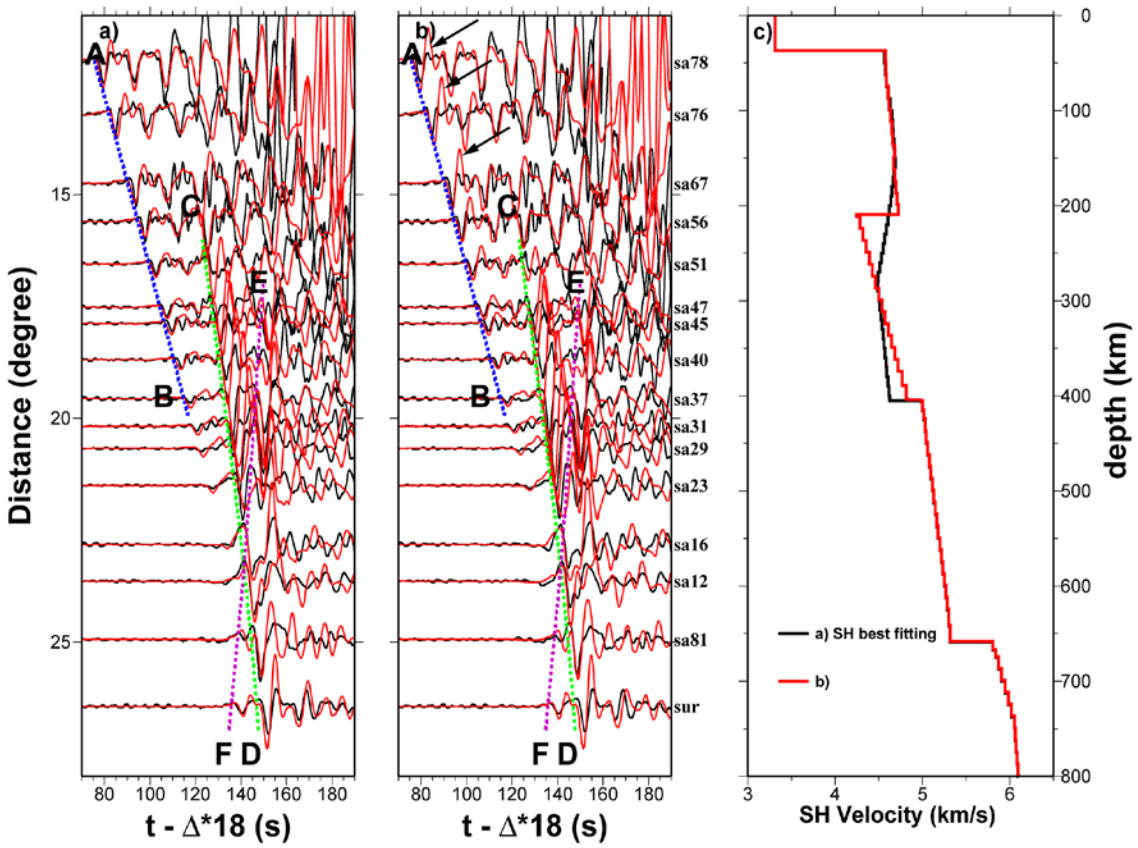

Figure 8. Comparisons of observed tangential displacements for the seismic waves sampling the upper mantle beneath southern Africa (black traces) and synthetic waveforms (red traces) calculated using (a) the best fitting model, with a low velocity zone in a depth range of 150 km to 405 km, and (b) a model with a first order discontinuity at the top of the low velocity zone, along with predicted travel time curves of the three branches of the seismic phases (dashed lines). The predicted travel times of different branches of the seismic phases are also labeled. Models are shown in (c) and labeled accordingly with the synthetics panels.

A low velocity zone beneath the high-velocity lid is needed to explain the amplitude decrease of the AB branch with increasing epicentral distance and its disappearance at the distances larger than 20^o. In the synthetics based on a model without

a low velocity zone, the AB branch extends to an epicentral distance larger than 24^o, while the AB branch disappears around 20^o in the seismic data (Figure 9a). The termination distance of the AB branch is sensitive to the onset depth of the low velocity zone. A shallower onset depth of the low velocity zone would make the AB branch disappear at a smaller distance. The amplitude decrease of AB branch, however, does not permit the detailed feature of the low velocity zone to be resolved. The synthetics (gray traces) based on a model with a gradually changing low velocity zone or a model with a first order discontinuity on the top of the low velocity zone would also fit the amplitude decrease of the AB branch and the travel time difference between the AB and CD branches (Figures 8a, 8b). However, for the model with a first order discontinuity on the top of the low velocity zone, strong reflections off the first order discontinuity (the strong up-swing immediately following the AB branch, pointed by arrows in Figure 8b) can be clearly recognized in the synthetics, while such strong pulses are not present in the seismic data. Thus, the model with a gradually changing low velocity zone is favored by the seismic data. The top of the low velocity zone is 150 km deep and the shear velocity reduction is -8.5% (model a, Figure 8c).

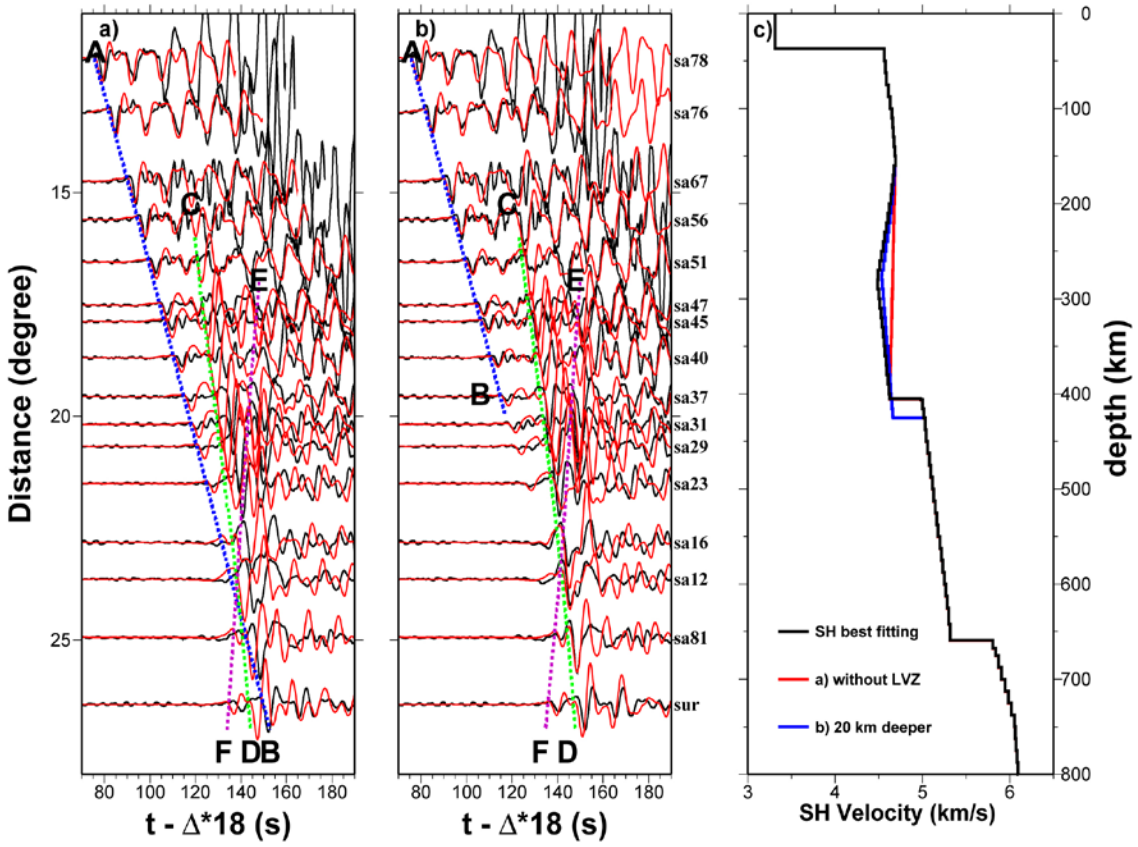

Figure 9. Comparisons of observed tangential displacements (black traces) and synthetic waveforms (red traces) calculated using models perturbed from the S wave best fitting model: (a) without a low velocity zone and (b) with a 20 km deeper 410-km discontinuity and a smaller velocity reduction in the low velocity zone, along with predicted travel time curves of the three branches of the seismic phases (dashed lines). Models are shown in (c) and labeled accordingly with the synthetics panels.

In explaining the seismic data, however, there is a trade-off between the shear velocity reduction in the low velocity zone and the depth of the 410-km discontinuity. For example, the synthetics calculated based on a model with a 20 km deeper 410-km discontinuity and a smaller velocity reduction in the low velocity zone could fit the seismic data equally well (Figure 9b). Despite the trade-offs, synthetic tests indicate that a low velocity zone with a minimum velocity reduction of -5% (which would be

associated with a 20 km deeper 410-km discontinuity) is required to explain the seismic data.

The absolute S wave velocities and the velocity gradient in the transition zone (0.0013 (km/s)/km) are well constrained by the absolute travel time and the move-out of the CD branch. A larger velocity would make the CD branch arrive earlier, and a larger velocity gradient would cause a larger move-out of the CD branch.

The S wave velocity jump across the 660-km discontinuity (0.5 km/s) is also well constrained by the travel time difference between the CD and EF branches. A larger velocity jump would make the CD branch arrive relatively later or the EF branch relatively earlier, i.e., a larger travel time difference between the CD and EF branches. A smaller velocity jump would do the opposite.

3.5 Upper manlte compressional velocity structure beneath southern Africa

Only two branches of triplications (the AB and CD branches) are clearly identifiable in the observed vertical displacements (Figures 10a, 10b). The AB branch turns about 140 km deep in the upper mantle at an epicentral distance of 11^o. The CD phase samples the transition zone to a depth of 660 km at 27^o. The AB branch can be clearly observed in the data until at a distance of about 17^o and becomes indiscernible at larger distances (Figures 10a, 10b).

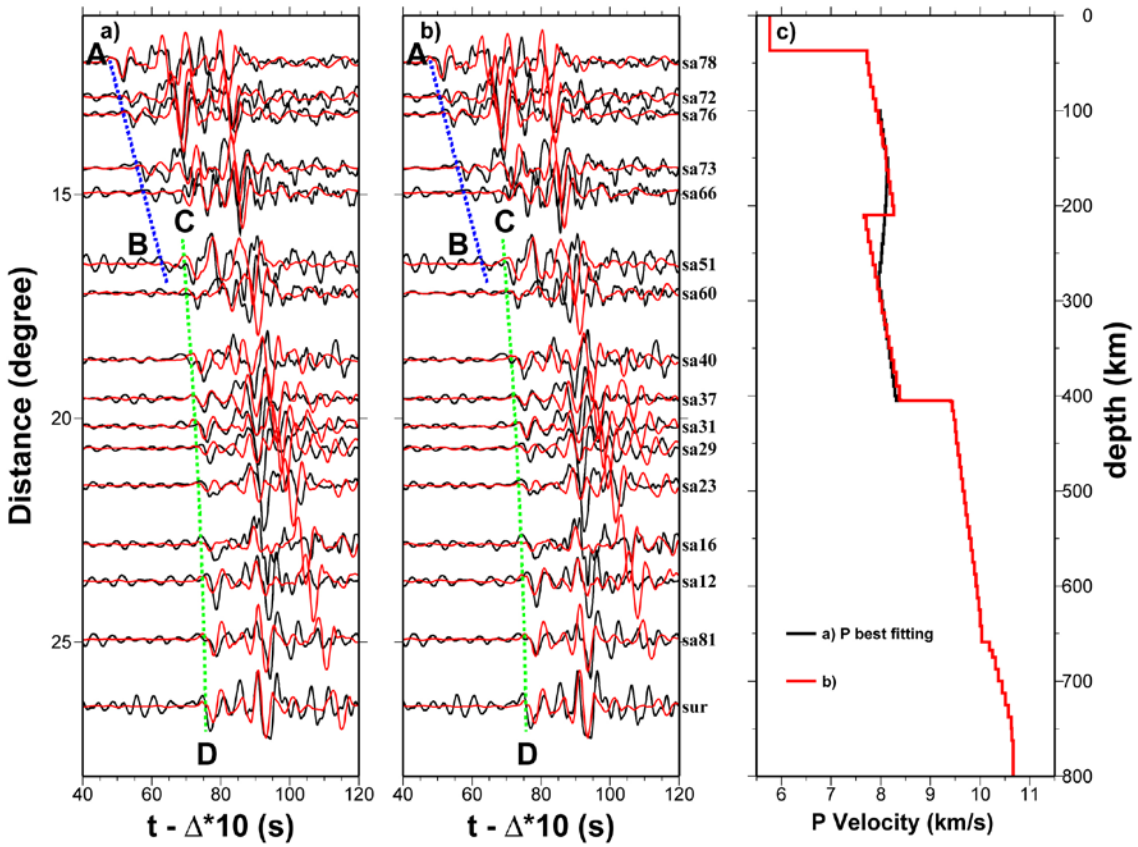

Figure 10. Comparisons of observed vertical displacements for the seismic waves sampling the upper mantle beneath southern Africa (black traces) and synthetic waveforms (red traces) calculated using (a) the best fitting model, with a low velocity zone in a depth range of 150 km to 405 km, and (b) a model with a first order discontinuity at the top of low velocity zone, along with predicted travel time curves of the two branches of the seismic phases (dashed lines). Models are shown in (c) and labeled accordingly with the synthetics panels.

A low velocity zone for the P waves is also required to satisfy the travel time difference between the AB and CD branches. In explaining the P wave data, the P velocity in the depth range between 150 km and the 410-km discontinuity trades off with the assumed depth of the 410-km discontinuity. A model with a deeper 410-km discontinuity would require a smaller velocity reduction in the depth range between 150 km and the 410-km discontinuity. A low velocity zone would not be required for the P

wave data if the 410-km discontinuity is placed 30 km deeper (Figure 11a). However, a 30-km deeper 410-km discontinuity would no longer fit the SH data (Figure 11b), because the small shear velocity reduction required for a 30 km deeper discontinuity would generate a larger termination distance of the AB phase in SH synthetics than in the data. Thus, a low velocity zone above the transition zone is also required for the P data, and the minimum reduction of P velocity in the low velocity zone is -2%, associated with a 20 km deeper 410-km discontinuity.

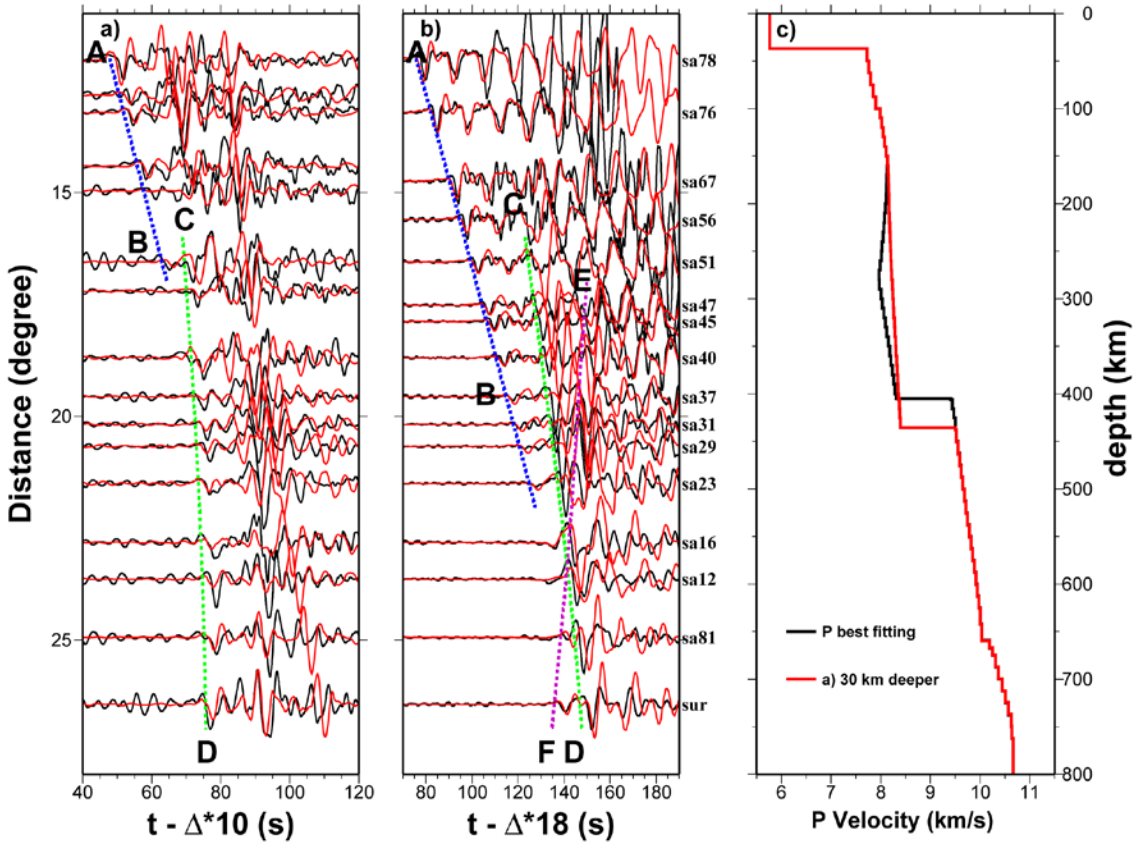

Figure 11. (a) Comparisons of observed vertical displacements (black traces) and synthetic waveforms (red traces) calculated using models perturbed from the P wave best fitting model, without a low velocity zone and with a 30 km deeper 410-km discontinuity and (b) comparisons of observed tangential displacements (black traces) and synthetic waveforms (gray traces) calculated using models perturbed from the S wave best fitting model, with a 30 km deeper 410-km discontinuity and a smaller velocity reduction in the

low velocity zone, along with predicted travel time curves of the seismic phases (dashed lines). Model (a) and the best fitting P model are shown in (c).

The P wave data, however, cannot resolve detailed feature of the low-velocity zone and the inferred P velocity reduction in the low velocity zone would also depend on the assumed feature of the low velocity zone. The synthetics (gray traces) calculated based on a model with a gradually changing low velocity zone or a model with a first order discontinuity on the top of the low velocity zone would fit the seismic data equally well (Figures 10a, 10b). Since the low velocity zone with a first order discontinuity cannot explain the tangential seismic data, we adopt a P velocity model with a gradually changing low velocity zone. In this model, the top of the low velocity zone is 150 km deep and the velocity reduction is -2% (model a, Figure 10c).

The P and SH data also indicate different P to S velocity ratios in the lithospheric lid and in the transition zone. Such feature is well resolved. A uniform P/S velocity ratio in the upper mantle cannot explain the seismic data in the whole distance range. For example, a P velocity model uniformly scaled from the best-fitting S velocity model to fit the arrival times of the AB phase would predict a CD branch much later than that in the seismic data (Figure 12a).

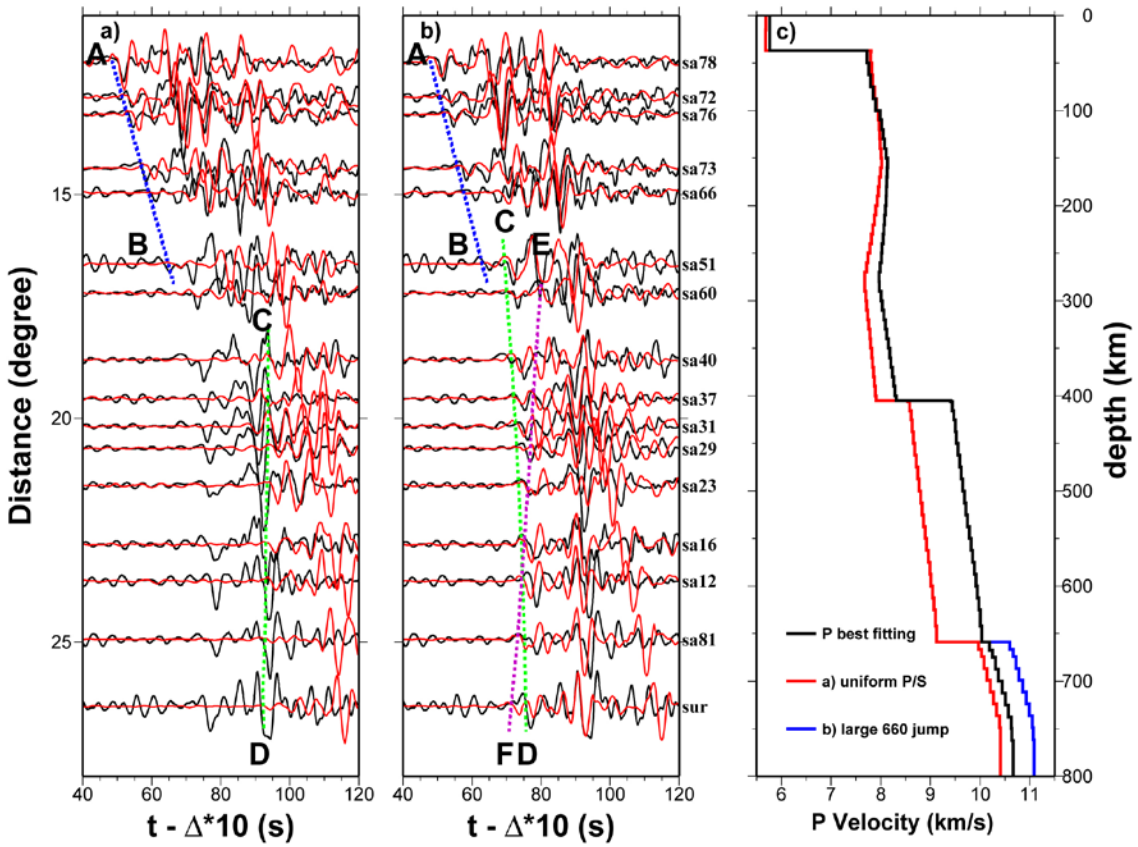

Figure 12. Comparisons of observed vertical displacements (black traces) and synthetic waveforms (red traces) calculated using (a) a model converted from the S wave best fitting model with a uniform P to S ratio and (b) a model perturbed form the P wave best fitting model with a larger velocity jump across the 660-km discontinuity, along with predicted travel time curves of the two branches of the seismic phases (dashed lines). Models are shown in (c) and labeled accordingly with the synthetics panels.

The triplication associated with the 660-km discontinuity (the waves reflected off and traveling below the 660-km discontinuity), while it is clear in the SH wave data, cannot be recognized in the P wave data. This suggests a small P velocity jump less than 4% across the 660-km discontinuity. A larger P velocity contrast across the discontinuity would predict strong triplication phases of the 660-km discontinuity that are not observed in the data (see Figure 12b for an example for the synthetics predicted by a model with a velocity jump larger than 4% across the 660-km discontinuity). The large SH velocity

jump and the small P velocity jump suggest a bulk sound velocity decrease across the 660-km discontinuity.

3.6 Thermal, compositional and mineralogical models of the upper mantle beneath southern Africa

In this section, we infer mantle thermal and compositional models beneath southern Africa through quantitative comparisons between the seismic models obtained from modeling the seismic data and the velocity structures predicted based on various thermal and compositional models. We also explore the mineralogical models associated with the various mantle temperature and composition. In mineral physics modeling, seismic velocities in the upper mantle are calculated following the procedures outlined in Chapter 2.

3.6.1 Low velocity zone

The low velocity zone beneath the lithospheric lid can be explained by a high temperature gradient or partial melt. The availability of both P and S velocity profiles would allow me to distinguish these two possibilities. Temperature would affect both bulk and shear moduli of the minerals, while partial melt would only mostly affect shear module. The velocity reductions in the low velocity zone in our best fitting model would suggest decreases of both shear and bulk moduli, so a high temperature gradient is a more likely explanation. A temperature gradient of about 6 $^{o}C/km$ in the depth range of 150-275 km (Figure 13d) is needed to satisfy the minimal shear velocity reduction of -5% inferred for the low velocity zone beneath southern Africa. Such a temperature gradient

would indicate that the mantle density in the low velocity zone is about 4% smaller than the density in lithospheric lid. If partial melt is involved, presence of water or other volatile elements would be required in the depth range of the low velocity zone to suppress the solidus, as the solidus of the dry peridotite (*Zhang, 1994*) would be higher than the inferred temperature, even with a temperature gradient of 6 $^{o}C/km$ (Figure 13d).

3.6.2 Different P/S ratios in the lithospheric lid and the transition zone

The different P to S velocity ratios between the lithospheric lid and the transition zone can be explained by a difference in aluminum content of the mantle composition in the two depth regions. A higher aluminum content would result in more garnet and less clinopyroxene and orthopyroxene (Figure 13f). Because the bulk modulus of garnet is much larger than those of clinopyroxene and orthopyroxene, and the shear modulus of garnet is only slightly larger than those of clinopyroxene and orthopyroxene, a higher aluminum content would cause a higher P wave velocity, but a similar S wave velocity and, thus, a higher P to S velocity ratio. In the lithospheric lid, a compositional model with an aluminum content of 1% can explain the absolute seismic velocities and the P to S velocity ratio. A lower aluminum content results in more clinopyroxene and orthopyroxene and less garnet (Figure 13e) and thus a lower P/S velocity ratio (Figure 13c) in the lithospheric lid. In the transition zone, the higher P to S velocity ratio requires a higher aluminum content of 4%. A higher aluminum content results in more garnet and less clinopyroxene and orthopyroxene in the transition zone, and thus a higher P to S velocity ratio (Figure 13c). The lower Al content inferred for the lithospheric lid could result from the depletion of the basaltic component of the mantle composition beneath the

old continental nuclei, consistent with the tectnosphere hypothesis beneath the continental cratons (*Jordan, 1978*).

3.6.3 The bulk sound velocity decrease across the 660-km discontinuity

The PREM-like SH velocity jump and a small P velocity jump across the 660-km discontinuity suggest a bulk sound velocity decrease of 3.4% across the 660-km discontinuity. The decrease in bulk sound velocity across the 660-km discontinuity seems to be consistent with the results from the first principle calculation for the ringwoodite (pure Mg_2SiO_4 , without Fe and Al) to perovskite and magnesiowustite phase transformation by *Yu et al.* (2007), which find a bulk sound velocity decrease of $0.1 \pm$ 0.48% across the phase transformation boundary. But, the bulk sound velocity reduction is much larger in the seismic results than in the first principle calculations. Base on current estimates of elastic properties of mantle phases, we are not able to predict a bulk sound velocity decrease with a magnitude of 3.4%. Such a large decrease of bulk sound velocity would require the bulk module of perovskite to be similar to those of ringwoodite and garnet at the pressure and temperature conditions around the 660-km discontinuity, a result remained to be confirmed by experimental or theoretical studies.

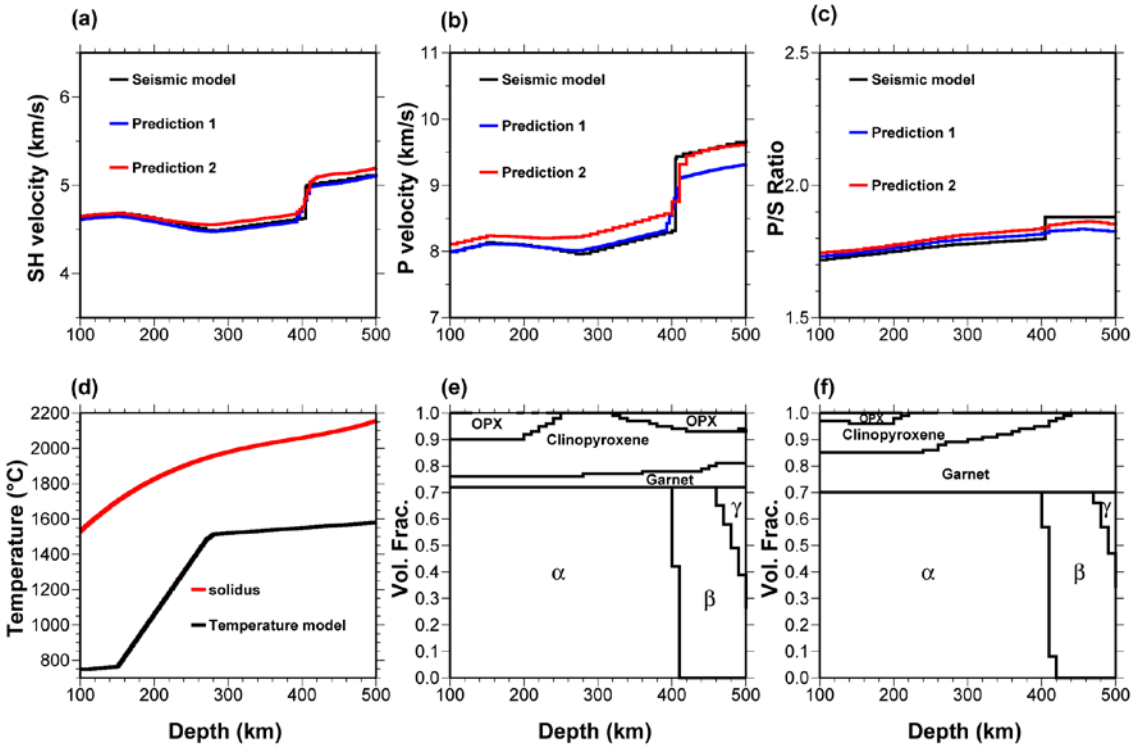

Figure 13. (a-c) comparisons between seismic velocity models and the predictions based on two mantle compositional models, (a) for S wave velocities, (b) for P wave velocities and (c) for P to S velocity ratios; (d) thermal model and the solidus for the anhydrous peridotite (*Jordan, 1978*); and (e-f) mineralogical models predicted based on the thermal model in (d) and two mantle compositional models with Al contents of 1% (e) and 4% (f). α denotes olivine; β wadsleyite; γ ringwoodite; OPX orthopyroxene.

3.7 Discussions

3.7.1 Effects of lateral variation of seismic structure on the inference of the low velocity zone

The primary evidence for the existence of a low velocity zone beneath the lithosphere in southern Africa is the decreasing amplitude and eventual disappearance of the AB branch observed at large distances in the SH data (Figure 8a); and the above inference of the low velocity zone is based on one-dimensional (1-D) seismic modeling. However, the Kaapvaal Seismic Array locates across several cratons (the Kaapvaal

Craton, the Limpopo Belt, the Zimbabwe Craton, the Kheiss Belt and the Namaqua-Natal Belt) and the epicenter of the event is in another craton, the Zambia Craton (Figure 6). Seismic waves sample regions across the Zambia Craton, the non-cratonic regions of the Irumide Belt and the Zambezi Belt, and the cratonic region of the Zimbabwe Craton, the Limpopo Belt and the Kaapvaal Craton (Figure 6). Lateral variation of velocity exists along the seismic paths and it is important to access the effects of the lateral velocity variation on the amplitude of the AB branch. I use a finite-difference method (*Vidale and Helmberger, 1987*) and test many two-dimensional (2-D) seismic velocity models to study such effects. Based on *Li & Burke*'s (2006) three-dimensional (3-D) S wave velocity model, the lateral variations between the Kaapvaal Craton, the Limpopo Belt, the Zimbabwe Craton, the Kheiss Belt and the Namaqua-Natal Belt are small, so we approximate them as one region with a 1-D velocity structure. Based on Priestley et. al.'s SV-velocity model in southern Africa (*Priestley, 2006*), at depths of 150 km and 250 km, the Zambia Craton and the Zimbabwe Craton have almost the same velocity, so we also used the 1D cratonic velocity model for the Zambia Craton. We thus test 2-D models that comprise of two different 1-D SH velocity structures along the paths, representing the velocity structures in and out of the cratons, respectively. We show synthetic examples for models with the boundaries that separate the cratonic and non-cratonic regions shown in Figure 6. The boundary between the non-craton region and the Zimbabwe Craton in these example models do not exactly coincide with the geological boundary of the Zimbabwe Craton, but finite-difference models with boundaries coinciding with the northernmost and southernmost the Zimbabwe Craton show similar results discussed below. Synthetics show that models with lateral velocity variation in the

lithospheres, but without a low-velocity zone beneath the lithospheric lid, cannot explain the seismic data. Models with the non-cratonic region having same velocity gradient as in the cratonic region, but having smaller absolute velocities, cannot generate the distance dependence of the amplitude of the AB phase as observed in the data (Figure 14a). Models with a larger velocity gradient in the non-cratonic region could generate a decrease of the amplitude of the AB phase with increasing epicentral distance in the synthetics. But the predicted change is much smaller than the observed and the predicted AB termination distance is much larger than what observed in the data. Even if we adopt a velocity gradient of 0.004712 km/s/km in the non-cratonic region, a gradient that would generate much larger travel times and a very different move-out of the AB phases than observed (Figure 14c), the synthetics based on this model cannot fit the distance dependence of the AB amplitude and the AB termination distance observed in the seismic SH data (Figure 14b). We thus conclude that the velocity variations between the cratonic and non-cratonic regions cannot explain the observed distance dependence of amplitude and the eventual termination of the AB phase at large distances in the seismic data. A low velocity zone beneath the lithospheric lid is required to explain these waveform characteristics.

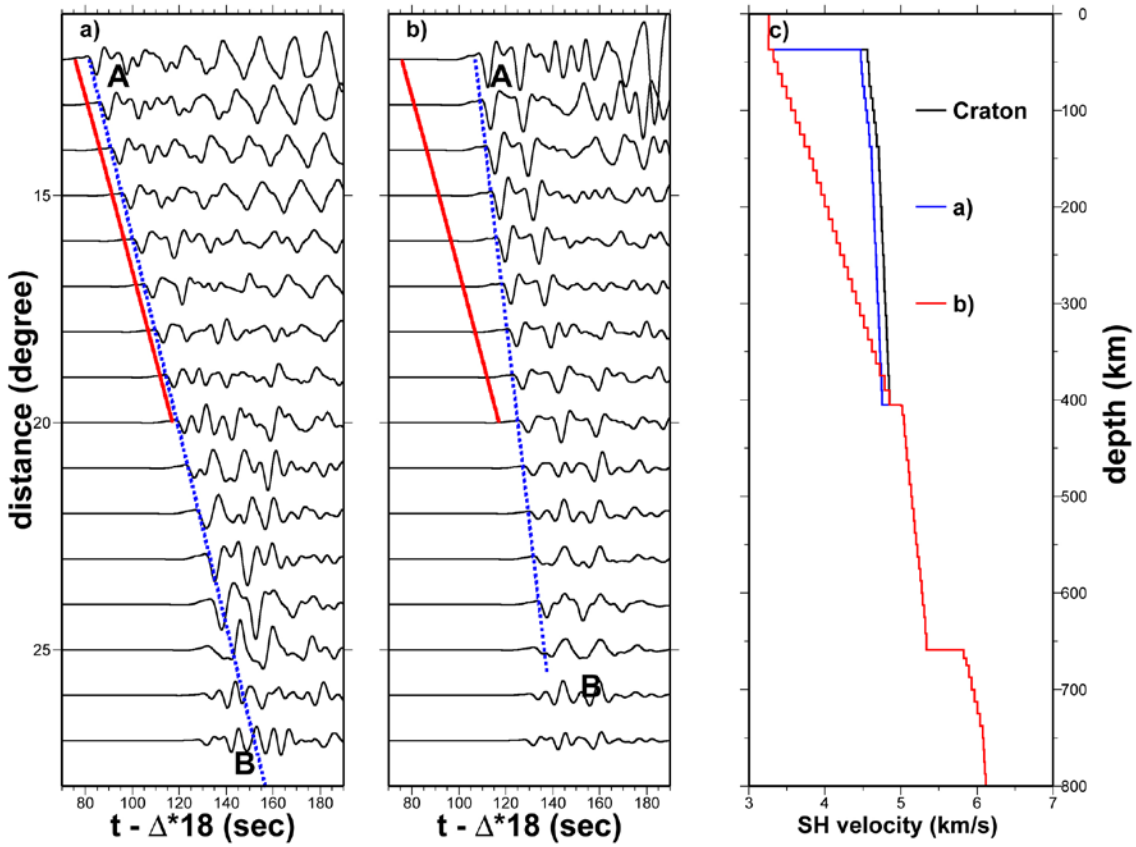

Figure 14. SH finite difference synthetic waveforms calculated based on two models with same SH velocity structure in the cratonic regions and two different SH velocity structures in the non-cratonic region having (a) a smaller absolute velocity and (b) a large velocity gradient in the lithospheric lid, along with predicted (blue dashed lines) and observed (red solid lines) travel time curves of the AB branch. Velocity models are shown in (c) and labeled accordingly with the synthetics panels.

3.7.2 Attenuation effect

We did not include attenuation effect in our synthetic calculations. A very high attenuation channel in the depths of the low velocity zone would generate an amplitude decrease of the AB phase at large epicentral distances, similar to the effect of a low velocity zone. However, synthetics tests indicate that such a high attenuation channel would also generate small amplitudes of the CD and EF phases and cannot explain the observed amplitude ratios between the CD and AB branches in the epicentral distance

range between 15^o and 22^o, and the observed amplitudes of the EF branch at large distances. Thus, the seismic data cannot be explained by attenuation effect; a low velocity zone is required. Synthetics tests further indicate that attenuation affects little the inference of the different P/S ratios between the lithospheric lid and the transition zone.

3.7.3 Comparisons with other models in southern Africa

Although different types of the seismic data were used, our best-fitting S velocity model is similar to the results of most of the previous surface wave studies. Earlier surface wave studies (*Bloch et al., 1969; Qiu et al., 1996*) showed a thinner lithospheric lid and a stronger S wave low velocity zone than our best-fitting model beneath southern Africa. Later studies (*Priestly, 1999; Priestly, 2006; Li and Burke, 2006*), however, indicated a model similar to our best-fitting SH velocity model, in having similar thickness and onset depth and magnitude of S wave velocity reduction of the low velocity zone. Freybourger et al. (*Freybourger, 2001*) found that the upper mantle beneath the Kaapvaal Craton is anisotropic from beneath the Moho to about 100 km depth, using the fundamental modes of the Love and Rayleigh wave phase velocities, but most of other studies did not find any evidence of anisotropy in this region (*Qiu et al., 1996; Priestly, 1999*). The fact that a low velocity zone was also present in the Rayleigh wave studies (*Priestly, 2006; Li and Burke, 2006*) suggests that the presence of the low velocity zone beneath the lithospheric lid is not the result of seismic anisotropy. The seismic data we used permit us to resolve several additional important features of the seismic structure that the surface wave data did not, including the velocity gradients in the lithospheric lid

and the transition zone, velocity structure below 400 km, and both P and S velocity structures.

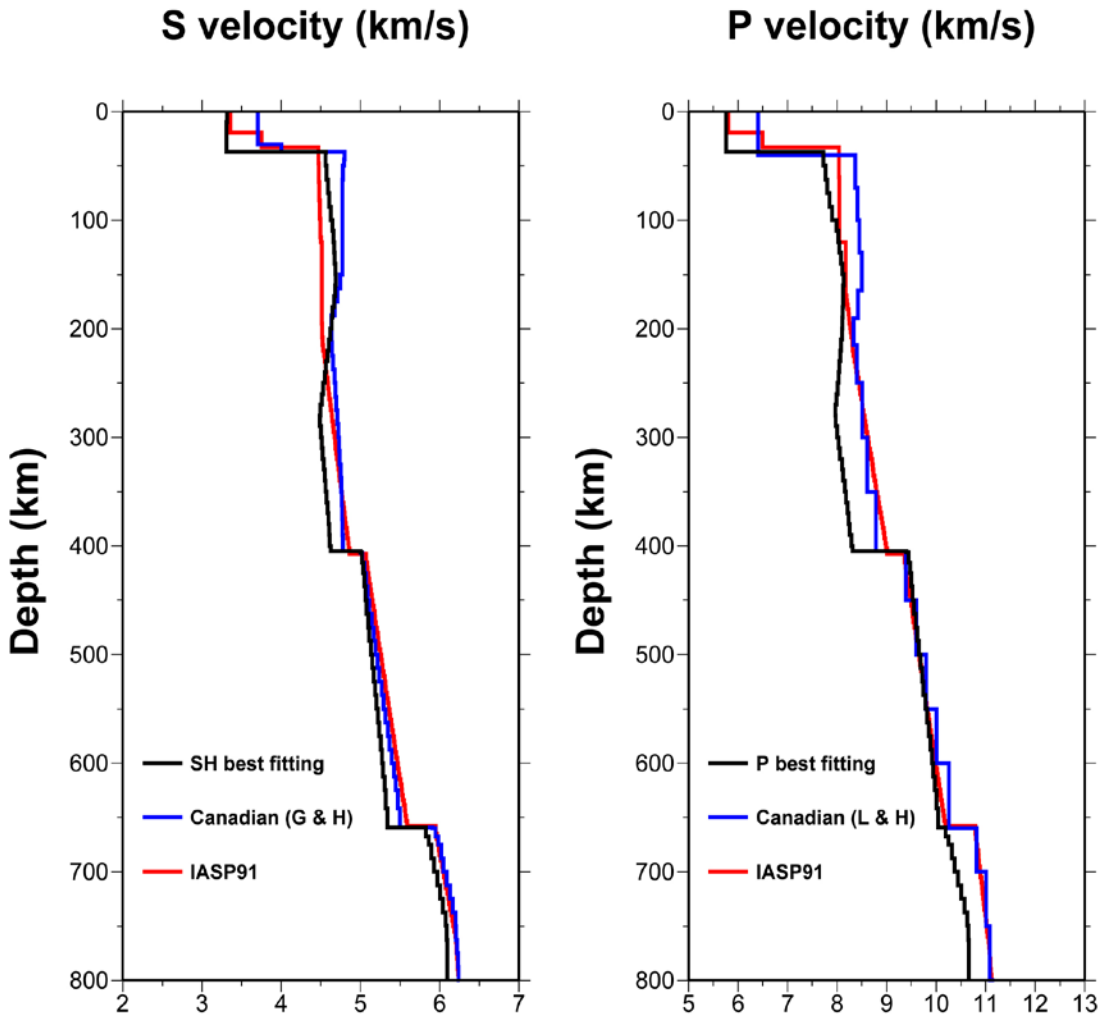

Figure 15. Comparisons between our best fitting models, two published upper mantle velocity models for the Canadian Shield, Canadian (G & H) (*Grand and Helmberger, 1984a*) and Canadian (L & H) (*LeFevre and Helmberger, 1989*), and IASP91(*Kennett, 1991*): (a) for S velocity and (b) for P velocity.

Receiver function (*Vinnik et al., 1996; Gao et al., 2002; Stankiewicz et al., 2002*) indicated that the thickness of the transition zone is similar to the global average and suggested that the transition zone beneath southern Africa is not anomalously warm.

Some receiver function study (*Gao et al., 2002*) did not find evidence for a low velocity zone, while others (*Vinnik et al., 1996; Stankiewicz et al., 2002*) found a weaker and deeper (> 300 km) S wave low velocity zone than that in our best-fitting SH velocity model. In those receiver function studies, the thickness of the transition zone and the depths of the discontinuities are inferred on the basis of the IASP91 (*Kennett, 1991*) model, which is different from our best-fitting southern Africa velocity model (Figure 15). Thus, the inferred transition zone thickness and discontinuity depths could be different sbetween different studies.

There are also many studies using triplication data in southern Africa (*Zhao et al., 1999; Simon et al., 2002; Wright et al., 2002; Simon et al., 2003; Wright et al., 2004*). *Zhao et al.* (1999) used both travel time and waveform data to constrain the P and S velocity models in the upper mantle beneath southern Africa. Because of the absence of the P waveform data from the epicentral distances less than 2200 km, they could not constrain the detailed velocity structure in the top 300 km of the mantle. Lack of S data prevented them from constraining detailed S velocity structure in the region. Using travel time and waveform information of the triplication data, *Simon et al.* (2002, 2003) and Wright et al. (*Wright et al., 2002; Wright et al., 2004*) inferred an S velocity model that has a lithospheric lid with a smaller thickness and similar velocities as our best-fitting SH velocity model, a low velocity zone with a first order discontinuity and a smaller velocity reduction, and a larger velocity gradient and larger velocities in the transition zone. Their P velocity model has larger velocities in the lithospheric lid and does not have a low velocity zone in the upper mantle. The sampling region of their seismic data is a broad region of southern Africa, including the Zimbabwe Craton, the Limpopo Belt, the

Kaapvaal Craton, the Namaqua-Natal mobile Belt and the Cape Fold Belt, while our sampling region is only the western part of the Zimbabwe Craton and some non-cratonic regions (Figure 6). The difference in sampling region in their studies may cause those velocity model differences.

3.7.4 Comparison to velocity models for the Canadian Shield

Our best fitting models exhibit similar characteristics as the P and S velocity model for the Canadian Shield (*Grand and Helmberger, 1984a; LeFevre and Helmberger, 1989*) in having a high-velocity lithospheric lid overlying a low velocity zone (Figure 15). However, our best fitting models have lower absolute P and S velocities in the lithospheric lid and a thinner low velocity zone with much larger velocity reductions. The P velocity jump across the 660-km discontinuity beneath the Canadian Shield is larger than that beneath southern Africa. The S wave model for the Canadian Shield was derived using travel times of S and SS phases recorded in the epicentral distance range of $10^o - 60^o$ (*Grand and Helmberger, 1984a)* and the P wave model for the Canadian Shield was derived using waveform modeling Pnl, P and PP phases (*LeFevre and Helmberger, 1989*). The lower S and P velocities in the lithospheric lid in our model suggest a higher mantle temperature or a lower Al content, or both, in the lithospheric lid in southern Africa than that in the Canadian Shield. The thinner low velocity zone suggests that a thinner layer of the high temperature gradient. The P/S velocity ratios in the lithospheric lid and in the transition zone beneath the Canadian Shield can be explained by a uniform Al content of 4%. Since the P and S velocity models for the Canadian Shield were derived in different studies and were constrained by different seismic datasets, it is

unclear that an uniform Al content for both the lithospheric lid and the transition zone found for the Canadian Shield is due to the fact that different datasets were used to inferred the P and S velocity models and the uncertainties are different for these P and S velocity models, or the Al contents in the lithospheric lids are different between the Canadian Shield and southern Africa.

3.8 Implications to the origin of the "African Superswell"

The presence of a low velocity zone with large velocity reductions in the upper mantle beneath southern Africa suggests a low-density anomaly in the upper mantle beneath southern Africa. The presence of a low-density anomaly beneath the lithospheric lid is consistent with the observed localized uplift and broad geoid anomalies in the region of the "African Superswell". The shallow low-density buoyancy generates large uplifts in the region, but little localized geoid anomaly because of the near-perfect compensation of the topography (*Wen and Anderson, 1997; Richards and Hager, 1984*). In this case, the localized uplift is caused by the low-density anomaly in the low-velocity zone beneath the lithospheric lid, while the geoid anomaly observed in a broader region of Africa may be attributed to the large-scale density anomalies in the lower mantle (*Wang and Wen, 2007*). The presence of a high temperature anomaly in the shallow mantle is also consistent with the high heat flow observed on the ocean floor of the "African Superswell" (*Nyblade and Robinson, 1994*).

3.9 Conclusions

We study seismic SH and P velocity structures, mineralogical, thermal and compositional models in the upper mantle beneath southern Africa, through joint modeling of seismic and mineral physics data. Our seismic data consist of the tangential and vertical components of triplicated phases recorded in the epicentral distance range of 11^{o}- 28^{o} for a shallow event occurring in southern Africa. The data suggest that the lithospheric lid is about 150 km thick, a low velocity zone below the lithospheric lid beneath southern Africa exists for both P and S velocity structures with velocity reductions of at least –5% for S waves and –2% for P waves, the P to S velocity ratio in the transition zone (1.88) is larger than in the lithospheric lid (1.70), and bulk sound velocity decreases about 3.4% across the 660-km discontinuity.

We infer mantle thermal and compositional models in this region through quantitative comparisons between the P and S seismic models obtained from modeling the seismic data and the velocity structures predicted based on various mantle thermal and compositional models. The low velocity zone can be explained by a high temperature gradient of $6\,^{o}C/km$ or presence of partial melt. The presence of partial melt would require presence of water or other volatile elements in depth range of the low velocity zone to lower the solidus. The difference in P to S ratio between the transition zone and the lithospheric lid can be explained by aluminum contents of 4% in the transition zone and 1% in the lithospheric lid. The inferred lower Al content in the lithospheric lid is consistent with the basaltic depletion in the cratonic tectnosphere. The inferred large decrease of bulk sound velocity of 3.4% across the 660-km discontinuity would be possible only if the bulk module of perovskite is similar to those of ringwoodite and

garnet at the pressure and temperature conditions of the 660-km discontinuity, a result remained to be confirmed by experimental or theoretical studies.

The presence of a low velocity zone with large velocity reductions in the upper mantle beneath southern Africa suggests existence of a low-density anomaly with a dense perturbation of -4% beneath the lithospheric lid beneath southern Africa. The existence of such a low-density anomaly could explain the observed localized uplift in the “African Superswell” and is consistent with the observed broad distribution of the geoid anomaly in the region.

Chapter 4 SH velocity structures and compositional models near the 660-km discontinuity beneath South America and northeast Asia

4.1 Abstract

We constrain SH wave velocity structures near the 660-km discontinuity beneath South America and northeast Asia, using triplicated phases near the discontinuity recorded in the epicentral distance range of 10^o - 35^o for three deep events. We then explore mineralogical and compositional models appropriate for explaining the inferred seismic structures between the two regions. SH velocity structures near the 660-km discontinuity are found to be different in the two regions. Beneath South America, the velocity gradient above the 660-km discontinuity is larger than that of Preliminary Earth Reference Model (PREM), while the velocity jump across the discontinuity is the same as PREM. Beneath northeast Asia, the velocity gradient above the 660-km discontinuity is the same as that of PREM, while the velocity jump across the discontinuity is larger than PREM. Both regions are characterized by a large velocity gradient extending about 80 km deep below the 660-km discontinuity. The different velocity structures require different mineralogical models in the transition zone in the two regions. The larger velocity gradient above the 660-km discontinuity beneath South America requires

existence of the ilmenite phase in the bottom of transition zone, while that beneath northeast Asia can be explained by the temperature and pressure dependence of elastic properties of the major mantle mineral assemblages. The observed large velocity gradients in the top of the lower mantle can be explained by gradual transformation of garnet to perovskite persisting to greater depths. The velocity jump across the discontinuity beneath South America can be explained by the presence of more garnet above the discontinuity than the pyrolite model, while a larger velocity jump across the discontinuity beneath northeast Asia requires more garnet transforming to perovskite across the discontinuity. These different mineralogical models can be caused by different mantle temperature or composition, especially the aluminum content in mantle composition. The presence of garnet 80 km below the 660-km discontinuity in the two regions may be explained by a uniform composition in the lower mantle with an aluminum content of 3.4%. The existence of ilmenite in the bottom of the transition zone beneath South America and the absence of ilmenite beneath northeast Asia can be explained by either a difference in mantle temperature of about 100 ^{0}C (with that beneath South America being lower) between the two regions assuming a uniform mantle composition, or alternatively, a difference in aluminum content of about 1% (with that beneath South America being lower) between the two regions without invoking a temperature difference between the two regions. We also discuss conditions of mantle composition and temperature that double discontinuities may occur near the 660-km depth, as well as the depth separation and velocity jumps of the double discontinuities. For the inferred mantle temperature and composition beneath South America and

northeast Asia, the maximum separation of the double discontinuities is 20 km and cannot be resolved by the SH wave data.

4.2 Introduction

Understanding the detailed structures and composition near the 660-km discontinuity is important for us to understand mantle dynamics. The endothermic phase transformation from ringwoodite to perovskite plus magnesiowustite may introduce temporary layering through the 660-km discontinuity (*Honda and Balachandar, 1993; Tackley et al, 1993*). However, the 660-km discontinuity is actually caused by at least two phase transformations: from garnet to perovskite and from ringwoodite to perovskite plus magnesiowustite (*Akaogi and Akimoto, 1979; Ito and Takahashi, 1987; Irifune and Ringwood, 1987*). These two phase transformations have different characteristics. While the breakdown of ringwoodite is endothermic, the phase transformation from garnet to perovskite is likely exothermic. These two phase transformations can also interact chemically. The actual paths of the perovskite-forming processes strongly depend on mantle temperature and composition (*Weidner and Wang, 2000*).

While the properties of these phase transformations depend on mantle composition and chemical interaction between the two subsystems in the mantle, they result in different seismic structures near the 660-km discontinuity and can be directly tested using seismic data. For example, the velocity gradient above the 660-discontinuity is sensitive to the presence of ilmenite above the discontinuity. The velocity jump across the 660-km discontinuity is sensitive to the amount of garnet transforming to perovskite across the discontinuity. With increasing amount of experimental data, now we can

quantitatively calculate velocity and density profiles based on different compositional models, so these compositional models can be directly constrained by seismic data.

In this study, we use joint modeling of seismic and mineral physics data to study the seismic SH velocity structures and mineralogical models near the 660-km discontinuity beneath South America and northeast Asia. We adopt waveform modeling to constrain the seismic structure. Synthetics are calculated by the reflectivity programs (*Zhu and Rivera, 2002*). We also explore the conditions of mantle composition and temperature that are appropriate for explaining the inferred mineralogical models between the two regions. We discuss seismic data in Section 4.3, the shear wave velocity structures beneath South America and northeast Asia in Sections 4.4 and 4.5, the compositional and mineralogical models in the two regions in Section 4.6, the possibility of double 660-km discontinuities in Section 4.7, and comparisons with previous studies in Section 4.8.

4.3 Seismic Data

Our study regions are South America and northeast Asia (Figure 16). The velocity structures near the 660-km discontinuity are constrained using triplicated phases recorded in the epicentral distance range of 10^o- 35^o for a deep event occurring in South America subduction zone and two events occurring in northeast Asia (Table 2). In order to minimize the effects of lateral seismic heterogeneities on the seismic wave propagation, we either use the seismic data recorded in seismic arrays or check the consistency of results from the data sampling different directions. The South America event is selected from the seismic data recorded in two PASSCAL experiments (BANJO and BLSP) in

South America for events occurring in the South America subduction zone from January 1994 to September 1995. Note that the seismic data sample the transition zone beneath South America in a small azimuthal range (Figure 16a). The two Asia events are selected from the data recorded at 48 broadband stations in the New Chinese Digital Seismic Network (NCDSN) for events occurring in northeast Asia from August 2001 to February 2004. The two events sample the transition zone in the directions approximately perpendicular to each other (Figure 16b). The signal to noise ratios of the seismic data for these three events are high. Our approach is similar to the seismic studies using triplication phases in the upper mantle distance ranges (*e.g., Helmberger and Wiggins, 1971; Burdick and Helmberger, 1978; Given and Helmberger, 1980; Walck, 1984; Grand and Helmberger, 1984a, 1984b; LeFevre and Helmberger, 1989; Cummins et al, 1992; Houard and Nataf, 1993; Neele, 1996; Brudzinski and Chen, 1997; Melbourne and Helmberger, 1998; Zhao et al., 1999; Brudzinski and Chen, 2000; Brudzinski and Chen, 2003, Chen and Brudzinski, 2003; Song et al., 2004*). In this study, we use deep events to avoid the effect of shallow velocity structures. For a shallow event, the triplications from other shallow discontinuities (e.g., the 410-km discontinuity) will also make waveform complex and phases difficult to be recognized.

Table 2 Event list

NO.	Origin time	Latitude (^oN)	Longtitude (^oE)	Depth (km)
1	1994/11/04 01:13:20	-9.331	-71.308	597
2	2003/07/27 06:25:31	47.15	139.25	477.2
3	2002/08/02 23:11:39	29.35	139.25	441.5

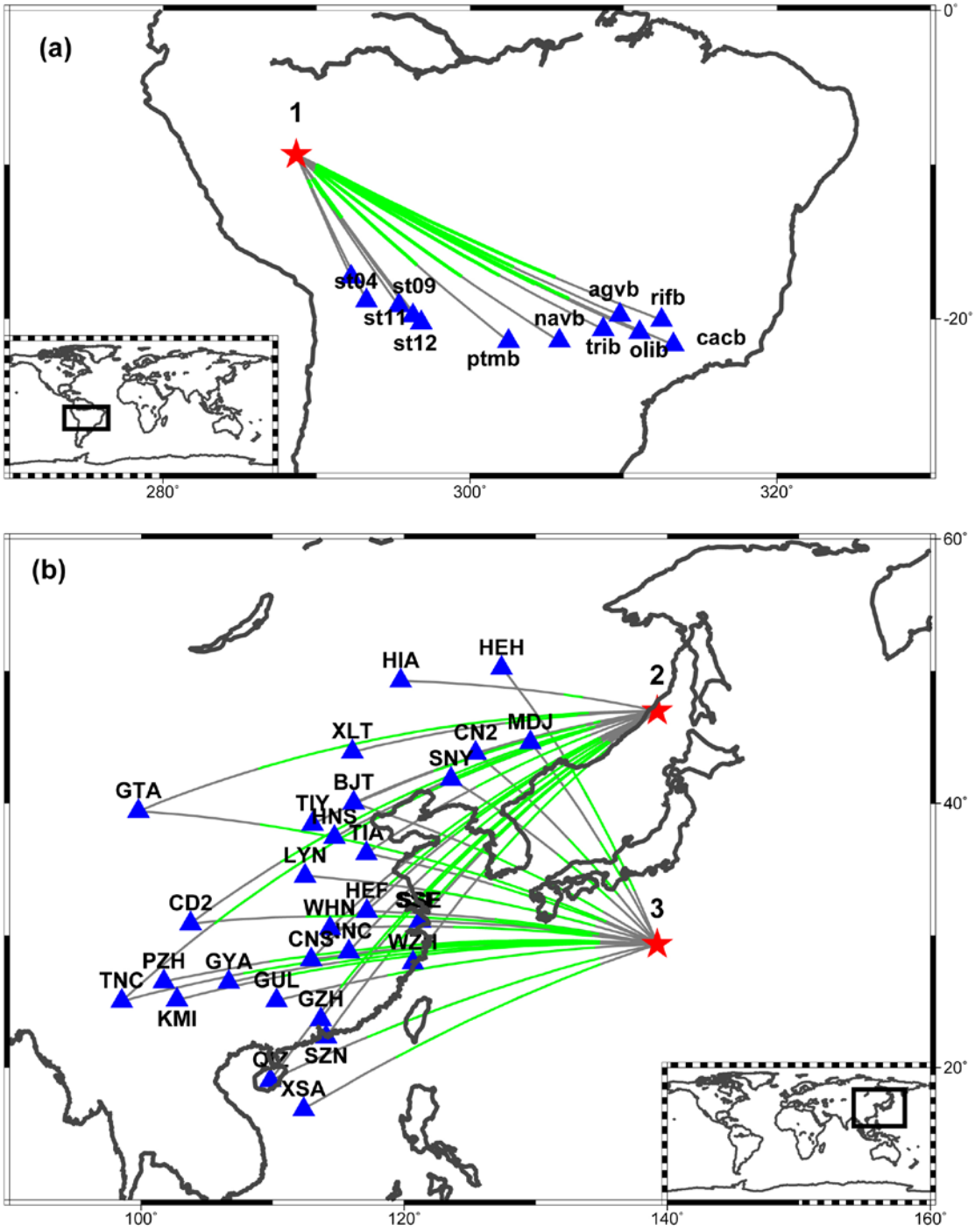

Figure 16. Great circle paths from seismic events (red stars) to stations (blue triangles), with the green segments indicating the portions that the CD branch travels below the 660-km discontinuity, in two study regions: (a) South America (event 1) and (b) northeast Asia (events 2 and 3) (see Table 2 for event information).

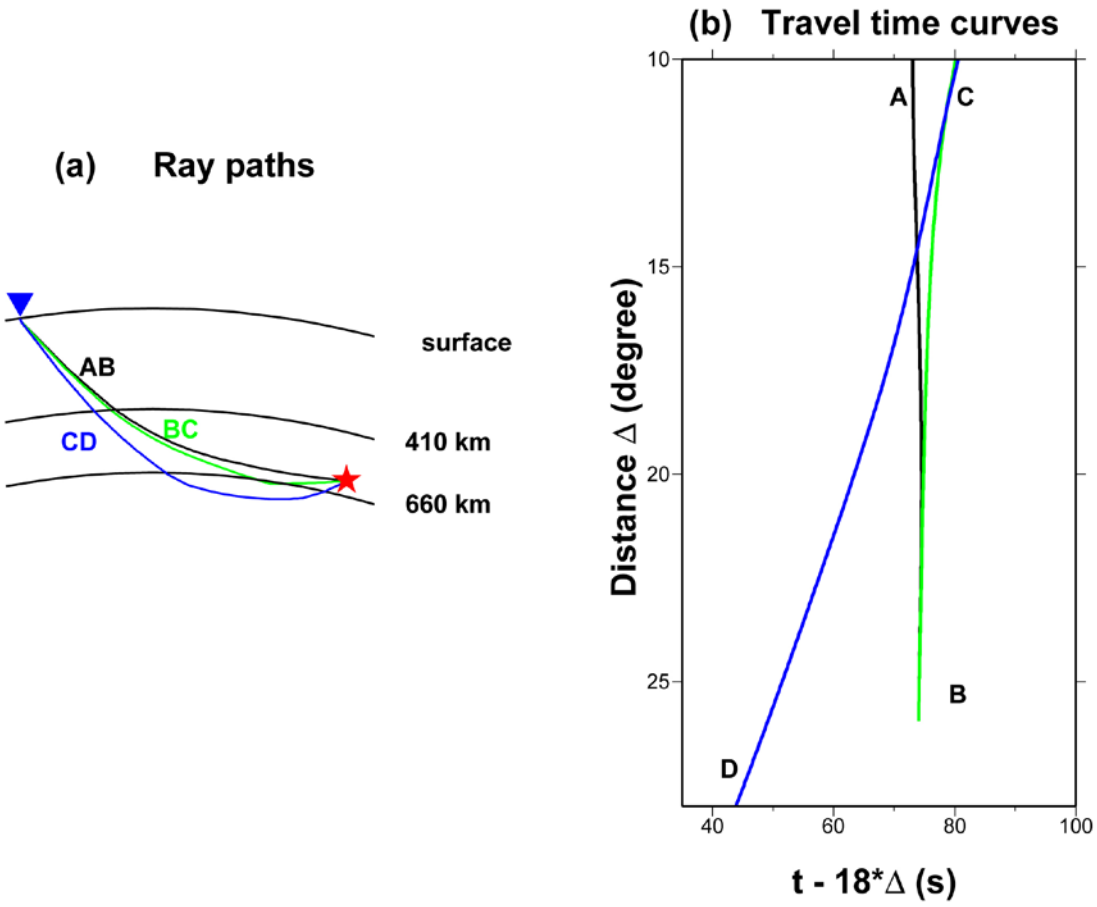

Figure 17. (a) Ray paths and (b) travel time curves of the triplications near the 660-km discontinuity for a source depth of 597 km. The AB branch is the direct SH wave propagating above the discontinuity; the BC branch is the reflection off the discontinuity; and the CD branch is the seismic wave traveling below the discontinuity.

Three seismic phases are used to constrain the velocity structure near the 660-km discontinuity (Figure 17): the wave propagating above the discontinuity (AB branch), the reflection off the discontinuity (BC branch) and the wave traveling below the discontinuity (CD branch). Since the ray paths of these three phases are very close in the shallow proportion of the mantle (Figure 17), the travel time difference and waveform between these phases are primarily sensitive to the velocity structure near the 660-km discontinuity. The termination distance of the AB branch is sensitive to the velocity

gradient above the 660-km discontinuity; the move-out of the CD branch is sensitive to the velocity gradient below the 660-km discontinuity; and the travel time difference between the AB and CD branches is sensitive to the velocity jump across the 660-km discontinuity. The triplication of the 660-km discontinuity occurs in an epicentral distance range of 10^o - 35^o, so the data in this epicentral distance range is used. Seismic data are bandpass filtered in a frequency range of 0.04—0.4 Hz.

4.4 Seismic shear velocity structure beneath South America

Tangential displacements recorded in the two PASSCAL experiments for event 1 constitute a good record section sampling the seismic structure near the 660-km discontinuity beneath South America (black traces, Figures 18a and 18b). The event exhibits a simple source time function and three branches of triplication are clearly identifiable in the distance range of $10^o - 27^o$. The AB branch turns about 600 km deep in the transition zone at an epicentral distance of 10^o and starts to diffract at the top of the 660-km discontinuity at an epicentral distance of about 20^o. The CD phase crosses over the AB phase at about 15^o and samples the top of the lower mantle to a depth of 820 km at 27^o. The AB branch can be clearly observed in the data after the cross-over (see data at stations PTMB, NAVB) untill at a distance of about 20^o and becomes indiscernible at stations TRIB, AGVB, OLIB, RIFB and CACB at larger distances (Figures 18a and 18b).

PREM (*Dziewonski and Anderson, 1981*) cannot explain the seismic data sampling South America. The termination distance of the AB branch is larger in the

PREM synthetics than in the data, and the travel time separation between the AB and BC branches is smaller in the synthetics than in the data (Figure 18a).

A larger velocity gradient above the 660-km discontinuity and a deeper 660-km discontinuity are needed to explain the seismic data for event 1. A larger velocity gradient above the discontinuity would make the AB branch terminated at a closer distance as observed in the data; and a deeper discontinuity would predict a larger travel time difference between the AB and BC branches. We obtain our best-fitting model by searching models with various velocity gradients above the discontinuity and various depths of the discontinuity. The best-fitting model has a velocity gradient of 0.0024 (km/s)/km above the discontinuity and a deeper 660-km discontinuity at 685 km (Figure 18c). Synthetics calculated using this modified model match well the termination distance of the AB branch and the travel time difference between the AB and BC branches (Figure 18b).

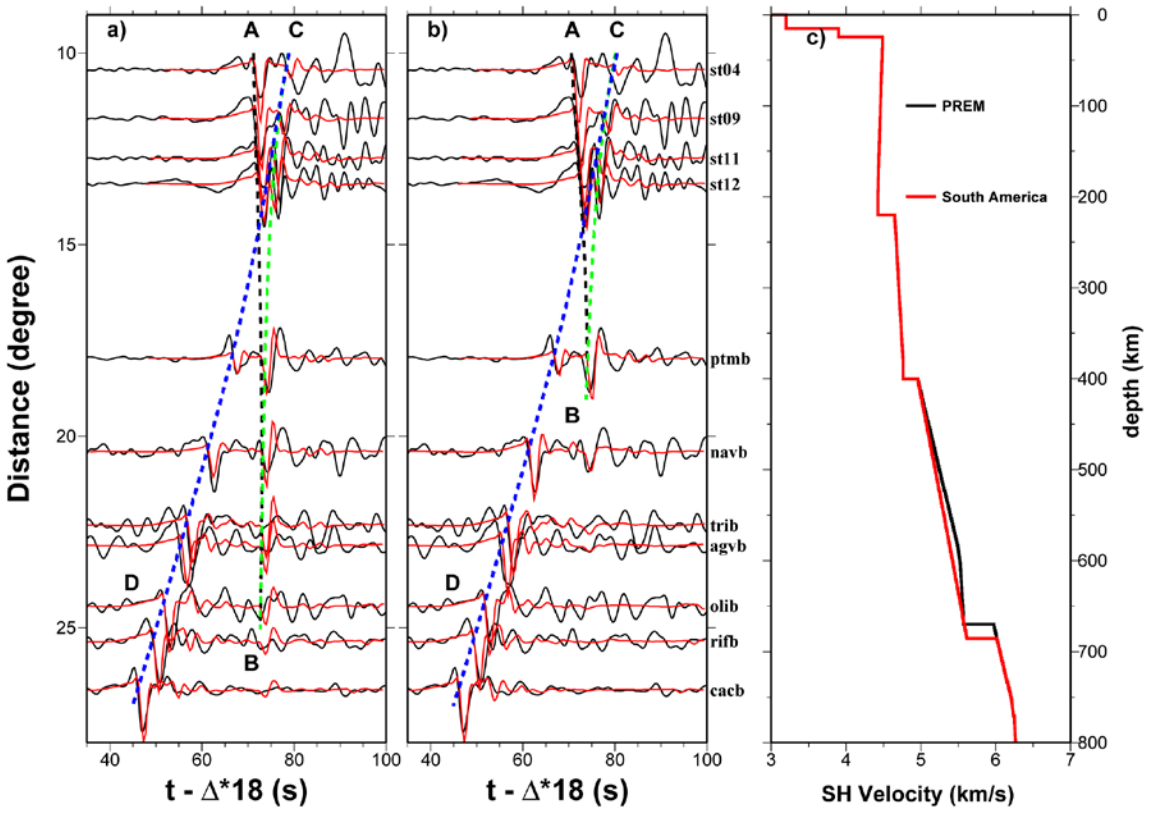

Figure 18. Comparisons of observed tangential displacements for the seismic waves sampling the transition zone beneath South America (event 1) (black traces) and synthetic waveforms (red traces) calculated using (a) PREM and (b) our best fitting model, along with predicted travel time curves of the three branches of the seismic phases (dashed lines). Models are shown in (c). Station travel time corrections are made for following stations: TRIB (-1.5 s), OLIB (-1.0 s), RIFB (-0.5 s), based on the observations from another event.

The velocity jump crosses the 660-km discontinuity and the velocity gradient below the discontinuity in PREM, on the other hand, can well explain the data (Figure 18b). The velocity jump across the 660-km discontinuity and the velocity gradient below the discontinuity are well constrained by the cross-over distance, and the relative timing and move-out of the CD phase observed in the seismic data. For example, synthetic waveforms calculated using a smaller velocity jump across the 660-km discontinuity show a smaller travel time difference between the AB and CD branches than what

observed in the data (Figure 19a). Synthetic waveforms calculated using a smaller velocity gradient below the 660 km discontinuity exhibit a different move-out of the CD branch from that in the data (Figure 19b).

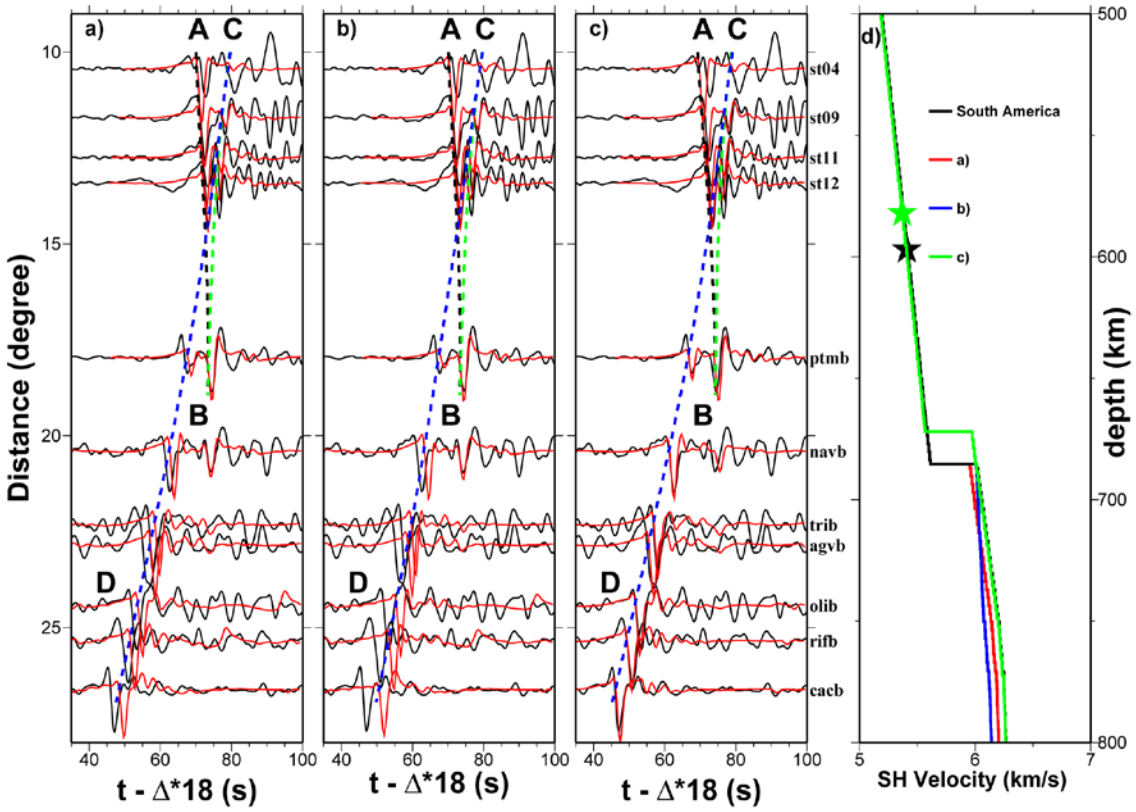

Figure 19. Comparisons of observed tangential displacements for event 1 (black traces) and synthetic waveforms (red traces) calculated using models perturbed from our best fitting model: (a) with a smaller velocity jump across the discontinuity, (b) with a smaller SH velocity gradient below the discontinuity, and (c) with a 15-km shallower discontinuity, along with predicted travel time curves of the three branches of the seismic phases (dashed lines). Models are shown in (d) and labeled accordingly with the synthetics panels. Synthetics in (c) are calculated with an event depth 15 km shallower. Stars in (d) represent source depths used in the calculations. Same station corrections are made as in Figure 18.

The depth of the 660-km discontinuity is, however, not well constrained by the seismic data. It trades off the assumed event depth, and thus strongly depends on the accuracy of the event depth determination. For example, synthetic waveforms calculated

using a model with a 15-km shallower 660-km discontinuity and a 15-km shallower event depth are indistinguishable from those predicted by our preferred model (Figure 19c). The determination of the absolute depth of the 660-km discontinuity would require accurate determination of event depth from other means.

4.5 Seismic shear velocity structure beneath northeast Asia

Tangential displacements recorded in the NCDSN for events 2 and 3 constitute a good record section sampling the seismic structure near the 660-km discontinuity beneath northeast Asia (black traces, Figures 20 for event 2 and 21 for event 3). Three branches of triplication are clearly identifiable in the distance range of $10^o - 35^0$. The AB branch turns about 480 km deep in the transition zone at an epicentral distance of 10^0 and starts to diffract at the top of the 660-km discontinuity at an epicentral distance of about 30^0. For event 2, the AB branch can be clearly observed at stations HNS, TIY, HEF, WZH, WHN, NNC, CNS, GTA, and becomes indiscernible at stations GZH, CD2, GUL, SZN at distances greater than 30^0 (Figure 20). The CD phase crosses over the AB phase at about 19^o (Figure 20) and samples the top of the lower mantle to a depth of about 910 km at 35^o. For event 3, the AB branch can be clearly observed at stations WHN, BJT, CNS, LYN, GUL, XSA, OIZ, GYA and becomes indiscernible at stations GZH, CD2, GUL, SZN at distances larger than 30^0 in the data (Figure 20). The CD phase crosses over the AB phase at about 19.5^o (Figure 21) and samples the top of the lower mantle to a depth of about 910 km at 35^o.

PREM also cannot explain the seismic data for events 2 (Figure 20a) and 3 (Figure 21a). For both events, the predicted travel time difference between the AB and CD branches is larger and the crossover of the CD branch occurs at an earlier distance in the PREM synthetics than in the data. A deeper 660-km discontinuity with a larger velocity jump across the discontinuity is needed to explain the observed travel time features and the crossover distance in the seismic data for both events.

We obtained our best-fitting model by searching models with various velocity jumps across the discontinuity and various depths of the discontinuity. The best-fitting model has PREM velocity gradients in the transition zone, a velocity jump of 0.53 km/s across the discontinuity, a large PREM-like velocity gradient extending 80 km below the 660-km discontinuity and a deeper discontinuity at 730 km (Figures 20c and 21c). Synthetics calculated based on our best-fitting model fit the observed travel time differences between the AB and BC branches, cross-over distance, and move out of the CD phase, and overall waveforms well (Figures 20b and 21b).

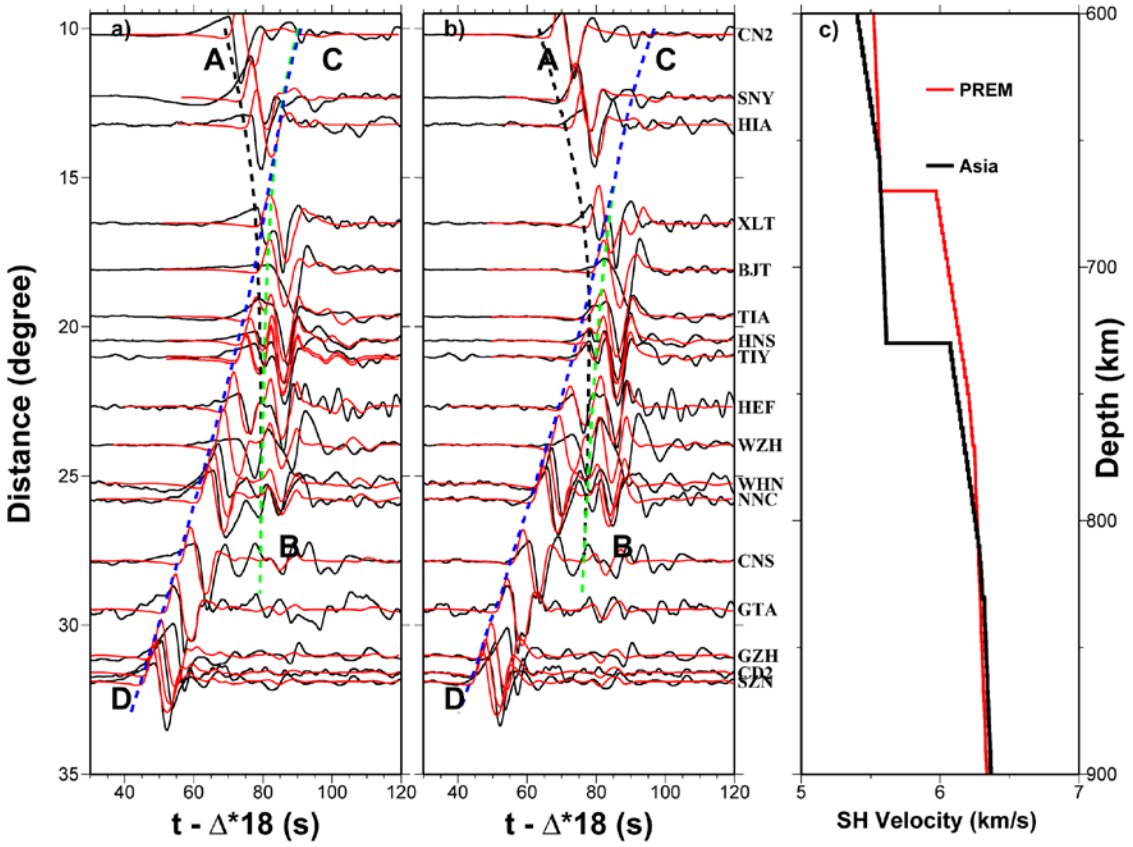

Figure 20. Comparisons of observed tangential displacements for event 2 (black traces) and synthetic waveforms (red traces) calculated using (a) PREM and (b) our best fitting Asia model, along with predicted travel time curves of the three branches of the seismic phases (dashed lines). Models are shown in (c). Station travel time corrections are made for following stations: CN2 (2 s), SNY (2 s), TIA (2 s), HNS (2 s), TIY (2 s), GTA (2.5 s), based on the observations from another event.

The velocity jump across the discontinuity of our best-fitting model is larger than that of PREM and it is well constrained by the travel time difference between the AB and CD branches in the seismic data for both events. The velocity jump across the discontinuity is tightly constrained by the observed travel time difference between the AB and CD branches. A larger (smaller) velocity jump would predict a larger (smaller) time separation between the two phases. We show an example for a model with a larger velocity jump across the 660-km discontinuity in Figures 22a and 23a. Note that the

synthetics show a larger travel time difference between the AB and CD branches than in the data (Figures 22a and 23a).

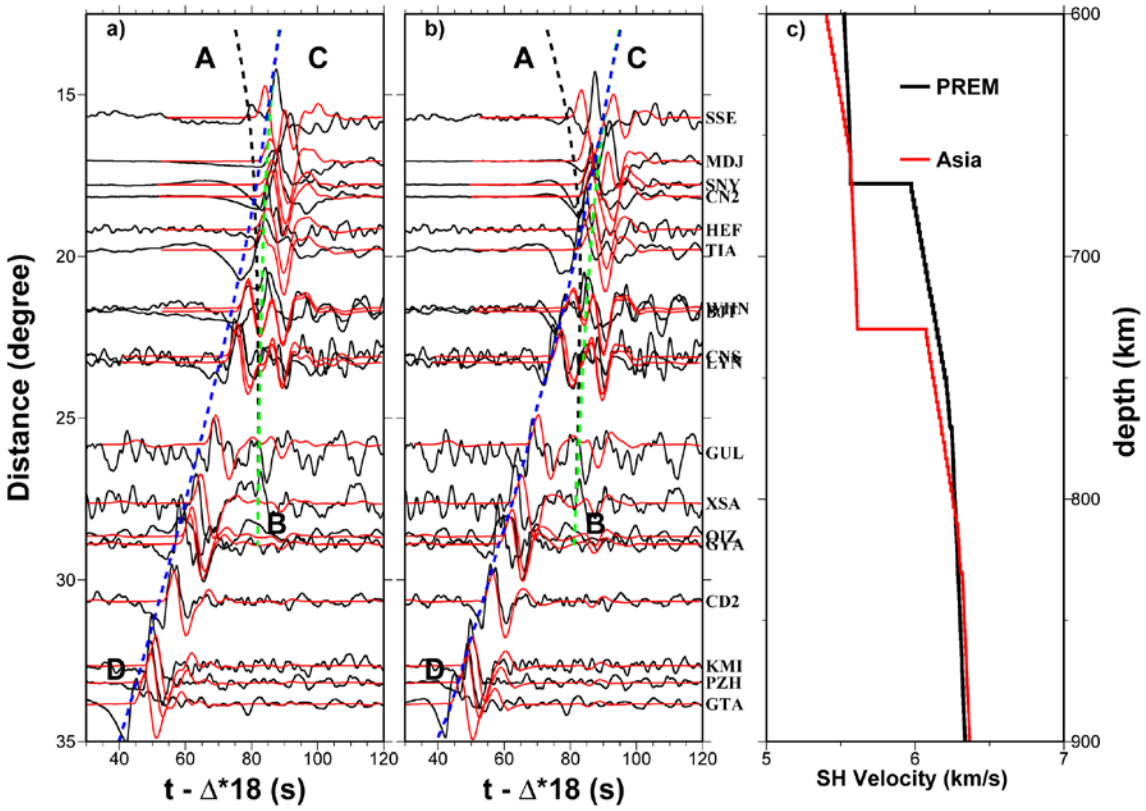

Figure 21. Comparisons of observed tangential displacements for event 3 sampling northeast Asia (Figure 6) (black traces) and synthetic waveforms (red traces) calculated using (a) PREM and (b) our best fitting Asia model, along with predicted travel time curves of the three branches of the seismic phases (dashed lines). Models are shown in (c). Station travel time corrections are made for following stations: CN2 (2 s), SNY (2 s), GYA (-1.5 s), KMI (3 s), PZH (0.5 s), based on the observations from another event.

The PREM-like velocity gradient below the 660-km discontinuity in our best-fitting model is also well resolved by the seismic data. The observed move-out of the CD phase is sensitive to the velocity gradient below the discontinuity. For example, synthetics calculated based on a model with a larger velocity gradient below the 660-km

discontinuity show a different move-out of the CD branch from that in the data (Figures 22b and 23b).

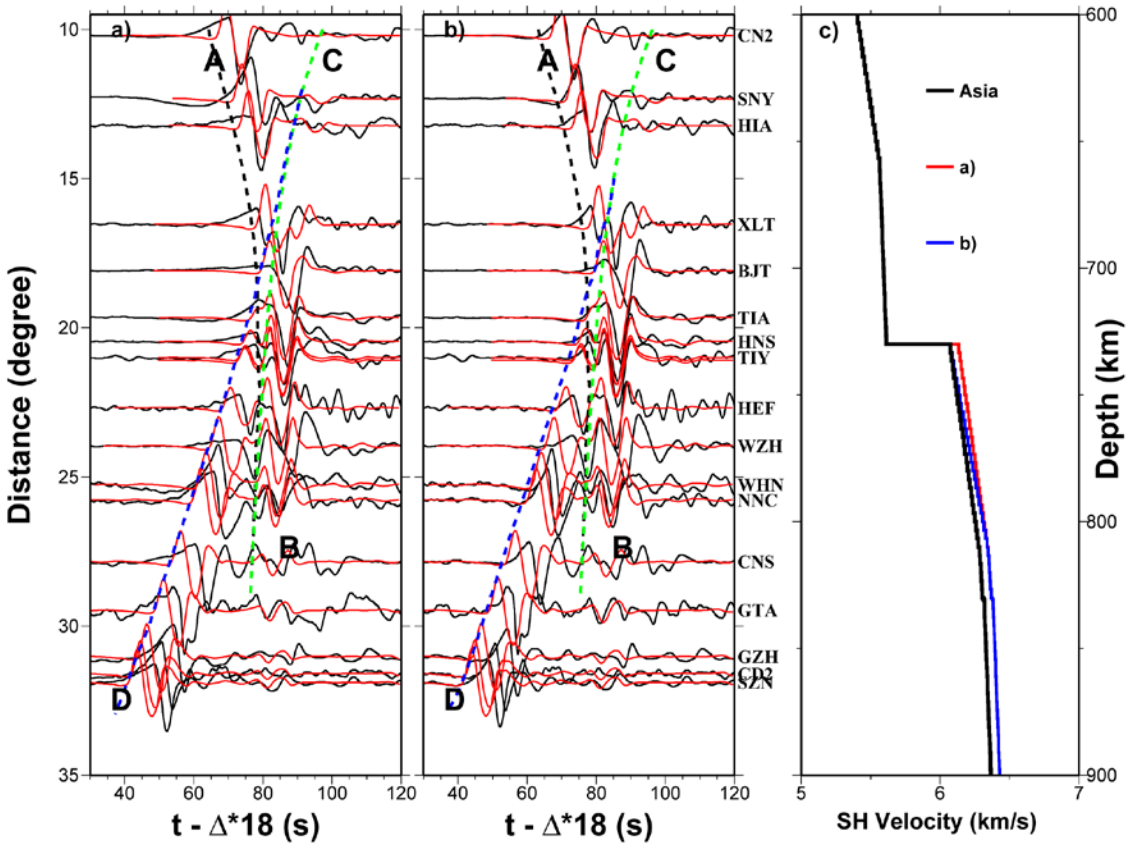

Figure 22. Comparisons of tangential displacements observed for event 2 (black traces) and synthetic waveforms (red traces) calculated using two models perturbed from the best fitting Asia model: (a) with a larger velocity jump across the 660-km discontinuity, and (b) with a larger velocity gradient below the discontinuity, along with predicted travel time curves of the three branches of the seismic phases (dashed lines). Models are shown in (c) and labeled accordingly with the synthetics panels. Station corrections are made as in Figure 20.

The depth extent of the large velocity gradient below the 660-km discontinuity is also well constrained by the seismic data. A shallower depth extent of the large velocity gradient below the 660-km discontinuity predicts later CD phases in the synthetics at

large distances than in the data (Figures 24a and 25a), while a deeper depth extent predict earlier CD phases in the synthetics at large distances (Figures 24b and 25b).

The best-fitting PREM-like velocity gradient just above the 660-km discontinuity is well constrained by the termination distance of the AB branch in the seismic data. The larger the velocity gradient above the discontinuity, the smaller the termination distance of the AB branch. We show an example of comparison of the data and synthetics for a model with a larger velocity gradient just above the discontinuity (Figures 26b and 27b). Note that, for a larger velocity gradient above the discontinuity, the synthetics show an indiscernible AB phase at large distances ($> 27^o$) and a weak AB phase at about 26^o, while the data exhibit a strong AB phase up to 33^o (Figures 26b and 27b).

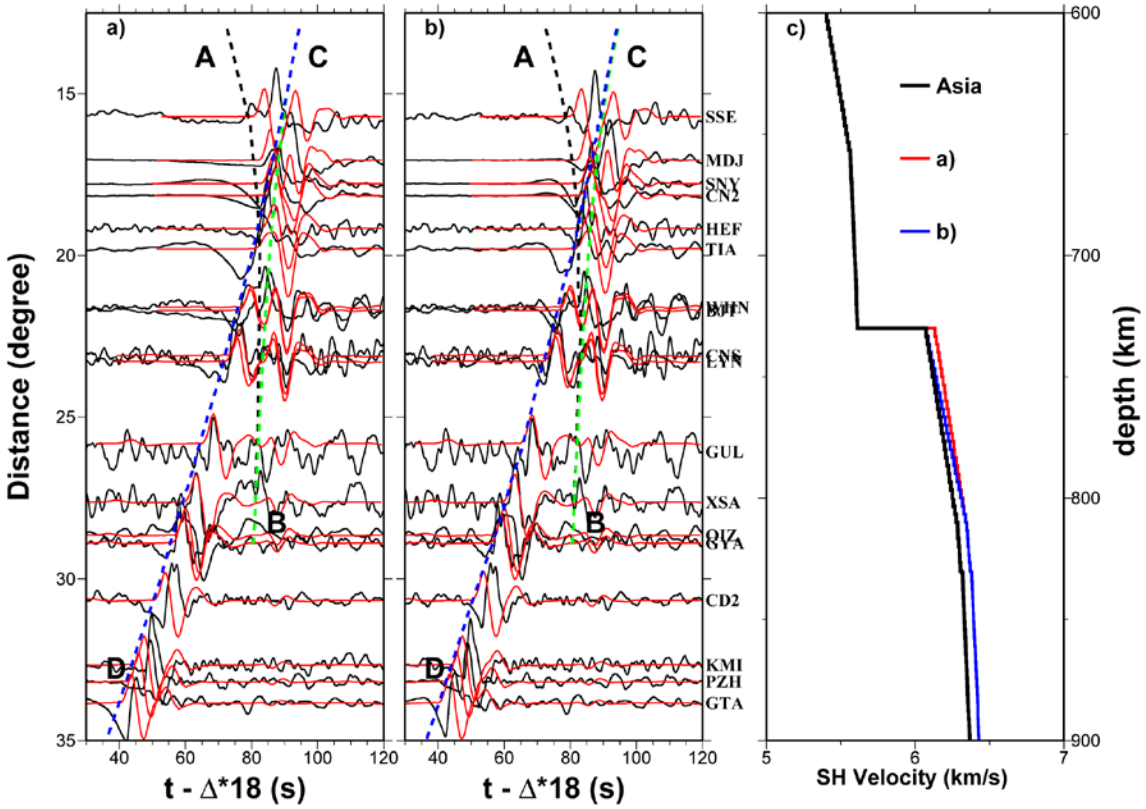

Figure 23. Comparisons of tangential displacements observed for event 3 (black traces) and synthetic waveforms (red traces) calculated using three models perturbed from the best fitting Asia model: (a) with a larger velocity jump across the 660-km discontinuity, and (b) with a larger velocity gradient below the discontinuity, along with predicted travel time curves of the three branches of the seismic phases (dashed lines). Models are shown in (c) and labeled accordingly with the synthetics panels. Station corrections are made as in Figure 21.

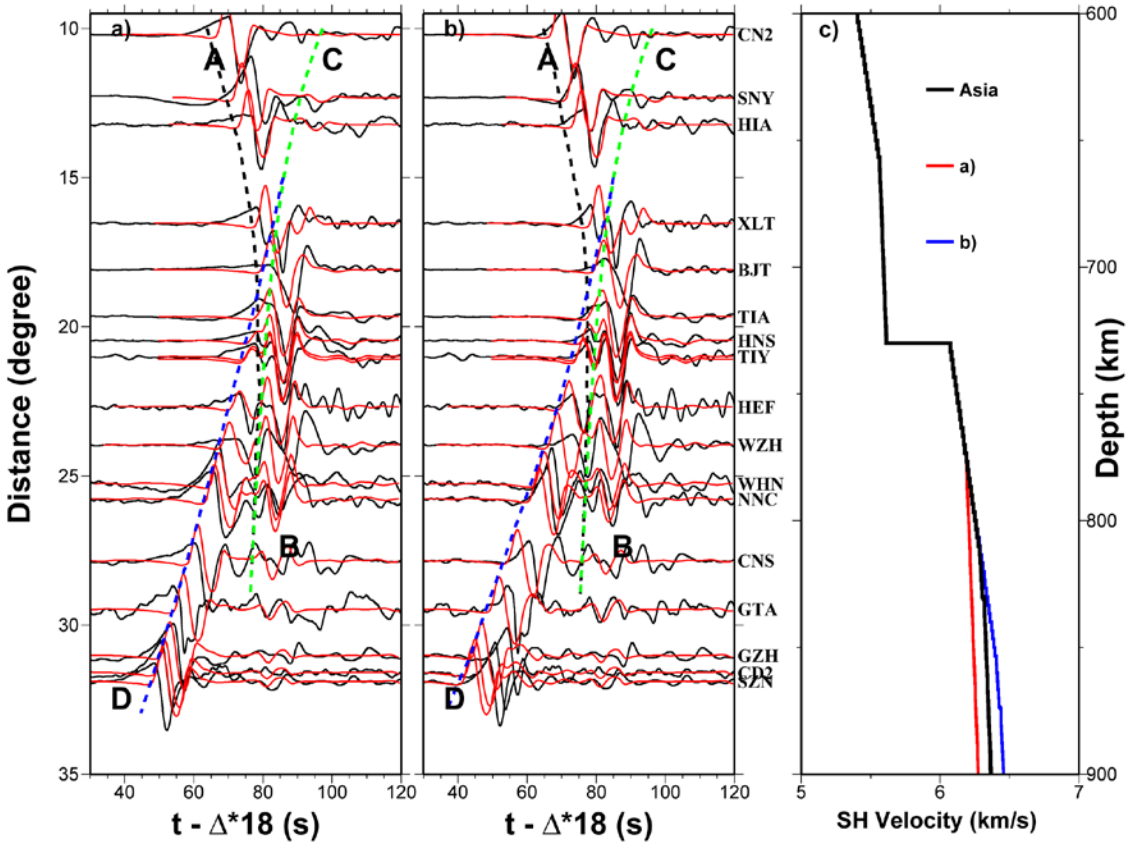

Figure 24. Comparisons of tangential displacements observed for event 2 (black traces) and synthetic waveforms (red traces) calculated using two models perturbed from the best fitting Asia model: (a) with a smaller depth extent of the larger velocity gradient below the 660-km discontinuity and (b) with a larger depth extent of the larger velocity gradient below the 660-km discontinuity, along with predicted travel time curves of the three branches of the seismic phases (dashed lines). Models are shown in (c) and labeled accordingly with the synthetics panels. Station corrections are made as in Figure 20.

The seismic data sampling northeast Asia also require a change of velocity gradient about 70 km above the 660-km discontinuity, same as PREM. PREM has two velocity gradients in the transition zone, with one (0.0029 (km/s)/km) between 400 km and 600 km depths and the other (0.0007 (km/s)/km) between 600 km and 670 km. Note that, while a smaller velocity gradient would explain the termination distance of the AB branch in the seismic data, it would also predict a strong phase traveling in shallow

portion of the transition zone (pointed by arrows in Figures 26a and 27a). No such phase is visible in the data. When the velocity gradient in the lowermost transition zone is fixed, changing the velocity gradient in the upper transition zone does not affect the termination distance of the AB branch. It would however generate different amplitudes and travel times for the phase traveling in the upper transition zone. A larger velocity gradient would predict a weak phase traveling in the shallow part of the transition zone, but it would make the AB branch terminated at closer distances than in the data. In another word, the termination distance of the AB branch observed in the data requires a small velocity gradient in the lower part of the transition zone, whereas the fact the phase traveling in the upper part of the transition zone is invisible in the data requires a large velocity gradient in the upper part of the transition zone. The seismic data thus indicate different velocity gradients in the lower (lowermost 70 km) and upper parts of the transition zone.

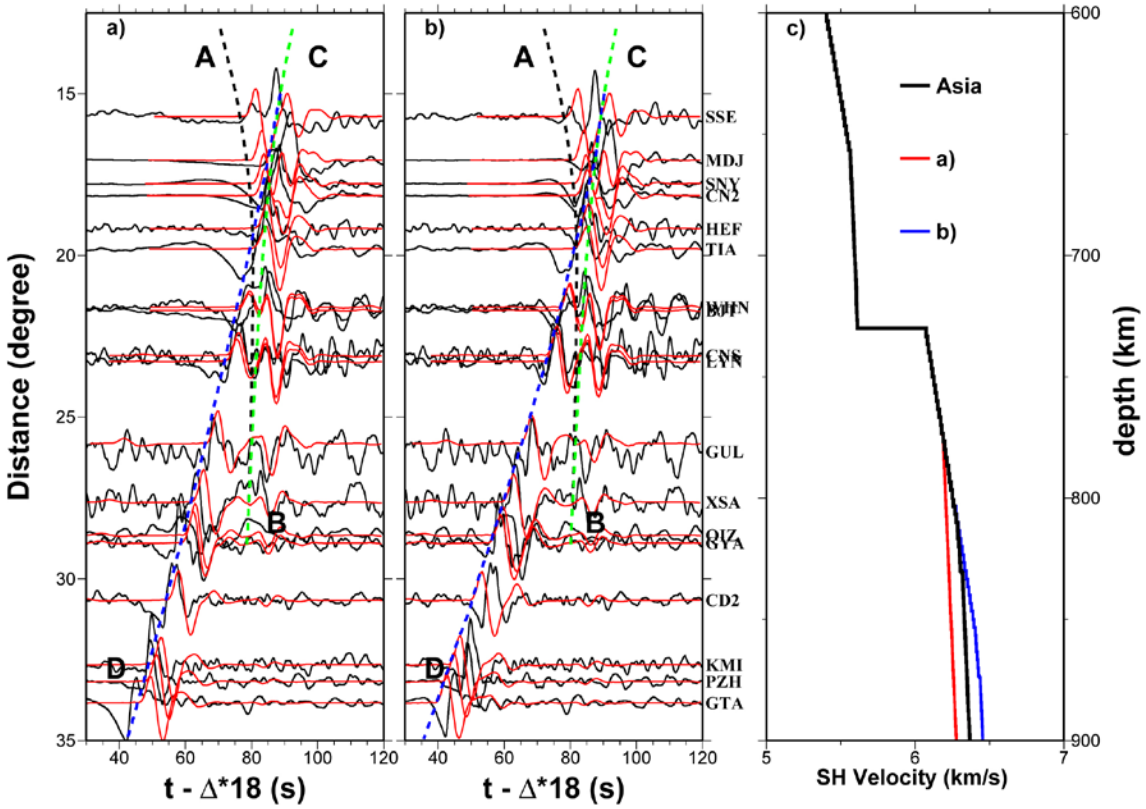

Figure 25. Comparisons of tangential displacements observed for event 3 (black traces) and synthetic waveforms (red traces) calculated using two models perturbed from the best fitting Asia model: (a) with a smaller depth extent of the larger velocity gradient below the 660-km discontinuity and (b) with a larger depth extent of the larger velocity gradient below the 660-km discontinuity, along with predicted travel time curves of the three branches of the seismic phases (dashed lines). Models are shown in (c) and labeled accordingly with the synthetics panels. Station corrections are made as in Figure 21.

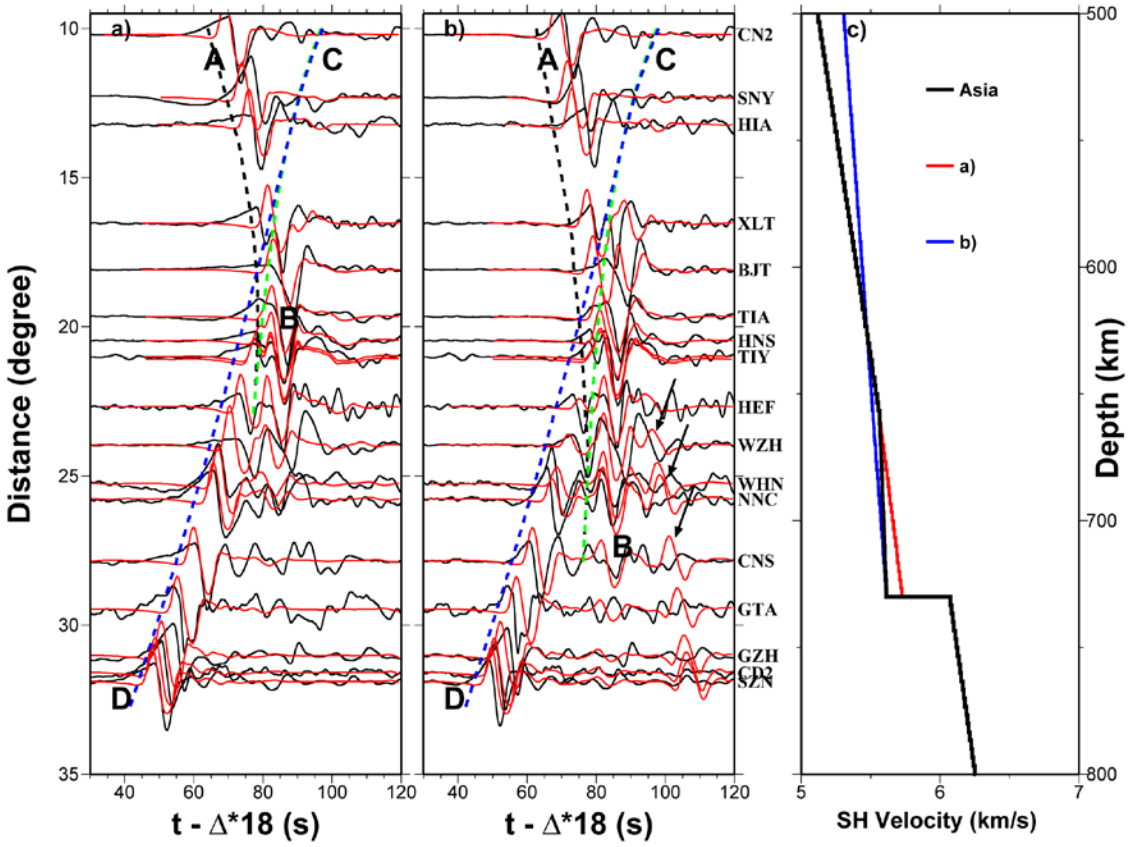

Figure 26. Comparisons of tangential displacements observed for event 2 (black traces) and synthetic waveforms (red traces) calculated using two models perturbed from the best fitting Asia model: (a) with a uniform velocity gradient in the transition zone, and (b) with a different velocity gradient in the bottom 70 km of the transition zone, along with predicted travel time curves of the three branches of the seismic phases (dashed lines). Models are shown in (c) and labeled accordingly with the synthetics panels. Station corrections are made as in Figure 20.

The seismic data for events 2 and 3, although sample the transition zone beneath Northeast Asia in the directions perpendicular to each other, can be explained by a same SH velocity model (e.g., Figures 20b, 21b). The consistency of the results obtained from the two events indicates that the effect of lateral variation of seismic velocity is not significant in our sampling region and the one-dimensional waveform modeling is appropriate.

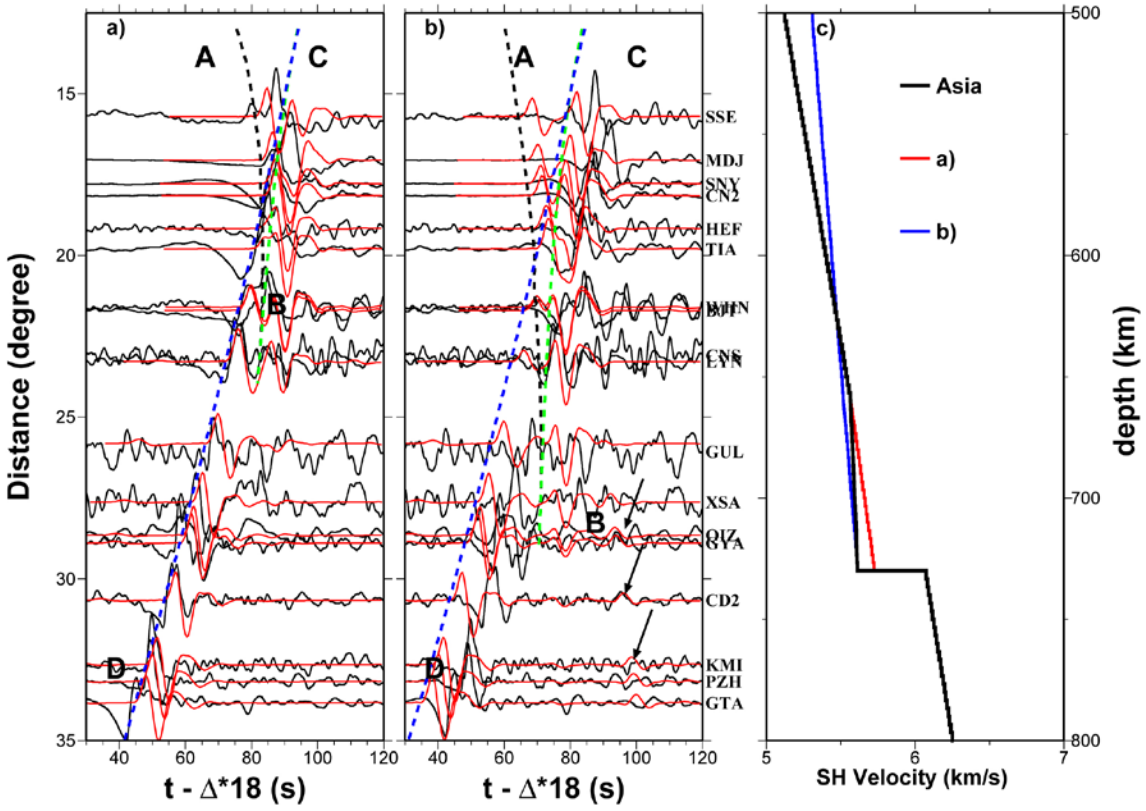

Figure 27. Comparisons of tangential displacements observed for event 3 (black traces) and synthetic waveforms (red traces) calculated using two models perturbed from the best fitting Asia model: (a) with a uniform velocity gradient in the transition zone, and (b) with a different velocity gradient in the bottom 70 km of the transition zone, along with predicted travel time curves of the three branches of the seismic phases (dashed lines). Models are shown in (c) and labeled accordingly with the synthetics panels. Station corrections are made as in Figure 21.

4.6 Compositional and mineralogical models beneath South America and northeast Asia

In this section, we infer mantle mineralogical models in the two regions through quantitative comparisons between the seismic models obtained from modeling the seismic data and the velocity structures predicted based on various mineralogical models. We also explore the conditions of mantle composition and temperature that are appropriate for explaining the difference of the inferred mineralogical models between

the two regions. In mineral physics modeling, seismic velocities near the 660-km discontinuity are calculated following the procedures outlined in Chapter 2.

The velocity gradient above the 660-km discontinuity is controlled by temperature and pressure dependences of the elastic properties of major mineral phases (ringwoodite + garnet + Ca-perovskite) and, if ilmenite is present, the increasing volume fraction of ilmenite with depth. The velocity jump across the 660-km discontinuity is sensitive to the volume fraction of ringwoodite in the composition and the fraction of garnet transformed to perovskite across the discontinuity. The velocity gradient below the discontinuity is determined by temperature and pressure dependences of the elastic properties of major mineral phases (perovskite + magnesiowustite + Ca-perovskite +garnet) and the decreasing volume fraction of garnet (or increasing volume fraction of perovskite) with depth. The decreasing volume fraction of garnet would generate a large velocity gradient in the top of the lower mantle. The depth extent of the high velocity gradient below the 660-km discontinuity is sensitive to the volume fraction of garnet present after its first-order transformation at the 660-km discontinuity, which is sensitive to the aluminum content of mantle composition (Table 3), but less so to mantle temperature.

Table 3. Garnet below the 660-km discontinuity v.s. aluminum content

Aluminum content (%)	Depth extent of garnet below the discontinuity (km)
0	No garnet
1	No garnet
2	No garnet
3	70
4	>100

For PREM, the velocity gradient above the 660 km discontinuity can be explained by the temperature and pressure dependences of the elastic properties of the major phases (ringwoodite + garnet + Ca-perovskite) (Figure 28a). The velocity jump can be explained by the pyrolite model (37.8% garnet and 54% ringwoodite). The velocity gradient below the 660-km discontinuity of PREM can be explained by the temperature and pressure dependences of the elastic properties of major mineral phases (perovskite + magnesiowustite + Ca-perovskite + garnet) and the decreasing volume fraction of garnet with depth in a mantle composition with an aluminum content of 3.4%.

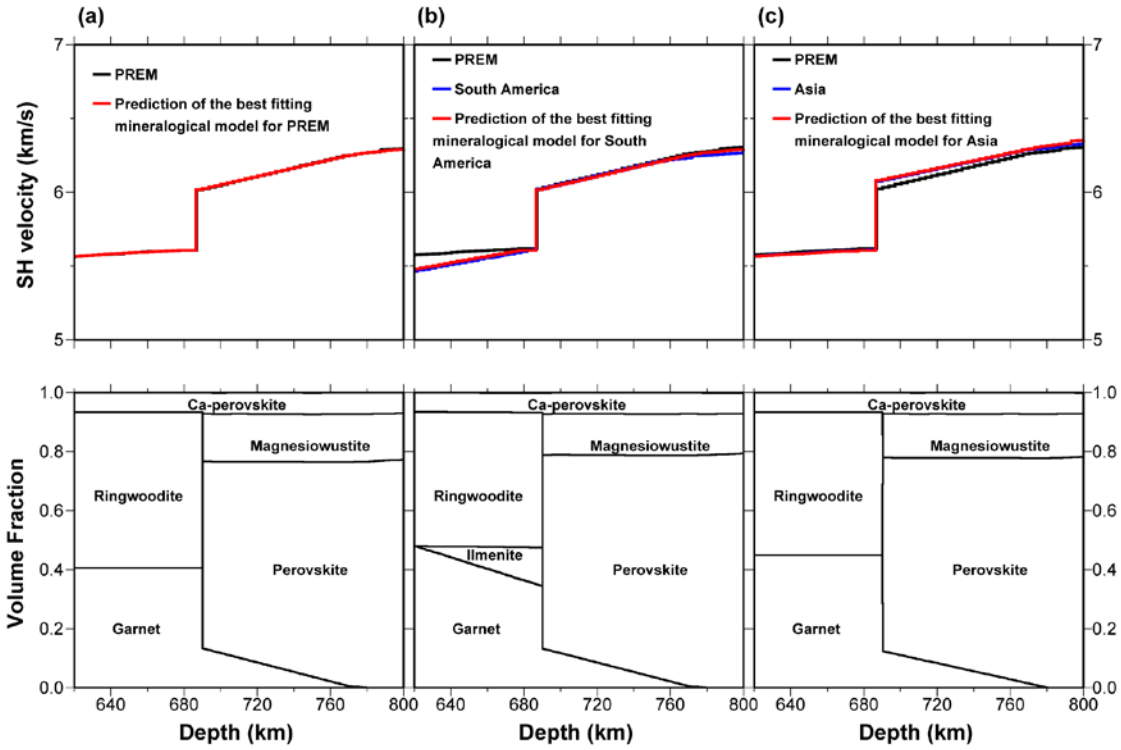

Figure 28. (Top) Comparisons between (a) PREM, (b) best fitting model for South America and (c) best fitting model for northeast Asia, and predicted velocity structures based on three mineralogical models shown in the bottom. Velocity models are calculated on the basis of measured elastic properties, relative volume fractions of these phases, and an adiabatic temperature gradient of 0.7 ${}^{0}C$/km. PREM is plotted as reference. (Bottom) Volume fractions of major mineral phases as a function of depth in three mineralogical models. The phase transformations from ringwoodite to perovskite plus magnesiowustite and from garnet to perovskite are assumed to occur in a same depth in the calculation.

Beneath South America, the temperature and pressure dependences of the elastic properties of the major phases cannot explain the large velocity gradient above the 660-km discontinuity, and existence of ilmenite is needed to explain the gradient (Figure 28b). Because the shear wave velocity of ilmenite is larger than that of garnet, increasing volume fraction of ilmenite results in a large velocity gradient above the 660-km discontinuity. In order to maintain the velocity jump across the discontinuity and the depth extents of the high velocity gradient below this discontinuity to be similar to PREM, a larger volume fraction of garnet in bulk composition model is needed beneath South America. The depth extent of the high velocity gradient below the 660-km discontinuity (about 80 km, Figure 28b) indicates a mantle composition with an aluminum content of 3.4% in the top of the lower mantle.

Beneath northeast Asia, the velocity gradient above the 660-km discontinuity can be explained by the temperature and pressure dependences of elastic properties of the major phases in the transition zone (ringwoodite + garnet + Ca-perovskite) (Figure 28c). The large velocity jump across the 660-km discontinuity requires more garnet changing to perovskite across the discontinuity. The inferred depth extent of the high velocity gradient below the 660-km discontinuity (about 80 km) would indicate a mantle composition with an aluminum content of 3.4% in the top of the lower mantle in this region.

Our mineral physics modeling indicates that our seismic results can be explained by a uniform composition with aluminum content of 3.4% in the lower mantle between the two regions. If we assume that the mantle have a uniform composition in these two regions, our inferred seismic structures would indicate different temperatures in the

transition zone between the two regions. For a mantle composition with an aluminum content of 3.4%, the existence of ilmenite beneath South America would suggest a mantle temperature (at 660 km) lower than $1334\,^{0}C$ and the absence of ilmenite beneath northeast Asia would require a mantle temperature higher than $1434\,^{0}C$ (Table 4). That means a mantle temperature difference of at least $100\,^{0}C$ between two regions. The absolute mantle temperature trades off with the Al content and subjects to the uncertainty in mineral physics calculation, but the temperature difference does not.

As the other end member of the explanations, the seismic structures above the 660-discontinuity between the two regions can also be explained by different mantle compositions with different aluminum contents without invoking a temperature difference between the two regions. In this case, the aluminum content of the mantle composition should be lower beneath South America because of the presence of ilmenite there. If, for example, we assume mantle temperature (at 660 km) in these two regions is $1334\,^{0}C$, the aluminum content in mantle composition is about 3.4% beneath South America to explain the presence of ilmenite there and should be higher than 4.6% beneath northeast Asia to explain the absence of ilmenite there. An aluminum content difference of more than 1% is required between the two regions. The inferred absolute aluminum content depends on the assumed mantle temperature, but the inferred difference in aluminum content between the two regions does not.

Table 4 Presence of Ilmenite above the 660-km discontinuity v.s. aluminum content and mantle temperature

Aluminum content (%)	The temperature of the presence of ilmenite (^0C)
0	Any temperature.
1	<1694
2	<1534
3	<1434
4	<1374
5	<1334

4.7 Double 660-km discontinuities

In the previous sections, we have assumed a single discontinuity at the bottom of the transition zone in both the seismic and mineral physics modeling. Since two phase transformations occur near 660 km and they can occur at different pressures, multiple discontinuities may exist near the 660-km depth. The depths of the phase transformations are controlled by mantle temperature, composition and chemical interaction between the olivine and pyroxene components. The phase transformation from ringwoodite to perovskite and magnesiowustite is endothermic with a negative Clapeyron slope, while that from garnet to perovskite is exothermic with a positive Clapeyron slope. When mantle temperature is high, the phase transformation from ringwoodite to perovskite and magnesiowustite occurs at a lower pressure and the phase transformation from garnet to perovskite occurs at a higher pressure, and vise versa. So if these transformations do not

interact chemically, they will most likely occur at different pressures and double discontinuities would appear near the 660-km depth. The phase transformation from garnet to perovskite, however, is also sensitive to the Al content in the system. A high Al content would stabilize the garnet phase to larger pressures, and make the garnet phase transformation to perovskite to appear at larger depths. The Al partitions are different between different mineral assemblages. Al would preferentially be partitioned into garnet when garnet, ringwoodite and ilmenite are in coexistent, and would preferentially be partitioned into perovskite in the assemblage of ringwoodite and perovskite. When the phase transformation from ringwoodite to perovskite and magnesiowustite occurs and at a pressure lower than the phase transformation from garnet to perovskite, some Al would be partitioned into perovskite from garnet. A reduced Al content in garnet would make the phase unstable, and the phase transformation from garnet to perovskite would occur instantaneously at the same pressure (Figure 29a). In this case, a single discontinuity would appear near the 660-km depth. If, for the mantle temperature and composition that the phase transformation from garnet (and ilmenite, if present) to perovskite occurs at a pressure lower that the ringwoodite transformation to perovskite plus magnesiowusite, double discontinuities would appear near the 660-km depth, with the shallower one resulted from garnet (and ilmenite, if present) to perovskite and the deeper one from the transformation from ringwoodite to perovskite plus magnesiowusite and, in a system with a high Al content, a further transformation from garnet to perovskite (Figures 29b, 29c). Such scenarios could occur when the mantle temperatures are relatively low or/and the Al contents of the system are low. At a high Al content and in the absence of ilmenite, the shallower discontinuity is controlled by the first-order transformation from garnet to

perovskite. The deeper discontinuity is controlled by the phase transformation from ringwoodite to perovskite plus magnesiowustite and a further transformation from garnet to perovskite in response to the reduced Al content in garnet because of the increased volume of perovskite after the ringwoodite transformation (Figure 29b). When ilmenite is present, Al would preferentially be partitioned into garnet and the presence of the ilmenite phase would increase the Al content in garnet and stabilize the garnet phase. However, when ilmenite transforms to perovskite, Al would be preferentially partitioned into perovskite from garnet and a reduced Al content in garnet would make garnet unstable and to transform to perovskite. In this scenario, the shallower discontinuity is controlled by simultaneous transformations of garnet and ilmenite to perovskite and the deeper discontinuity by the phase transformation from ringwoodite to perovskite plus magnesiowustite (Figure 29c).

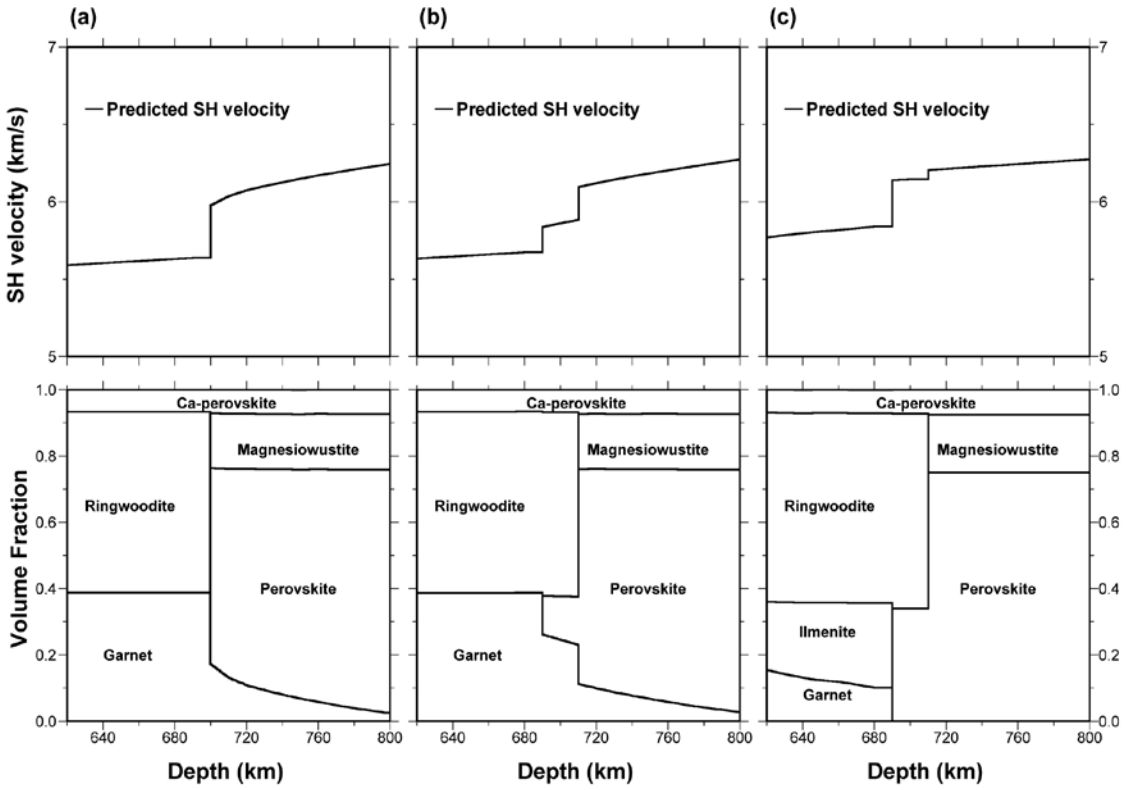

Figure 29. (Bottom) volume fractions of major mineral phases as a function of depth for three mantle thermal and compositional models: (a) with a mantle temperature of 1554 ^0C and an Al content of 4%; (b) with a mantle temperature of 1394 ^0C and an Al content of 4%; and (c) with a mantle temperature of 1394 ^0C and an Al content of 1%. (Top) SH velocity models predicted based on three mantle thermal and compositional models shown in the bottom panels.

The depth separation of the double discontinuities is sensitive to mantle temperature and the Al content of the system. A lower mantle temperature would make the phase transformation from ringwoodite to perovskite plus magnesiowustite to occur at a higher pressure and the phase transformation from garnet to perovskite at a lower pressure, so the separation of the discontinuities increases with decreasing temperature. A lower Al content would not change the pressure of the ringwoodite phase transformation, but it would make the phase transformation from garnet to perovskite to occur at a lower pressure, so the separation of the discontinuities increases with decreasing Al content.

However, when the Al content and/or mantle temperature are lowered to some extents, the ilmenite phase starts to appear (such as in the scenario in Figure 29c). The separation of the double discontinuities is then controlled by the pressure difference of the phase transformations from ilmenite to perovskite and from ringwoodite to perovskite plus magnesiowustite, and reaches maximum. The maximum separation of the double discontinuities also becomes insensitive to the Al content and mantle temperature, because these two phase transformation pressures are not sensitive to the Al content, and both phase transformations are endothermic with similar Clapeyron slopes making the pressure difference of these two phase transformations insensitive to temperature.

The velocity jumps of the double discontinuities are different in the two scenarios shown in Figures 29b and 29c. The S velocity jump caused by phase transformation from garnet to perovskite is large (about 8-9%), while that caused by the phase transformation from ringwoodite to perovskite and magnesiowustite is only about 1%. In the absence of the ilmenite phase (Figure 29b), the velocity jump across the shallower discontinuity is about 2.8% and that across the deeper one is about 3.5%. In the presence of ilmenite (Figure 29c), the velocity jump across the shallower discontinuity is dominant (about 5%) and that of the deep one is about 1%.

Under the inferred mantle temperatures and compositions beneath South America and northeast Asia, the separation between the double discontinuities should be less than 20 km. Beneath South America, with the ilmenite phase present, double discontinuities may exist, similar to the scenario in Figure 29c. The separation between the two discontinuities is controlled by the pressure difference of the phase transformations from ilmenite to perovskite and from ringwoodite to perovskite plus magnesiowusite, and is

less than 20 km. Beneath northeast Asia, there is no evidence for the presence of the ilmenite phase. There are two possibilities: 1. the mantle temperature is high, so that the ringwoodite to perovskite and magnesiowustite phase transformation occurs at a lower pressure and the phase transformation from garnet to perovskite occurs at the same depth, similar to the scenario in Figure 29a; or 2. the Al content is high, double discontinuities exisit, with the shallower one caused by the garnet to perovskite phase transformation, and the deeper one by the ringwoodite transformation to perovskite plus magnesiowustite and a further transformation from garnet to perovskite similar to the scenario in Figure 29b. The separation between the two discontinuities in this case is also within 20 km.

The SH data we used cannot distinguish double discontinuities separated by less than 20 km from a single discontinuity. The synthetics based on a model with two discontinuities separated by 20 km fit the seismic data equally well (Figure 30a). Our seismic data, however, would exclude models with double discontinuities separated by 40 km, as double peaks can be observed in the synthetics, different from the seismic data (Figure 30b). Thus, the seismic data support the above inference of the properties of phase transformations near the 660-km depth.

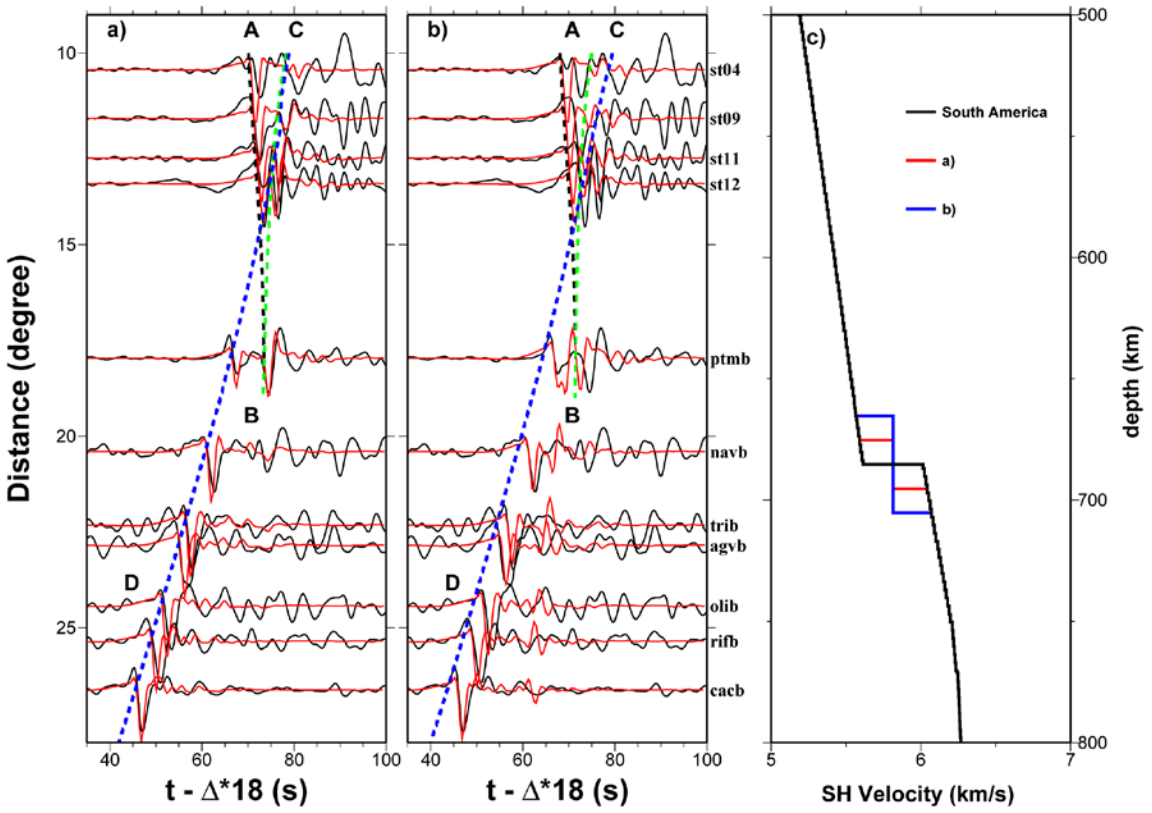

Figure 30. Comparisons of observed tangential displacements for event 1 (black traces) and synthetic waveforms (red traces) calculated using models perturbed from the best fitting model with double discontinuities near the 600-km depth with depth separations of (a) 20 km and (b) 40 km. Models are shown in (c) and labeled accordingly with the synthetics panels.

4.8 Comparison to other studies

Compared to the studies of the 660-km discontinuity using other approaches, such as precursors to the PP and SS phases (e.g., *Shearer, 1991; Shearer and Flanagan, 1999)* or receiver functions *(e.g. Niu and Kawakatsu, 1996; Shen et al., 1996,*), our study can constrain the velocity gradients above and below the discontinuity, in additional to the velocity jump across the discontinuity and the depth of the discontinuity. The velocity gradient above the 660-km discontinuity is sensitive to mantle temperature and the Al content, and the velocity gradient below the 660-km discontinuity is sensitive to the Al

content in the mantle. So these velocity gradients can place significant constraints on mantle temperature and composition. Our study is also affected little by the seismic heterogeneities in the shallower part of the mantle, while the precursor studies and receiver function analyses need to deal with the shallower heterogeneities carefully. Studies using the precursors to the PP and SS phases, however, provide global coverage of the properties of the 660-km discontinuity and the receiver function studies could provide a better lateral resolution in the study region. The inferred depth of the 660-km discontinuity in our study would also require an accurate determination of event depth.

4.9 Conclusions

We study seismic SH velocity structures, mineralogical models and mantle temperature and composition near the 660-km discontinuity beneath South America and northeast Asia, through joint modeling of seismic and mineral physics data. Our seismic data consist of the tangential component of triplicated phases recorded in the epicentral distance range of 10^{o}- 35^{o} for a deep event occurring in South America subduction zone and two events occurring in northeast Asia. The data suggest two different SH velocity structures near the 660-km discontinuity beneath South America and northeast Asia. Beneath South America, the velocity gradient above the 660-km discontinuity is larger than that of PREM; while the velocity jump across the discontinuity and the depth extent of the larger velocity gradient below the discontinuity are the same as those of PREM. Beneath northeast Asia, the velocity structures above and below the 660-km discontinuity are the same as that of PREM, while the velocity jump across the discontinuity is larger

than that of PREM. The 660-km discontinuity could be double discontinuities with a depth separation less than 20 km, but no more than 40 km.

We infer mantle mineralogical models in the two regions through quantitative comparisons between the seismic models obtained from modeling the seismic data and the velocity structures predicted based on various mineralogical models. The different velocity structures in these two regions can be explained by two different mineralogical models. The velocity gradient above the 660-km discontinuity beneath northeast Asia can be explained by temperature and pressure dependences of the elastic properties of the major phases (ringwoodite + garnet + Ca-perovskite), while the large velocity gradient above the discontinuity beneath South America requires presence of ilmenite. The depth extents of the large velocity gradient below the 660-km discontinuity in the two regions can be explained by the garnet transformation to perovskite persisting to large depths. The larger velocity jump across the discontinuity beneath northeast Asia indicates more garnet changing to perovskite across the discontinuity in the region than that in the pyrolite model.

The depth extent of the large velocity gradient below the 660-km discontinuity can be explained by a lower mantle composition with an aluminum content of 3.4% in the two regions. The different mineralogical models in the transition zone between the two regions can be explained by a difference in mantle temperature and/or composition, especially the aluminum content. Assuming a uniform mantle composition with aluminum of 3.4%, the presence of ilmenite above the 660-km discontinuity beneath South America and the absence of ilmenite beneath northeast Asia would suggest a mantle temperature difference of about 100^0C (with that beneath South America being

lower) between the two regions. Alternatively, the different mineralogical models above the 660-km discontinuity in these two regions can also be explained by a difference in aluminum content of 1% in mantle composition (with that beneath South America being lower) without invoking a temperature difference between the two regions.

Since at least two phase transformations occur near the 660-km depth and they can interact each other chemically, double discontinuities may exist at the bottom of the transition zone. We discuss the mantle temperature and composition that the double discontinuities may appear, as well as the depth separation and the velocity jumps of the double discontinuities. For the inferred mantle temperature and composition beneath South America and northeast Asia, the depth separation of double discontinuities is less than 20 km and cannot be resolved by the SH seismic data.

Chapter 5 Composition of Mars constrained using geophysical observations and mineral physics modeling

5.1 Abstract

We use the total mass, possible core radius and the observed moment of inertia factor to constrain the mineralogical and compositional structures of Mars. We adopt a liquid Fe-S system for the martian core and construct 1-D density models of the interior of Mars for a series of mantle compositions, core compositions and temperature profiles, and use the total mass of Mars to constrain its core radius. The moment of inertia factor of the planet is calculated and compared to the observation to place constraints on Mars composition. Based on other independent constraints of possible core radius of 1520-1840 km, and the moment of inertia factor (0.3662±0.0017) of Mars, we find that Fe content in the martian mantle is between 10.5% and 14.3%; Al content in the martian mantle is less than 4%; S content in the martian core is between 4.6% and 13.3%. Based on the possible composition models of Mars, the Fe content in Mars is between 25.61% and 31.52%, and the Fe/Si ratio in Mars is between 1.528 and 2.114, and the range is too broad to make a conclusion if Mars has the same nonvolatile bulk composition as that of C1 chondrite. We calculate the flattening factor and hydrostatic gravity of Mars using the second-order internal theory of equilibrium of a self-gravitating and rotating planet. We

also discuss the implications of these compositional and thermal models to the understanding of formation and evolution of the planet.

5.2 Introduction

Compositions of the mantle and the core of the terrestrial planets are important for us to understand the formation and evolution of the planets. The geophysics studies suggest that it is possible for the Earth to have the same bulk composition as that of C1 chondrite. Understanding the composition of Mars can help us understand planet's evolution. Previous studies (*Bertka and Fei, 1998*), using the moment of inertia factor and mineral physics data to constrain Mars composition, concluded that the bulk composition of Mars is different from that of C1 chondrite.

The studies assumed a solid core and a fixed mantle composition, and did not consider the uncertainties of the moment of inertia factor observation. Recent studies, however, have suggested a liquid core in Mars. Recent progress in mineral physics field allows us to quantitatively predict velocity and density profiles in the interior of Mars for various mantle compositions, core compositions and temperature profiles inside the planet. In this study, we adopt a liquid Fe-S system in the core and test a variety of mantle compositions. Our mineral physics modeling method allows us to systematically search for possible compositions in the mantle and the core. We construct 1-D density models of the interior of Mars for a series of mantle compositions, core compositions, and a temperature profile from *Fei and Bertka*'s (2005) study, and then calculate the moment of inertia factors. Comparing the predictions with the observations, we place constraints on the mantle and core compositions in Mars. We discuss methodology we

used in section 5.3; modeling results in section 5.4; and comparisons to previous study and other geophysical parameters in section 5.5.

5.3 Method

5.3.1 Moment of inertia factor

Moment of inertia, which describes the mass distribution inside a rotating body, is an important constraint on bulk composition of terrestrial planets. It is defined as $C = \int r^2 dm / MR^2$, the moment of inertia factor around the rotation axis; r is the distance to the rotation axis; M is the total mass; R is the mean radius of the planet. With the knowledge of a planet's total mass M, the mean radius R and the moment of inertia factor C, we can place constraints on density models inside the planet, which can be linked to the planet's composition using mineral physics modeling. Recent space mission, the Mars Pathfinder, provide us precise observations of the moment of inertia factor of Mars. *Folkner et al.* (1997) calculated the moment of inertia factor of Mars (0.3662 ± 0.0017), which can be used to place constraints on Mars composition, based on the measurements of the Mars Pathfinder lander.

5.3.2 Mineral physics modeling

In mineral physics modeling, density distribution in the martian mantle is calculated following the procedures outlined in chapter 2. *Wanke and Dreibus's* (1988) Mars' mantle composition model (Table 5) is used as a reference mantle composition, and the temperature model from *Fei and Bertka* (2005) is used as a reference temperature profile inside Mars.

Table 5 Reference mantle composition model of Mars (*Wanke and Dreibus, 1988*)

	MgO	**FeO**	**CaO**	SiO_2	Al_2O_3
Wt%	30.2	17.90	2.45	44.4	3.02
Mole%	40.72	13.54	2.37	40.16	3.21

Several recent studies (e.g. *Fei and Bertka, 2005*) suggest that the martian core is liquid. In this modeling, we adopt a liquid Fe-S system in the martian core, and use the elastic measurements for pure liquid Fe (*Anderson and Ahrens, 1994*) and for liquid Fe with 10% S (*Balog et al., 2003; Sanloup et al., 2000*) (Table 6) and an assumption of the elastic properties linearly changing with S content to predict core density profiles based on different S contents.

We predict the density profiles in the mantle and the core for a series of mantle composition and core composition, and constrain core radius using the total mass of Mars. For a fixed mantle composition, core composition and temperature profile, only one core radius could fit the total mass of Mars. Figure 31 shows a mineral assemblage (Figure 31b) and a density profile (Figure 31a) inside Mars predicted based on *Fei and Bertka*'s (2005) temperature model, *Wanke and Dreibus*'s (1988) Mars' mantle composition model and an liquid Fe-S system with 4% S in core. A martian crust with a depth of 50 km and a density of 3.0 g/cm^3 is adopted. Then we calculate the moment of inertia factor, and use possible core radius (1520—1840 km) (*Yoder et al., 2003*) and the observed moment of inertia factor (0.3662±0.0017) (*Folkner et al., 1997*) to place constraints on Mars composition models.

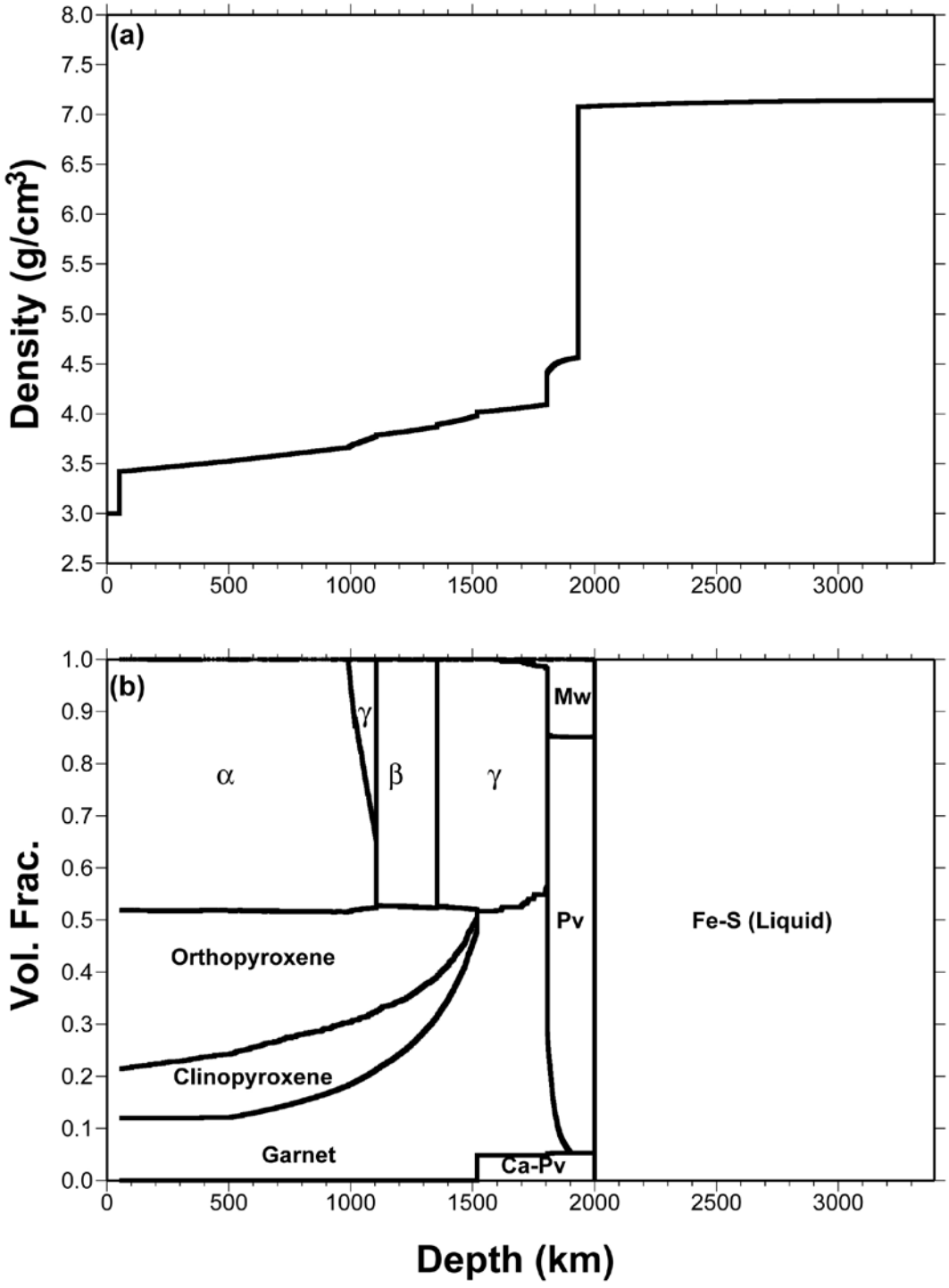

Figure 31. Predicted (a) density profile and (b) mineralogical model in Mars, based on *Fei and Bertka*'s (2005) temperature model, *Wanke and Dreibus*'s (1988) Mars' mantle composition model and a liquid Fe-S core with 4% S. A martian crust with a depth of 50 km and a density of 3.0 g/cm^3 is adopted. α denotes olivine; β wadsleyite; γ ringwoodite; Pv perovskite; Ca-Pv Cacium-perovskite; and Mw magnesiowustite.

Table 6 Elastic measurements of liquid Fe-S system

Material	$\rho_0 (g/cm^3)$	K(Gpa)	K'	$\alpha(K^{-1})$
Fe[1]	8.0	189	4.66	8.75×10^{-5}
$Fe+10\%S$[2]	6.4	122	4.7	8.75×10^{-5}

1: Anderson and Ahrens (1994)
2: Balog et al. (2003) and Sanloup et al. (2000)

5.4 Modeling results

Density in the martian core is controlled by S content in the martian core. A higher S content causes a lower density in the core, and requires a larger core radius to fit the total mass (Figure 33a). A fixed mantle density and a less dense and larger core result in a larger moment of inertia factor. A higher S content in the martian core results in a larger core radius (Figure 33a) and a larger moment of inertia factor of Mars (Figure 33b), when mantle composition is fixed.

Fe content in the mantle has significant effects on the mantle density and the moment of inertia factor of Mars. A higher Fe content causes a higher density in the mantle (Figure 32), because increasing Fe content would increase density of every mineral in the mantle. If the core density is fixed, increasing mantle density requires a decreasing core radius to fit the total mass of Mars (Figure 33a). A higher mantle density and a smaller core radius result in a higher moment of inertia factor. A higher Fe content in the martian mantle results in a smaller core radius (Figure 33a) and a higher moment of inertia factor (Figure 33b) of Mars, when the core composition is fixed. We search a series of composition models with different Fe contents in the mantle and S contents in the core (Figure 33). With the constraints of the total mass, possible core radius (1520—

1840 km) and the observed moment of inertia factor (0.3662±0.0017), we find that Fe content in the martian mantle is between 10.5%--14.3% (shadow region in Figure 33b), and S content in the martain core is between 4.6%--13.3% (shadow region in Figure 33b).

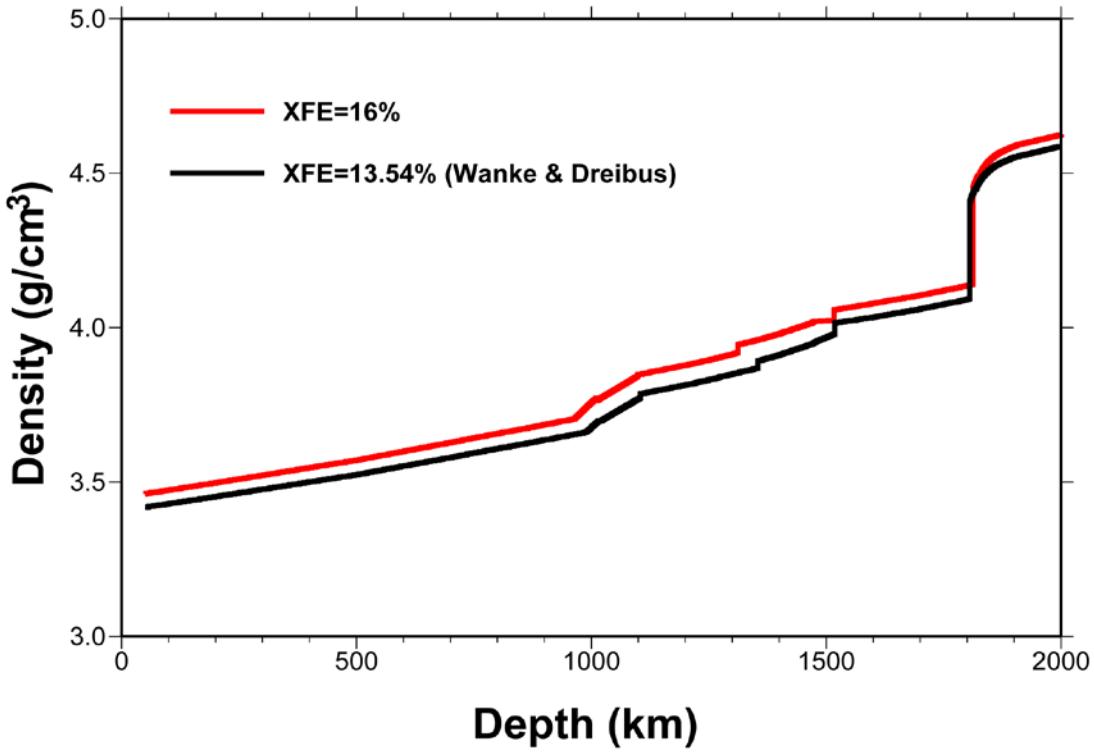

Figure 32. Predicted mantel density profiles inside Mars based on two compositional models with different Fe contents.

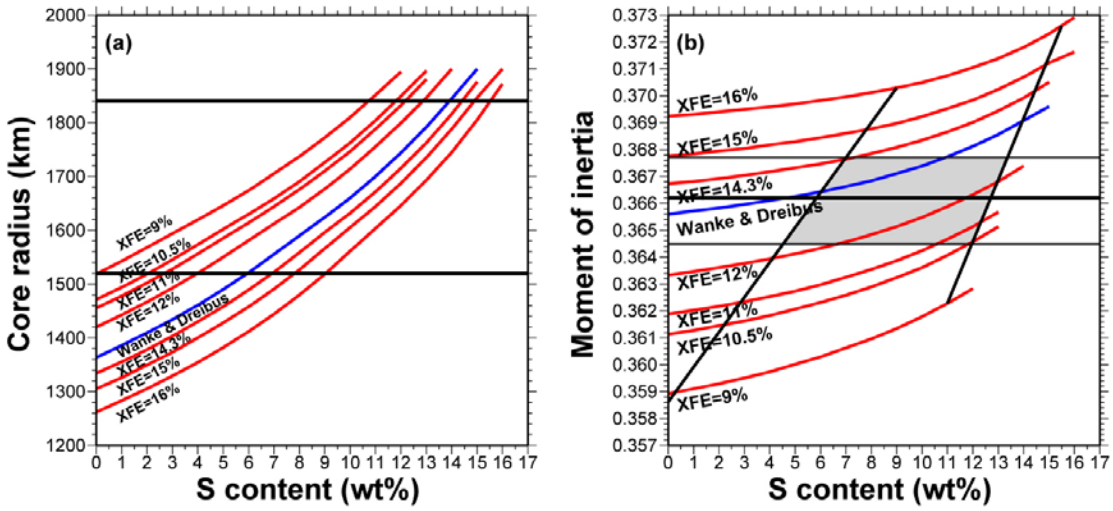

Figure 33. Predicted (a) core radius and (b) moment of inertia factors based on different Fe contents in the mantle and S contents in the core. The black horizontal lines in (a) and the black vertical lines in (b) are the boundaries of possible core radius range, 1520 km and 1840 km; the black horizontal lines in (b) are the observed value and error bars of the moment of inertia factor.

Al content does not affect the elastic properties of mantle minerals significantly, but it affects the stability of garnet, so it also affects the mantle density and the moment of inertia factor of Mars. A higher Al content would make garnet more stable, so there is more garnet and less pyroxene in the mantle. Garnet has a higher density than that of pyroxene, so increasing Al content in the mantle would increase the mantle density (Figure 34). If the core composition is fixed, an increasing Al content in the mantle requires a decreasing core radius (Figure 35a) and results in a higher moment of inertia factor (Figure 35b). We search a series of composition models with different Al contents in the mantle and S contents in the core (Figure 35). With the constraints of the total mass, possible core radius and the observed moment of inertia factor, we find that Al content in the martian mantle is less than 4% (shadow region in Figure 35b), and S content in the martain core is between 4.6%--13.3% (shadow region in Figure 35b).

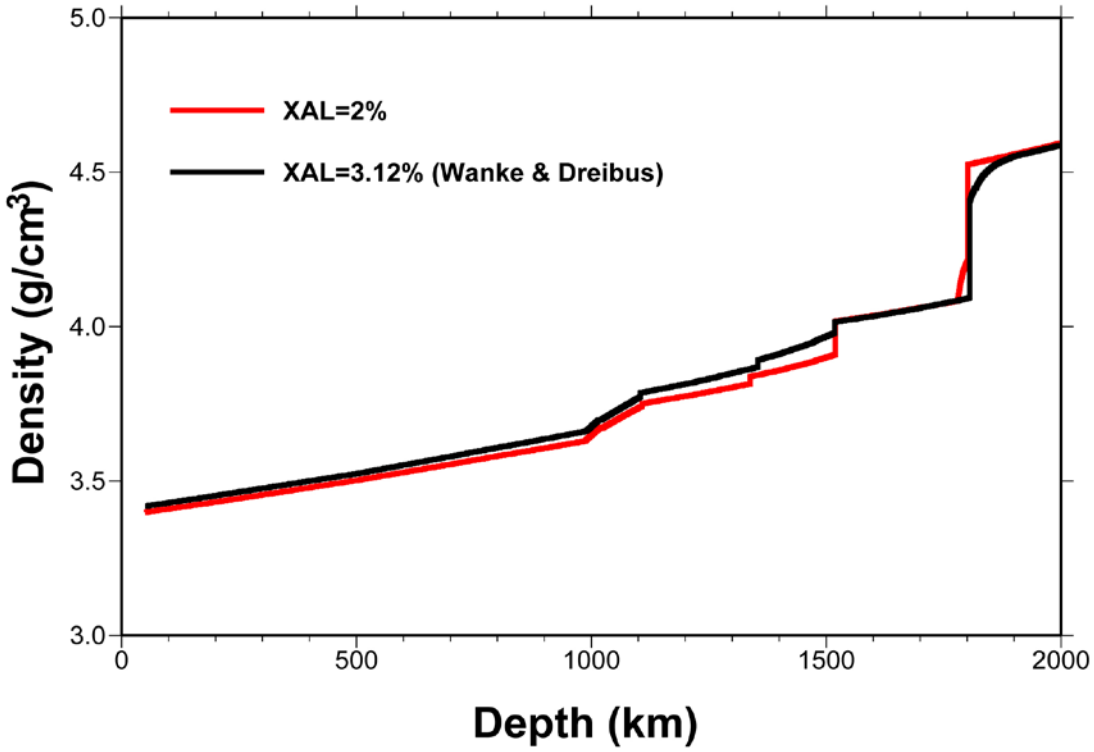

Figure 34. Predicted mantel density profiles inside Mars based on two compositional models with different Al contents.

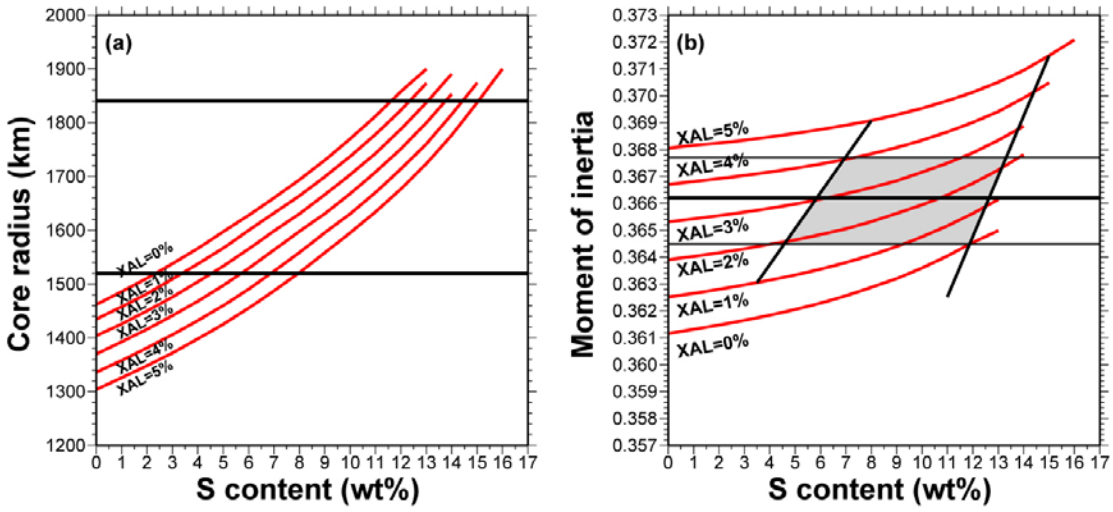

Figure 35. Predicted (a) core radius and (b) moment of inertia factors based on different Al contents in the mantle and S contents in the core. The black horizontal lines in (a) and the black vertical lines in (b) are the boundaries of possible core radius range, 1520 km and 1840 km; the black horizontal lines in (b) are the observed value and error bars of the moment of inertia factor.

For these possible mantle and core composition models, we calculate the Fe content and the Fe/Si ratio in Mars (Table 7). In the possible composition range, if S content in the core is fixed, an increasing Fe content in the mantle results in a decreasing core radius, a decreasing total Fe content and a decreasing Fe/Si ratio in Mars (Lines 3-5 in Table 7); an increasing Al content in the mantle also results in a decreasing core radius, a decreasing Fe content and a decreasing Fe/Si ratio in Mars (Lines 6-8 in Table 7). If mantle composition is fixed, an increasing S content in core results in an increasing core radius, an increasing Fe content and an increasing Fe/Si ratio in Mars (Lines 10-13 in Table 7). Based on the constraints of the total mass, possible core radius and the observed moment of inertia factor, the total Fe content in Mars is between 25.61% and 31.52%, and the Fe/Si ratio in Mars is between 1.528 and 2.114 (Lines 1 and 2 in Table 7). C1 carbonaceous chondrite has a Fe content of 27.8% and a Fe/Si ratio of 1.71 (Line 18 in Table 7), which are within our possible composition range, but our possible composition range is not narrow enough to make a conclusion if Mars has the same nonvolatile element abundances as those of C1 carbonaceous chondrite or not.

Table 7. Composition of Mars for different models

	Mantle Model	S in Core (wt%)	Core radius (km)	Mcore (wt%)	Bulk Fe (wt%)	Fe/Si
1	**Fe = 10.5%**	11.8	1840	24.41	31.52	2.114
2	**Fe = 14.3%**	7	1522	15.47	25.61	1.528
3	**Fe = 12%**	7	1612	18.30	27.85	1.722
4	**Fe = 13%**	7	1576	17.12	26.92	1.640
5	**Fe = 14%**	7	1535	15.85	25.92	1.554
6	**Al = 4.0%**	7	1524	15.52	25.65	1.532
7	**Al = 3.0%**	7	1563	16.71	26.60	1.612
8	**Al = 2.0%**	7	1599	17.87	27.51	1.692
9	**Bertka & Fei (1998)**	14.2	1421	14.24	23.1	1.319
10	**Wanke and Dreibus**	0	1363	12.76	24.36	1.407
11	**Wanke and Dreibus**	4.6	1478	14.87	25.50	1.510
12	**Wanke and Dreibus**	6	1521	15.74	25.99	1.556
13	**Wanke and Dreibus**	11	1700	19.69	28.17	1.773
14	**Fe = 14%**	0	1346	12.29	23.96	1.376
15	**Fe = 0%**	19.8	2589	54.53	49.56	5.701
16	**Fe = 13.4%**	6	1527	15.92	26.13	1.568
17	**Fe = 11.6%**	12.7	1846	24.16	31.12	2.08
18	**C1 Chondrite**				27.8	1.71

5.5 Discussions

5.5.1 Comparisons to previous study

Our study concludes that the total Fe content in Mars is between 25.61% and 30.99%, the Fe/Si ratio in Mars is between 1.528 and 2.05, and the possible composition range is too broad to make a conclusion whether or not Mars has the same nonvolatile bulk composition as that of C1 condrite (Fe% = 27.8, Fe/Si = 1.71); while previous studies (*Bertka and Fei, 1998*) conclude that the total Fe content and the Fe/Si ratio in Mars (Fe% = 23.1%, Fe/Si=1.319) (Line 9 in Table 7) are smaller than those of C1 chondrite (Fe% = 27.8, Fe/Si = 1.71). Our modeling method allows me to search for different mantle compositions, and we use a liquid core assumption and considered the uncertainties of the moment of inertia factor observation and a constraint of possible core radius; while *Fei and Bertka* used a fix mantle composition (Table 5, *Wanke and Dreibus*'s mantle composition model), a solid core assumption and did not consider the uncertainties of the moment of inertia factor observations and the constraint of core radius. The different conclusions come from the consideration of the uncertainties of moment of inertia factor observation and the variation of mantle composition in our modeling.

If we use the fixed *Wanke and Dreibus*'s composition model in the mantle, like what Fei and Bertka did, and a liquid core assumption, ignore the uncertainties of the moment of inertia factor observation and the constraint of core radius, the results become that Mars has 4.6% S in core, a core radius of 1478 km, an Fe content of 25.50% and an Fe/Si ratio of 1.510 (Figure 33, Line 11 in Table 7). The core radius (1478 km) does not fit our core radius constraint (1520—1840 km), and the Fe content and the Fe/Si ratio of

Mars are smaller than those of C1 chondrite (Fe% = 27.8, Fe/Si = 1.71), but larger than *Fei and Bertka*'s results (Fe% = 23.1%, Fe/Si=1.319). Since liquid Fe has a smaller density than solid Fe, a liquid core assumption requires a smaller S content in the core than a solid core assumption for a certain core density, and causes a larger Fe content and a larger Fe/Si ratio in Mars. If we consider the uncertainties of the moment of inertia factor observation, the possible Mars composition range is broadened. The results become that S content in the core is between 0% and 11%; core radius is between 1363 km and 1700 km; the Fe content is between 24.36% and 28.17%; and the Fe/Si ratio is between 1.407 and 1.773 (Figure 33, Lines 10 and 13 in Table 7). This composition range is too broad to conclude whether or not Mars has the same bulk composition as that of C1 chondrite. If we add an additional constraint of core radius, the results are narrowed down to a range with S content in the core between 6% and 11%, core radius between 1520 km and 1700 km, the Fe content between 25.99% and 28.17%, and the Fe/Si ratio between 1.556 and 1.773 (Figure 33, Lines 12 and 13 in Table 7). This narrowed composition range is still too broad to conclude if Mars has a bulk composition like that of C1 chondrite. Above discussion shows that if we use a fixed mantle composition, like what Fei and Bertka did, the liquid core assumption cannot change the conclusion that the bulk composition of Mars is different from that of C1 chondrite. But the uncertainties of the moment of inertia factor observation can broaden the Mars composition range enough to reach the composition of C1 chondrite. Even with the additional constraint of core radius, the composition range is still too broad to conclude if Mars has the same nonvolatile element abundances as those of C1 chondrite.

If we allow the mantle composition to vary, but ignore the uncertainties of the moment of inertia factor observation and the constraint of core radius, the results become that S content in the core is between 0% and 19.8%; core radius is between 1346 km and 2589 km; the Fe content is between 23.96% and 49.54%; and the Fe/Si ratio is between 1.376 and 5.701 (Figure 36, Lines 14 and 15 in Table 7). The composition range is broadened enough to reach the C1 chondrite composition. If we add an additional constraint of core radius, the results are narrowed down to a range with S content in the core between 6.0% and 12.7%, core radius between 1520 km and 1840 km, the Fe content between 26.13% and 31.12%, and the Fe/Si ratio between 1.568 and 2.08 (Figure 36, Lines 16 and 17 in Table 7). This narrowed composition range is still too broad to conclude if Mars has the same bulk composition like that of C1 chondrite.

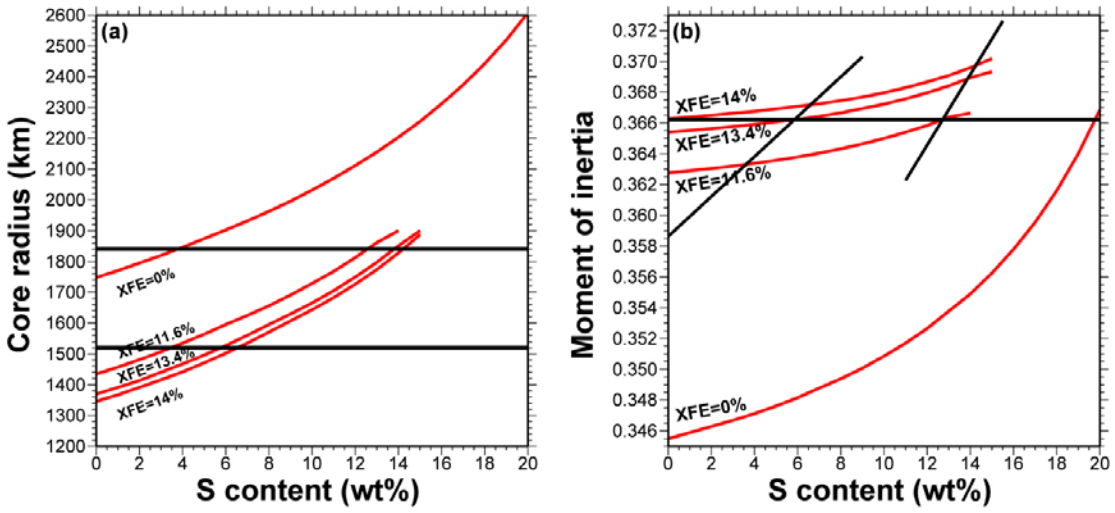

Figure 36. Predicted (a) core radius and (b) moment of inertia factors based on different Fe contents in the mantle and S contents in the core. The black horizontal lines in (a) and the black vertical lines in (b) are the boundaries of possible core radius range, 1520 km and 1840 km; the black horizontal lines in (b) are the observed value of the moment of inertia factor.

5.5.2 Other geophysical constraints

Besides the moment of inertia factor, there are other parameters, which are related to the density distributions inside Mars, such as the hydrostatic gravity and the flattening factor. The external gravitational potential of a planet is commonly described as $U = \frac{GM}{r}(1 - \sum_{n=1}^{\infty} J_{2n} P_{2n}(\sin\varphi))$, M is the total mass; G is the gravitational constant; r is the radial distance; J_{2n} is the numerical coefficients that describe the departure of the gravitational field from spherical symmetry and P_{2n} is the Legendre polynomials of degree 2n. The hydrostatic gravity field is dominated by the contribution from the J_2 term and controlled by the mass distributions inside a planet, so the J_2 value also can provide constraint on the composition of planets. The flattening factor $f = \frac{a - b}{a}$ describes the difference between the shape of a rotating planet and a perfect sphere. For a self-gravitating and rotating planet, the flattening factor is controlled by density distribution inside the planet, and can be used to constrain the planet composition.

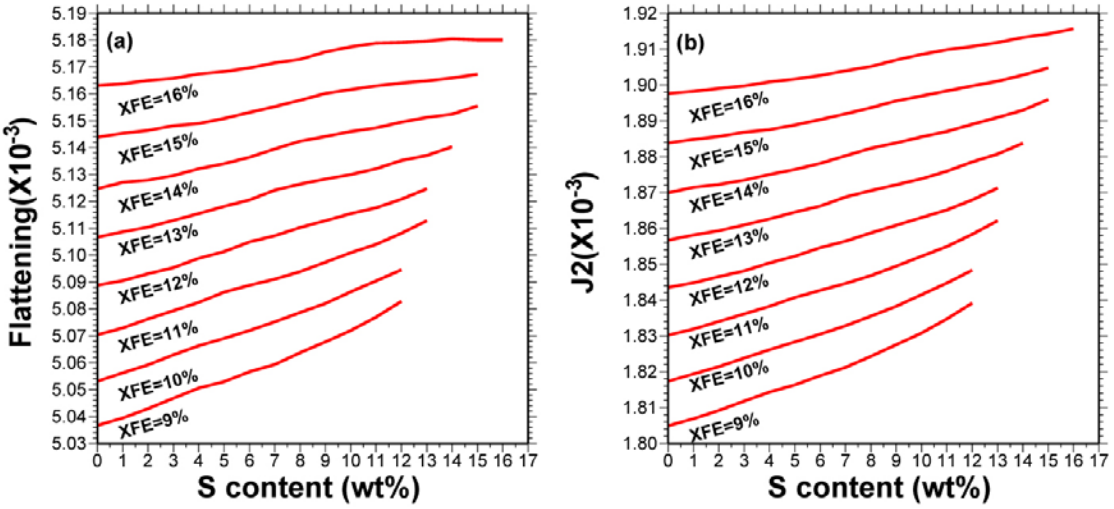

Figure 37. Predicted (a) flattening factor and (b) J_2 based on different Fe contents in the mantle and S contents in the core.

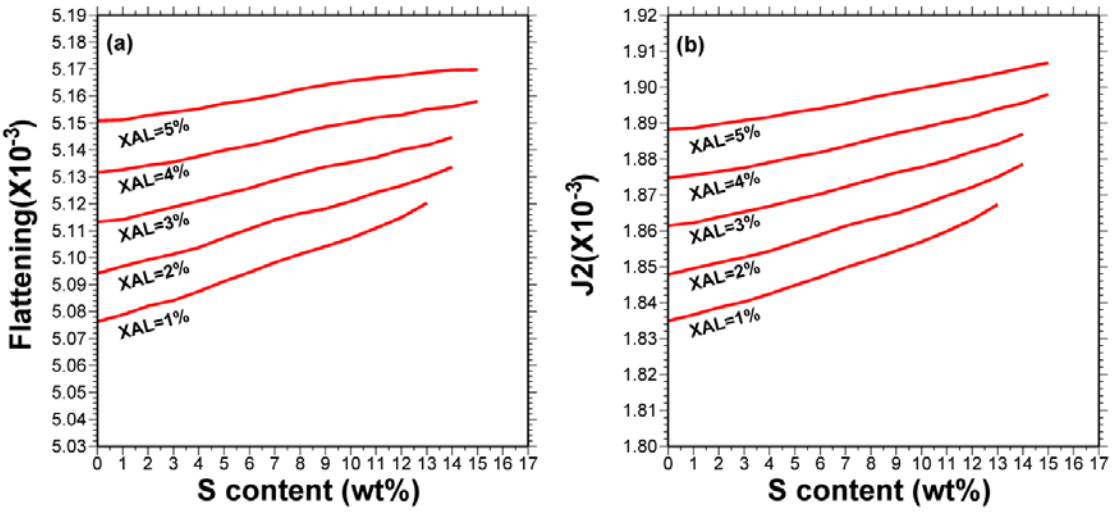

Figure 38. Predicted (a) flattening factor and (b) J_2 based on different Al contents in the mantle and S contents in the core.

We also calculate the flattening factor and the J_2 based on different composition models (Figures 37 and 38), using the second-order internal theory of equilibrium of a self-gravitating and rotating planet. The moment of inertia, the flattening factor and J_2

are all controlled by the mass distributions inside Mars, so there are relationships between those parameters. Different composition models, which have the same moment of inertia factor, result in the same flattening factor and J_2 value, so the flattening factor and the J_2 observations could not place additional constraints on Mars composition models. But the flattening factor and the J_2 values calculated using the second-order internal theory of equilibrium of a self-gravitating and rotating planet are more precise than those calculated using approximate equations: $J_2 \approx \frac{5m}{3(2.5-3.75C)^2+3} - \frac{m}{3}$ and $f \approx \frac{1}{2}(m+3J_2)$, while $m = \frac{\omega^2 R^3}{GM}$ (*Yorder and Standish, 1997*) (Table 8). The differences between the values calculated using the second order internal theory and using approximate equations, dJ_2 and df, are significant, larger than 1% of the J_2 and f values (Table 8). If we use approximate equations to calculate the moment of inertia factor C based on the J_2 value, comparing to the moment of inertia factor value calculated using density models, the difference is larger than the uncertainties of the moment of inertia factor observation. So approximate equations cannot provide precise relationships between these parameters, and our mineral physics modeling method and the second order internal theory of equilibrium of a self-gravitating and rotating planet provide a more precise way to calculate the flattening factor and the hydrostatic gravity from the moment of inertia factor.

Table 8. J_2 and the flattening factor calculating using the second-order internal theory of equilibrium and using approximate equations

Moment of inertia C	J_2 $(\times 10^{-3})$	$J_2 \approx \frac{5m}{3(2.5-3.75C)^2+3} - \frac{m}{3}$ $(\times 10^{-3})$	**d** J_2 $(\times 10^{-3})$
0.3656	1.8642	1.8328	0.0314
0.3660	1.8677	1.8373	0.0304
0.3664	1.8727	1.8432	0.0295
0.3671	1.8783	1.8517	0.0266
0.3681	1.8838	1.8645	0.0193
0.3691	1.8887	1.8767	0.0120

Table 8. J_2 and the flattening factor calculating using the second-order internal theory of equilibrium and using approximate equations (continue)

Moment of inertia C	**Flattening factor f** $(\times 10^{-3})$	$f \approx \frac{1}{2}(m+3J_2)$ $(\times 10^{-3})$	**df** $(\times 10^{-3})$
0.3656	5.117	5.044	0.073
0.3660	5.122	5.051	0.071
0.3664	5.129	5.059	0.070
0.3671	5.137	5.072	0.065
0.3681	5.142	5.091	0.051
0.3691	5.147	5.110	0.037

5.6 Conclusions

We predict density profiles in Mars based on different mantle compositions, core compositions and a liquid core assumption, then calculate the moment of inertia factors of Mars, and compare the predictions with the observation to place constraints on Mars

composition. With the constraints of the total mass, possible core radius and the observed moment of inertia factor, we find that Fe content in the martian mantle is between 10.5%--14.3%; Al content in the martian mantle is less than 4%; S content in the martian core is between 4.6%--13.3%. Based on the possible composition models of Mars, the Fe content in Mars is between 25.61% and 31.52%, and the Fe/Si ratio in Mars is between 1.528 and 2.114, and the range is too broad to make a conclusion if Mars has the same nonvolatile bulk composition as that of C1 chondrite. The difference between the conclusions of our study and *Fei and Bertka's* study is mainly caused by the consideration of the uncertainties of the moment of inertia factor observations and the variation of mantle composition in our study. We also calculated the flattening factor and the hydrostatic gravity based on different composition models, using the second-order internal theory of the equilibrium of a self-gravitating and rotating planet. Although the flattening factor and the hydrostatic gravity cannot provide additional constraints on Mars composition, our mineral physics modeling method and the second-order internal theory provide a more precise way to calculate the flattening factor and the hydrostatic gravity from the moment of inertia factor.

Bibliography

Akaogi, M. and Akimoto, S. (1979), High-pressure phase equilibria in a garnet Iherzolite, with special reference to $Mg^{2+} - Fe^{2+}$ partitioning among constituent minerals. *Physics Earth Planet. Interiors*, 19, 31-51.

Anderson, W. W. and Ahrens, T. J. (1994), An equation of state for liquid iron and implications for the Earth's core, *J. Geophys. Res.*, 99, 4273-4284.

Balog, P. S., Secco, R. A., Rubie, D. C. and Frost, D. J. (2003), Equation of state of liquid Fe-10 wt% S: Implications for the metallic cores of planetary bodies, *J. Geophys. Res.*, 108, doi:10.1029/2001JB001646.

Bertka, C. B. and Fei, F. (1998), Implication of Mars Pathfinder data for the accretion history of the terrestrial planets, *Science*, 281, 1838-1840.

Birch, F. (1947), Finite elastic strain of cubic crystals, *Physic. Review*, 71, 809-824.

Bloch, S., Hales, A. L. and Landisman, M. (1969), Velocities in the crust and upper mantle of southern Africa from multi-mode surface wave didpersion, *Bull. Seism. Soc. Am*., 159, 1599-1629.

Brudzinski, M. R. and Chen, W. P. (1997), Variations of P wave speeds in the mantle transition zone beneath the northern Philippine Sea, *J. Geophys. Res.* 102, 11,815-11,827.

Brudzinski, M. R. and Chen, W. P. (2000), Variations in P wave speeds and outboard earthquakes: Evidence for a petrologic anomaly in the mantle transition zone, *J. Geophys. Res.* 105, 21,661-21,682.

Brudzinski, M. R. and Chen, W. P. (2003), A petrologic anomaly accompanying outboard earthquakes beneath Fiji-Tonga: Corresponding evidence from broadband P and S waveforms, *J. Geophys. Res.* 108, doi:10.1029/2002JB002012.

Burdick, L. J. and Helmberger, D. V. (1978), The upper mantle P velocity structure of the Western United States, *J. Geophys. Res.* 83, 1699-1712.

Chen, W. P. and Brudzinski, M. R. (2003), Seismic anisotropy in the mantle transition zone beneath Fiji-Tonga, *Geophys. Res. Lett.* 30, doi:10.1029/2002GL016330.

Cummins, P. R., Kennett, B. L. N., Bowman, J. R. and Bostock, M. G. (1992), The 520 km discontinuity?, *Bull. Seismol. Soc. Am.* 82 (1992) 323-336.

Dziewonski, A. M. and Anderson, D. L. (1981), Preliminary reference Earth model, *Phys. Earth and Planet. Int.*, 25, 297-356.

Fei, Y., and Bertka., C. (2005), The interior of Mars, *Science*, 308, 1120-1121.

Folkner, W. M., Yoder, C. F., Yuan, D. N, Standish, E. M., and Preston, R. A. (1997), Interior structure and seasonal mass redistribution of Mars from radio tracking of Mars Pathfinder, *Science*, 278, 1749-1752.

Freybourger, M., Gaherty, J. B., Jordan, T. H. and the Kaapvaal Seismic Group (2001), Structure of the Kaapvaal craton from surface waves, *Geophys. Res. Lett.*, 28, 2489-2492.

Ganapathy, R., and Anders, E. (1974), Bulk compositions of the Moon and Earth, estimated from meteorites, *Fifth Luna Sci. Conf.*, 2, 1181.

Gao, S. S., Silver, P. G., Liu K. H. and the Kaapvaal Seismic Group (2002), Mantle discontinuities beneath Southern Africa, *Geophys. Res. Lett.*, 29, doi:10.1029/2001GL013934.

Gasparik, T. (2003), *Phase diagrams for geoscientists, An atlas of the Earth interior*, Springer, Verlag Berlin Heidelberg, New York.

Given, J. W. and Helmberger, D. V. (1980), Upper mantle structure of northwestern Eurasia, *J. Geophy. Res.* 85, 7183-7194.

Grand, S. P. and Helmberger, D. V. (1984a), Upper mantle shear structure of North America, *Geophys. J. R. astr. Soc.* 76, 399-438.

Grand, S. P. and Helmberger, D. V. (1984b), Upper mantle shear structure beneath the Northwest Atlantic Ocean, *J. Geophys. Res.* 89, 11,465-11,475.

Hager, B. H. (1984), Subducted slabs and the geoid: Constraints on mantle rheology and flow, *J. Geophys. Res.*, 89, 6003-6015.

Helmberger, D. V. and Wiggins, R. A. (1971), Upper mantle structure of Midwestern United States, *J. Geophys. Res.* 76, 3229-3245.

Honda, S. and Balachandar, D. R. S. (1993), Three-dimensional mantle dynamics with an endothermic phase transition, *Geophys. Res. Lett.*, 20, 221-224.

Irifune, T. and Ringwood, A. E. (1987), Phase transformations in primitive MORB and pyrolite compositions to 25 Gpa and some geophysical implications, *High Pressure Research in Geophysics*, Manghnani, M. H. and Y. Syono. Tokyo/Washington, Terrapub/AGU, 231-242.

Ito, E. and Takahashi, E. (1987), Ultrahigh-pressure phase transformations and the constitution of the deep mantle, *High Pressure Research in Geophysics*, Manghnani, M. H. and Y. Syono. Tokyo/Washington, Terrapub/AGU, 231-242.

Jordan, T. H. (1978), Composition and development of the continental tectosphere, *Nature* 274, 544-548.

Kennett, B. (1991), Seismic velocity gradients in the upper mantle, *Geophys. Res. Lett.*, 18, 115-118.

LeFevre, L. V., and Helmberger, D. V. (1989), Upper mantle P velocity structure of the Canadian Shield, *J. Gelphys. Res.* 94, 17,749-17,765.

Li, A. and Burke, L. (2006), Upper Mantle structure of southern Africa from Rayleigh wave tomography, *J. Geophys. Res.* 111, doi: 10.1029/2006JB004321.

Lithgow-Bertelloni, C., and Silver, P. G. (1998), Dynamic topography, plate driving forces, and the African superswell, *Nature* 395, 269-273.

Melbourne, T. and Helmberger, D. V. (1998), Fine structure of the 410-km discontinuity, *J Geophys. Res.* 103, 10,091-10,102.

Neele, F. (1996), Sharp 400-km discontinuity from short-period P reflections, *Geophys. Res. Let.* 23, 419-422.

Niu, F. L. and Kawakatsu, H. (1996), Complex structure of mantle discontinuities at the tip of the subducting slab beneath Northeast China – a preliminary investigation of broadband receiver functions, *J. Phys. Earth*, 44, 701-711.

Nyblade, A. A. and Robinson, S. W. (1994), The African superswell. *Gerphys. Res. Lett.* 21, 765-768.

Phipps Morgan, J. and Shearer, P. M. (1993), Seismic constraints on mantle flow and topography of the 660 km discontinuity: evidence for whole mantle convection, *Nature*, 365, 5-6-511.

Priestly, K. (1999), Velocity structure of the continental upper mantle: evidence from southern Africa, *Lithos*, 48, 45-56.

Priestly, K., McKenzie, D., and Debayle, E. (2006), The state of the upper mantle beneath southern Africa, *Tectonophysics*, 416, 101-112.

Qiu, X., Priestley, K. and McKenzie, D. (1996), Average lithospheric structure of southern Africa, *Geophys. J. Int.* 127, 563-587.

Richards, M. A. and Hager, B. H. (1984), Geoid anomalies in a dynamic Earth, *J. Geophys. Res.*, 89, 5987-6002.

Ringwood, A. E. (1959), On the chemical evolution and densities of the planets, *Geochim. Cosmochim. Acta.*, 15, 257-183.

Sanloup, C., Guyot, F., Gillet, P., Fiquet, G., Mezouar, M. and Martinez, I. (2000), Density measurements of liquid Fe-S alloys at high-pressure, *Geophys. Res. Lett.*, 27, 811-814.

Shearer P. M. (1991), Constraints on upper mantle discontinuities from observations of long-period reflected and converted phases, *J. Geophys. Res.*, 96, 18,147-18,182.

Shearer P. M. and Flanagan, M. P. (1999), Seismic velocity and density jumps across the 410- and 660-kilometer discontinuities, *Science*, 285, 1545-1548.

Shen, Y., Solomon, S. C., Bjarnason, I. T. and Purdy, G. M. (1996), Hot mantle transition zone beneath Iceland and the adjacent Mid-Atlantic Ridge inferred from P-to-S conversions at the 410- and 660-km discontinuities, *Geophys. Res. Lett.*, 23, 3527-3530.

Simon, R. E., Wright, C., Kgaswane, E. M. and Kwadida, T. O. K. (2002), The P wavespeed structure below and around the Kaapvaal craton to depth of 800 km, from traveltimes and waveforms of local and regional earthquakes and mining-induced tremors, *Geophys. J. Int.*, 151, 132- 145.

Simon, R. E., Wright, C., Kwadiba M. T. O. and Kgaswane, E. M. (2003), Mantle structure and composition to 800-km depth beneath southern Africa and surrounding oceans from broadband body waves, *Lithos*, 71, 353-367.

Song, T. A., Helmberger, D. V. and Grand, S. P. (2004), Low-velocity zone atop the 410-km seismic discontinuity in the northwestern United States, *Nature* 427, 530-533.

Stankiewicz, J., Chevrot, S., van der Hilst, R. D. and de Wit, M. J. (2002), Crustal thickness, discontinuity depth, and upper mantle structure beneath southern Africa: constraints form body wave conversions, *Phys. Ear. Plane. Inter.*, 130, 235-251.

Tackley, P. J., Stevenson, D. J., Glatzmaier, G. A. and Schubert, G. (1993), Effects of an endothermic phase transition at 670 km depth in a spherical model of convection in the Earth's mantle, *Nature*, 361, 699-704.

Urey, H. C. (1952), *The Planets: their origin and development*, Yale University Press, New Haven, CT.

Vidale, J. E. and Helmberger, D. V. (1987), Path effects in strong motion seismology, B. A. Bolt. *Seismic strong motion synthetics*. Computational techniques, v. 4. Orlando, Fla, Academic Press.

Vinnik, L. P., Green, R. W. E., Nicolaysen, L. O., Kosarev, G. L. and Petersen, N. V. (1996), Deep seismic structure of the Kaapvaal craton, *Tectonophysics*, 262, 67-75.

Walck, M. C. (1984), The P-wave upper mantle structure beneath an active spreading center: the Gulf of California, *Geophys. J. R. astr. Soc.* 76, 697-723.

Wang, Y., Wen, L., Weidner, D. J. and He, Y. (2006), SH velocity and compositional models near the 660-km discontinuity beneath south America and northeast Asia, *J. Geophys. Res.*, in press, doi:10.1029/2005JB003849.

Wang, Y. and Wen, L. (2007), Geometry and P and S velocity structure of the "African Anomaly", *J. Geophys. Res.*, 112, doi:10.1029/2006JB004483.

Wang, Y., Wen, L., and Weidner, D. J. (2008), Upper mantle SH- and P-velocity structures and compositional models beneath southern Africa, *Earth Planet. Sci. Lett.*, 267, 596-608.

Wang, Y., Wen, L., and Weidner, D. J. (in press), Array triplication data constraining seismic structure and composition in the mantle, *Surveys in Geophysics*, in press.

Wanke, H., and Dreibus, G. (1988), Chemical composition and accretion history of terrestrial planets, *Philos. Trans. R. Soc. London ser. A*, 325, 545-557.

Weidner, D. J. and Wang, Y. (1998), Chemical- and Clapeyron-induced buoyancy at the 660 km discontinuity, *J. Geophys. Res.*, 103, 7431-7441.

Weidner D. J. and Wang, Y. (2000), Phase Transformations: Implications for Mantle Structure, *Earth's Deep Interior: Mineral Physics and Tomography From the Atomic to the Global Scale*, 215-235.

Wen, L. and Anderson, D. L. (1997a), Layered mantle convection: A model for geoid and topography, *Earth Planet. Sci. Lett.*, 146, 367-377, 1997a.

Wen, L. and Anderson, D. L. (1997b), The present-day plate motion constraint on mantle rheology and convection, *J. Geophys. Res.*, 102, 24,639-24,654.

Wright, C., Kwadiba, M. T. O., Kgaswane, E. M. and Simon, R. E. (2002), The structure of the crust and upper mantle to depth of 320 km beneath the Kaapvaal craton, from P wave arrivals generated by regional earthquakes and mining-induced tremors, *J. Afric. Ear. Sci.*, 35, 477-488.

Wright, C., Kwadiba, M. T. O., Simon, R. E., Kgaswane, E. M. and Nguuri, T. K. (2004), Variations in the thickness of the crust of the Kaapvaal craton, and mantle structure below southern Africa, *Ear. Plane. Spac.*, 56, 125-137.

Yoder, C. F., and Standish, E. M. (1997), Martian precession and rotation from Viking lander range data, J. *Geophys. Res*., 102, 4065-4080.

Yoder, C. F., Konopliv, A. S., Yuan, D. N., Standish, E. M., and Folkner, W. M. (2003), Fluid core size of Mars from Detection of the solar tide, *Science*, 300, 299-303.

Yu, Y. G., Wentzcovitch, R. M., Tsuchiya, T., Umemoto, K. and Weidner, D. J. (2007), First principle investigation of the postspinel transition in Mg_2SiO_4, *Geophys. Res. Lett.*, 34, doi: 10.1029/2007GL029462.

Zhang, J. (1994), Melting experiments on anhydrous peridotite KLB-1 from 5.0 to 22.5 Gpa, *J. Geophys. Res.* 99, 17,729-17,742.

Zhao, M. C., Langston, C. A., Nyblade, A. A. and Owens, T. J. (1999), Upper mantle velocity structure beneath southern Africa from modeling regional seismic data, *J. Geophys. Res.* 104, 4783-4794.

Zhu, L. P. and Rivera, L. A, (2002), A note on the dynamic and static displacements from a point source in multilayered media, *Geophys. J. Int.* 148, 619-627.